

Nanowire-based Quantum Photonics

Proefschrift

ter verkrijging van de graad van doctor
aan de Technische Universiteit Delft,
op gezag van de Rector Magnificus prof. ir. K.C.A.M. Luyben,
voorzitter van het College voor Promoties,
in het openbaar te verdedigen op maandag 12 mei 2014 om 12.30 uur

door

Gabriele BULGARINI

Master of Science in Physics Engineering, Politecnico di Milano, Italië
geboren te Milan (Italië)

Dit proefschrift is goedgekeurd door de promotor:

Prof. dr. L.P. Kouwenhoven

Copromotor:

Dr. V. Zwiller

Samenstelling promotiecommissie:

Rector Magnificus,	voorzitter
Prof. dr. L.P. Kouwenhoven,	Technische Universiteit Delft, promotor
Dr. V. Zwiller,	Technische Universiteit Delft, copromotor
Prof. dr. J. Gomez Rivas,	TU Eindhoven
Prof. dr. A. Rastelli,	Johannes Kepler Universität, Oostenrijk
Prof. dr. S. Reitzenstein,	TU Berlijn, Duitsland
Prof. dr. J.M. Gerard,	CEA, Frankrijk
Prof. dr. H.W. Zandbergen,	Technische Universiteit Delft
Prof. dr. R. Hanson,	Technische Universiteit Delft, reservelid



Dit werk maakt deel uit van het onderzoekprogramma van de Stichting voor Fundamenteel Onderzoek der Materie (FOM), die deel uitmaakt van de Nederlandse Organisatie voor Wetenschappelijk Onderzoek (NWO)

Published by: Gabriele Bulgarini

Printed by: Gildeprint, Enschede

Cover by: Gabriele Bulgarini

Casimir PhD series Delft-Leiden 2014-10

ISBN 978-90-8593-185-0

Copyright ©2014 Gabriele Bulgarini

Contents

1	Introduction	7
1.1	Single-photon generation: state of the art	8
1.2	Quantum dots in nanowire: outline of this thesis	12
1.3	References	14
2	Optical properties of a semiconductor quantum dot	17
2.1	Spectroscopy of a single quantum dot	18
2.2	Exciton fine-structure splitting and entanglement generation	21
2.3	Photon statistics	23
2.4	Photon coherence	25
2.5	References	29
3	Realization of semiconductor single-photon sources	31
3.1	Self-assembled quantum dots	32
3.2	Nanowire quantum dots	32
3.3	Single-photon collection strategies	33
3.3.1	Solid immersion lens	34
3.3.2	Optical microcavity	34
3.3.3	Tapered nanowire waveguide	35
3.4	Fabrication of the nanowire waveguide	37
3.4.1	MOVPE growth	38
3.4.2	CBE growth	38
3.5	Photon collection from nanowire devices	39
3.6	References	43
4	Quantum dot emission coupled to a nanowire waveguide mode	47
4.1	Introduction	48
4.2	Sample preparation and characterization	48
4.3	Time-resolved photoluminescence	50
4.4	Conclusions	52
4.5	References	54

5	Bright single-photon sources in bottom-up tailored nanowire waveguides	57
5.1	Introduction	58
5.2	Fabrication of a tapered nanowire waveguide	59
5.3	Quantum dot location and composition	60
5.4	Sample preparation	62
5.5	Single-photon extraction efficiency	63
5.6	Modeling of the fundamental waveguide mode	65
5.7	Extraction efficiency enhancement	66
5.8	Conclusions	67
5.9	References	69
6	Gaussian far field emission for ideal fiber-coupling	71
6.1	Introduction	72
6.2	Numerical simulations of the far field emission profile	72
6.3	Diameter dependent analysis: high order waveguide modes	77
6.4	Coupling to single-mode optical fiber	79
6.5	Conclusions	80
6.6	References	81
7	Single-photon interference measurements	83
7.1	Introduction	84
7.2	Single-photon coherence measurements	84
7.3	Counteracting dephasing mechanisms	87
7.4	Monte Carlo simulations of the quantum dot emission spectrum	88
7.5	Conclusions	90
7.6	Appendix 1: single-photon interference and spectral lineshapes	91
7.7	Appendix 2: details of Monte Carlo simulations	92
7.8	References	98
8	Nanowire opto-electronics: a quantum dot in a nanowire photodiode	101
8.1	Introduction	102
8.2	Device characterization	102
8.3	Resonant quantum dot excitation	106
8.4	Appendix: Photon number estimation	108
8.5	References	109
9	Conclusions and outlook	111
9.1	Achieved results and status of research	111
9.2	Future research directions	112
9.3	Outlook: a plug and play single-photon generator	114
9.4	References	119
	Summary	123
	Samevatting	124
	Sommario	125
	Curriculum Vitae	127
	Publications	128

CHAPTER 1

Introduction

The manipulation of quantum states of matter is at the heart of devices for quantum technologies. Quantum mechanical interactions regulate the transitions from one state to another of a quantum device. Engineering and functionalizing these quantum devices leads to a broad range of foreseen innovative applications. For instance, a quantum computer is expected to solve complex algorithms at a much faster speed than a classical computer, since it would allow for trying all the solutions at once processing a superposition of input states. Simulation of complex physical and biological system could also be performed much faster by using quantum interactions instead of executing classical calculations. Along the same line, measurements that utilize quantum interactions are anticipated to enhanced enormously the sensitivity of metrology. Several systems are proposed as carriers of quantum bits of information (qubits). Among them, we can distinguished between stationary qubits, that are localized in space, and flying qubits that can travel long distances while maintaining the carried information. Whereas the proposed implementations of stationary quantum bits are several, for example based on superconducting resonators, electron or nucleus spin, the system of choice for flying quantum bits is represented almost exclusively by photons. The science that employs single light particle is called quantum photonics, or quantum optics. In addition to optics-based implementation of the above mentioned applications, single photons provide a route to secure communications utilizing quantum cryptography. The idea behind quantum cryptography is sending information via single photons and protecting it by the laws of quantum mechanics. The most common approach to secure information is based on the quantum key distribution protocols [1, 2, 3]. In these schemes only the key to encrypt and decrypt the information is based on single-photons. As in con-

ventional cryptography the message is encrypted with the secret key and sent via a classical channel. To finally decode the message the receiver needs to know the secret key. The same applies to an eavesdropper trying to listen at the private conversation. However, the generation of the secret key is based on quantum mechanics and thereby fundamentally protected against eavesdropping. Since the quantum state of a photon cannot be cloned, it is impossible for the eavesdropper to learn the key without changing the photon state and thus being unavoidably detected. Quantum cryptography provides fundamentally secure communication, but nevertheless the security suffers from imperfections in its physical implementation. For instance, if the information is erroneously transmitted by two photons, the secret listener may collect one of them to gain knowledge of the message without leaving any trace. The desired source in the field of quantum cryptography shall provide the highest possible photon flux combined with a very low probability of multi-photon emission. For the actual implementation of the quantum bits using photons there are several alternatives. The most commonly utilized is the photon polarization [4]. Other implementations of photonic qubits rely on the photon number state or in the time-bin between consecutive photons [5]. These latter implementations are more robust for fiber-based long distance communication, because photon polarization is altered after propagating long distances in a fiber [6].

1.1 Single-photon generation: state of the art

The concept of the photon as light particle was introduced more than a century ago [7]. Nowadays, demonstrating the quantum nature of light has become a standard experiment utilizing sources that are able to emit individual photons. One at a time, single photons are directed towards a half-silvered mirror, a beam splitter. Here, each photon has 50 % probability of being reflected and 50 % probability of being transmitted. At each output port of the beam splitter a single-photon counter is positioned. When the source emits only individual photons, there are never simultaneous detection events on both detectors. The photon wavefunction takes both output paths, but collapses only at one of the two detectors where it is absorbed, thereby triggering a detection event that reveals its quantized nature. If we now position in place of the photodetectors two mirrors facing the beam splitter we create an interferometer. In this case, the photon wavefunction after traveling along both interferometer arms is reflected at the mirrors. The superposition of the photon being reflected and being transmitted at the beam splitter is thus brought back to the original beam splitter where the superposition was created. Here, depending on the phase difference acquired while traveling the two interferometer arms, interference of the photon electric field determines the photon output direction. The fact that such interference is realized from just a single particle is a striking expression of the quantum mechanical description of light.

In order to characterize single-photon sources and their optical quality, we list the most important requirements of a quantum emitter.

- **Deterministic.** A source should emit on-demand as a response of a trigger event such as an excitation laser pulse.
- **Bright.** The source should emit an intense flux of photons which are efficiently collected. For demonstrating high brightness, photodetectors with high detection efficiency are also necessary.
- **Coherent.** The emission bandwidth should be limited by the Fourier-transform of the emission lifetime.
- **Pure single-photon statistics.** The emission statistics should be described by a non-classical number state of 1 (Fock State). The probability of multi-photon events should be zero.
- **Gaussian emission mode.** Photons should be emitted in a Gaussian mode to provide efficient coupling to optical fibers.

In addition to these five basic properties, additional requirements may be added depending on the specific aim of an experiment or an application. We list four additional properties.

- **Frequency tunability.** A tunable emission energy, by means of electric field, magnetic field, strain or temperature is necessary for coupling more sources and performing two photon interference, that is a basic requirement for implementation of quantum communication or linear optics quantum computation. The emission can be also precisely tuned to the telecom wavelength range to provide very low losses for long distance communication in optical fibers. Alternatively, the emission frequency can be chosen to be in resonance with atomic transitions for the coupling of single-photon sources to atomic vapors.
- **Electrically driven emission.** The emission of single photons is obtained after an electrical trigger. This approach may simplify realistic device implementation by avoiding the use of laser excitation.
- **Entanglement.** A source emitting pairs of entangled photons is particularly important for quantum computing and required for the implementation of a quantum repeater for long distance quantum communication.

The most common choice for generation of single photons is the spontaneous parametric downconversion process [3]. One laser photon impinging on a non-linear crystal generates two photons, each carrying half of the laser photon energy. If phase matching conditions are attained, the two output photons are polarization-entangled [8]. Parametric downconversion is inherently a very inefficient process and because of its probabilistic

nature, a single photon cannot be emitted on-demand at a precise moment in time. This problem is partially overcome by utilizing the advantage that two photons are simultaneously generated. The detection of the first photon can be used to herald the presence of the second photon, optimizing the success probability for each communication attempt at the expense of diminishing the number of usable photons [9].

Most of the doubts about the suitability of laser light for single-photon generation is ascribed to the fact that such sources follow Poissonian statistics. Even though the power of a laser pulse is reduced to have an average probability of one photon per pulse, Poissonian statistics of coherent light implies that there is still a high probability of getting zero photons and not negligible probability of having more than one photon per pulse. For the spontaneous downconversion process, this implies that four or six photons can be found when just two were expected.

Ideally, this problem is overcome by utilizing a two energy level system that allows for relaxation from the excited state to the ground state via an individual photon. Such a perfect single-photon source does not obey Poissonian statistics but has instead full probability emitting an individual photon. Seminal experiments on single photons were performed using natural atomic transitions between two energy levels of individual sodium atoms [10]. Later, the first experimental demonstration of quantum entanglement through violation of Bell's inequality was achieved using calcium atoms [11]. Single atoms are isolated in magneto-optical traps and are fundamentally equal to one another when they are kept under ultra high vacuum in an unperturbed environment [12]. As a result, the emission of atomic transition has emission linewidth not yet achievable with solid-state single photon sources. Experimental work on single atoms is pioneering the field of quantum networks with atoms operating both as quantum emitters and quantum memories [13]. The disadvantage of atoms, however, is that they are trapped in ultra high vacuum conditions in potential lattices created by laser interference. Such complex architecture hampers scalability and does not suggest atoms as the candidate photon sources in the next generation of personal computers.

The realization of quantum light sources in solid-state is envisioned as the main route to the miniaturization of single-photon sources with control over the source position aiming at scaling-up the number of quantum light sources connected in a network. The solid-state system that is the most similar to an atom is a crystal impurity. The most popular crystal impurities for photon emission are nitrogen vacancy centers in diamond [14]. The rich spin environment of electrons and nuclei in the nitrogen vacancy center complex [15] makes it very appealing for quantum information [16] and magnetometry [17]. Such source enables single-photon emission up to room temperature and recently electroluminescence has been observed from such a high bandgap material [18]. Nevertheless, the strong phonon coupling deteriorates the emission linewidth and furthermore, considerable part of the emission falls in the phonon side-band.

Single molecules represent an alternative avenue to single-photon generation at room temperature. Compared to inorganic semiconductors and color centers in diamond, molecules are embedded in a dielectric with refractive index between 1 and 1.5. This

allows the use of oil-immersion lenses to cancel the dielectric mismatch and effectively enlarge the collection numerical aperture to enhance the collection efficiency to the record value of 96 % [19]. This collection efficiency is the highest ever obtained for single-photon sources, however the main problem for realistic application of molecule-based sources is the bleaching of the fluorescence. In the excited state, molecules undergo photochemical reactions that irreversibly lead them to a dark state after a limited amount of excitation cycles [20] and thus hamper their utilization in the long time scale.

Quantum dots are semiconductor nanostructures composed by a few thousands atoms. The spatial confinement of carriers provided by the nanoscale dimension of a quantum dot gives rise to discrete energy levels that resembles the level scheme of an atom. For this reason semiconductor quantum dots are often referred to as *artificial atoms* [21] and thus play a major role in the context of single-photon generation. Upon laser excitation, electron and hole pairs, excitons, can be generated in the discrete energy levels of a quantum dot. The recombination of the last residing exciton in the quantum dot is the transition utilized for single-photon emission, since the quantum dot cannot emit again unless re-excited by the following excitation pulse.

Semiconductor quantum dots present several advantages compared to other single-photon emitters. A quantum dot outputs an individual photon on-demand at each laser pulse and at a precise frequency. The deterministic nature of the emission is combined with the source brightness making semiconductor quantum dots appealing for application in quantum cryptography. Another key advantage of semiconductors over other single-photon sources is the versatility in emission wavelength. By varying the quantum dot composition, the wavelength of quantum dot emission is tuned from the ultraviolet [22] to the telecom wavelength range of 1.3 μm [23] and 1.55 μm [24]. In turn, every dot emits at a slightly different wavelength compared to the neighboring quantum dot. This is both due to the individual composition and position of individual constituents of a ternary semiconductor alloy, strain induced on the quantum dot as well as defects in the surrounding semiconductor. Having different quantum dots emitting at the very same frequency is crucial for the interference of two indistinguishable single photons, upon which linear-optics quantum computation and quantum communication are based. Researchers have been thus trying to obtain control on the emission energy of individual quantum dots. The most promising approach to date for tuning the exciton emission frequency is to combine biaxial strain with external applied electric field in order to tune both the quantum dot emission [25] and the exciton properties [26] without losing the source brightness.

Quantum dots are also natural sources of polarization-entangled photons via the biexciton-exciton cascade [27], whose properties can be tuned by controlling the quantum dot shape during growth [28]. Compared to laser downconversion, quantum dots produce on-demand pairs of polarization-entangled photons because their emission does not rely on a probabilistic process [29]. Importantly, semiconductor quantum dots can

be easily embedded at the interface of p-n junctions whilst preserving the above mentioned optical properties. Extensive research has been devoted in this direction for first achieving electrically driven single-photon emission [30] and subsequently generation of polarization-entangled photon pairs [31]. These electrically driven sources have been recently used for the teleportation of a quantum dot exciton emission using the following biexciton-exciton cascade [32]. The weakness of such quantum dot based light-emitting diodes is the random positioning of the quantum dot, that becomes deterministically controlled when utilizing quantum dots grown in nanowire p-n junctions [33].

The optical properties of quantum dots pave the way to the realization of an optical quantum network. The nodes of such network as well as the logic gates of a quantum computer based on linear optics [34] require the interference of two (or more) photons emitted from distinct light sources. First two-photon interference measurements have been realized by tuning a laser in resonance with the quantum dot emission [35] and by tuning two exciton transitions from independent quantum dots at the same frequency through strain [36]. To push long distance communication towards high efficiency, optical fibers should be involved and thus emission energy in the telecom wavelength range, 1.3 or 1.55 μm , are required. To date, the only two-photon interference measurement that uses photons at telecom wavelength has been performed using parametric down-conversion [37]. Quantum interference of single photons at telecom wavelength, yet to be realized with semiconductor quantum light sources, is of the utmost importance to turn quantum networks into an approachable reality.

1.2 Quantum dots in nanowire: outline of this thesis

In this thesis we develop novel sources of single photons with high brightness, pure single-photon statistics and a narrow spectrum based on quantum dots embedded in semiconductor nanowires. Nanowires are quasi one-dimensional structures that are grown with a bottom-up technique enabling the controlled growth of an individual heterostructured quantum dot on the nanowire axis. Recent developments of this novel growth technique provides control over both the semiconductor crystal phase purity of the semiconductor and the nanowire shape. The nanowire can be tailored into a waveguide for the photons emitted from the quantum dot. Excellent accuracy in positioning the quantum emitter on the waveguide axis results in efficient coupling to the fundamental waveguide mode along the nanowire and Gaussian far-field emission of single photons. Outstanding advantage of quantum dots in nanowires is that all ingredients for their excellent optical quality are obtained together, while maintaining site-controlled growth and the ability of positioning only a single emitter per nanowire waveguide. In addition to the emission properties, individual quantum dots are embedded in nanowire p-n junctions and are utilized in this thesis as efficient photodiodes, thus demonstrating the possibility of using nanowire-based devices as both quantum emitters and detectors.

In this thesis we analyze the optical properties of quantum dots in nanowire waveguides. Point by point, we analyze the requirements and address the major hurdles for the development of high quality single-photon sources. The basic concepts of photoluminescence spectroscopy of single quantum dots along with a description of the statistical properties of single-photon sources are given in **Chapter 2**. The most common quantum dot growth techniques and the photonic structures employed for collecting single photons with high efficiency are presented and compared in **Chapter 3**. From **Chapter 4** the thesis focuses on the system of quantum dots in nanowires. In particular, we start by studying the coupling of quantum dot emission to waveguide mode in a nanowire which is measured as a function of the nanowire diameter. Optimum waveguide conditions are utilized in **Chapter 5**, in combination with a tapered tip and a bottom-gold mirror, to improve the photon collection efficiency. **Chapter 6** investigates the far field radiation profiles that are obtained under different waveguide conditions. In **Chapter 7**, we study single-photon interference measurements at different temperatures to measure the bandwidth of single photons and the causes of photon decoherence. **Chapter 8** describes an opto-electronic device that consists of a single quantum dot embedded in the multiplication region of a avalanche nanowire photodiode. The optical properties of a single quantum dot are combined with the electrical properties of a nanowire p-n junction. In **Chapter 9**, the results of the thesis are summarized and future research directions are discussed.

1.3 References

- [1] C.H. Bennett, G. Brassard, Quantum cryptography: Public key distribution and coin tossing. *Proc. of Int. Conf. on Computers, Systems and Signal Processing*, **175**, 175–179 (1984).
- [2] A.K. Ekert, Quantum cryptography based on Bell’s theorem. *Phys. Rev. Lett.* **67**, 661–663 (1991).
- [3] N. Gisin, G. Ribordy, W. Tittel, and H. Zbinden, Quantum cryptography. *Rev. Mod. Phys.* **74**, 145–195 (2002).
- [4] G. Ribordy, J. Brendel, J.-D. Gautier, N. Gisin and H. Zbinden, Long-distance entanglement-based quantum key distribution. *Phys. Rev. A* **63**, 012309 (2000).
- [5] W. Tittel, J. Brendel, H. Zbinden, and N. Gisin, Quantum cryptography using entangled photons in energy-time Bell states. *Phys. Rev. Lett.* **84**, 4737–4740 (2000).
- [6] H. Takasue et al., Quantum key distribution over a 40-dB channel loss using superconducting single-photon detectors. *Nat. Photon.* **1**, 343–348 (2007).
- [7] A. Einstein, Über einen die Erzeugung und Verwandlung des Lichtes betreffenden heuristischen Gesichtspunkt. *Ann. Phys.* **17**, 132–148 (1905).
- [8] P. Kwiat et al., New high-intensity source of polarization-entangled photon pairs. *Phys. Rev. Lett.* **75**, 4337–4341 (1995).
- [9] M. Giustina et al., Bell violation using entangled photons without the fair-sampling assumption. *Nature* **497**, 227–230 (2013).
- [10] H.J. Kimble, M. Dagenais and L. Mandel, Photon antibunching in resonance fluorescence. *Phys. Rev. Lett.* **39**, 691–695 (1977).
- [11] A. Aspect, J. Dalibard and G. Roger, Experimental test of Bell’s inequalities using time-varying analyzers. *Phys. Rev. Lett.* **49**, 1804–1807 (1982).
- [12] T. Wilk, S.C. Webster, A. Kuhn and G. Rempe, Single-Atom Single-Photon Quantum Interface. *Science* **317**, 488 (2007).
- [13] S. Ritter et al., An elementary quantum network of single atoms in optical cavities. *Nature* **484**, 195–200 (2012).
- [14] R. Brouri, A. Beveratos, J.-P. Poizat and P. Grangier, Photon antibunching in the fluorescence of individual color centers in diamond. *Opt. Lett.* **25**, 1294–1296 (2000).

- [15] W. Pfaff et al., Demonstration of entanglement-by-measurement of solid-state qubits. *Nat. Phys.* **9**, 29–33 (2013).
- [16] H. Bernien et al., Heralded entanglement between solid-state qubits separated by 3 meters. *Nature* **497**, 86–90 (2013).
- [17] G. De Lange, D. Riste, V.V. Dobrovitski and R. Hanson, Single-spin magnetometry with multipulse sensing sequences. *Phys. Rev. Lett.* **106**, 080802 (2011).
- [18] N. Mizuochi et al., Electrically driven single-photon source at room temperature in diamond. *Nat. Photon.* **6**, 299–303 (2012).
- [19] K.G. Lee et al., A planar dielectric antenna for directional single-photon emission and near-unity collection efficiency. *Nat. Photon.* **5**, 166–169 (2011).
- [20] W.E. Moerner, M. Orrit, Illuminating Single Molecules in Condensed Matter. *Science* **283**, 1670–1676 (1999).
- [21] R. Bratschitsch and A. Leitenstorfer, Quantum dots: Artificial atoms for quantum optics. *Nat. Mater.* **5**, 855–856 (2006).
- [22] M.J. Holmes, K. Choi, S. Kako, M. Arita and Y. Arakawa, Room-temperature triggered single photon emission from a III-Nitride site-controlled nanowire quantum dot. *Nano Lett.* (2014).
- [23] M.B. Ward et al., On-demand single-photon source for 1.3 μm telecom fiber. *Appl. Phys. Lett.* **86**, 201111 (2005).
- [24] M. Benyoucef, M. Yacob, J.P. Reithmaier, J. Kettler and P. Michler, Telecom-wavelength (1.5 μm) single-photon emission from InP-based quantum dots. *Appl. Phys. Lett.* **103**, 162101 (2013).
- [25] J. Zhang et al., A Nanomembrane-Based Wavelength-Tunable High-Speed Single-Photon-Emitting Diode. *Nano Lett.* **13**, 5808–5813 (2013).
- [26] R. Trotta et al., Universal Recovery of the Energy-Level Degeneracy of Bright Excitons in InGaAs Quantum Dots without a Structure Symmetry. *Phys. Rev. Lett.* **109**, 147401 (2012).
- [27] N. Akopian et al, Entangled photon pairs from semiconductor quantum dots. *Phys. Rev. Lett.* **96**, 130501 (2006).
- [28] G. Juska et al., Towards quantum-dot arrays of entangled photon emitters. *Nat. Photon.* **7**, 527–531 (2013).
- [29] M. Mueller, S. Bounouar, K.D. Jöns, M. Glässl, P. Michler, On-demand generation of indistinguishable polarization-entangled photon pairs. *Nat. Photon.* **8**, 224–228 (2014).

- [30] Z. Yuan et al, Electrically driven single-photon source. *Science* **295**, 102–105 (2002).
- [31] C.L. Salter et al., An entangled-light-emitting diode. *Nature* **465**, 594–597 (2010).
- [32] J. Nilsson et al., Quantum teleportation using a light-emitting diode. *Nat. Photon.* **7**, 311–315 (2013).
- [33] S. Deshpande, J. Heo, A. Das and P. Bhattacharya, Electrically driven polarized single-photon emission from an InGaN quantum dot in a GaN nanowire. *Nat. Commun.*, **4**, 1675 (2013).
- [34] E. Knill, R. Laflamme and G.J. Milburn, A scheme for efficient quantum computation with linear optics *Nature* **409**, 46–52 (2001).
- [35] A.J. Bennett, R.B. Patel, C.A. Nicoll, D.A. Ritchie and A.J. Shields, Interference of dissimilar photon sources. *Nat. Phys.* **5**, 715–717 (2009).
- [36] E.B. Flagg, Interference of single photons from two separate semiconductor quantum dots. *Phys. Rev. Lett.* **104**, 137401 (2010).
- [37] A.R. McMillan et al., Two-photon interference between disparate sources for quantum networking. *Sci. Rep.* **3**, 2032 (2013).

CHAPTER 2

Optical properties of a semiconductor quantum dot

A quantum dot is a semiconductor nanostructure where the reduced spatial dimensions induce quantum confinement resulting in discrete energy levels in conduction and valence band. The potential enables for the confinement of electrons, holes or both charges in the form of excitons. Depending on the symmetry of the potential distribution as well as the number of electron and holes simultaneously populating the dot, the properties of excitons inside a quantum dot have peculiar characteristics. In this chapter, we survey the fundamental principles of single quantum dot spectroscopy in order to set the basis for the understanding of experiments shown in this thesis. Furthermore, exciton recombination between discrete energy levels is utilized in quantum dots to generate single photons. Principles of single-photon statistics and experimental methods for the analysis of the single-photon coherence properties are discussed

2.1 Spectroscopy of a single quantum dot

We consider a heterojunction consisting of a semiconductor quantum dot embedded in a semiconductor matrix with large energy bandgap. At the interface, the alignment of conduction band and valence band of the two semiconductors provides a potential well for the confinement of both electrons and holes. This alignment is defined as type I band alignment [1] and is displayed for InP and InAsP in Fig. 2.1a. The schematic displays, not in scale, the energy of the bottom of the conduction band and the top of the valence band as a function of position across the heterojunction. The bandgap of $\text{InAs}_{0.25}\text{P}_{0.75}$ is lower compared to InP by 220 meV for zincblende InP (1.42 eV at room temperature) and 290 meV in case of wurtzite InP (1.51 eV). In particular, the energy levels shown in the schematics account for spatial confinement in the InAsP region. We consider a disk-shaped quantum dot with height of a few nanometers (across the heterojunction) and diameter of a few tens of nanometers. The strong spatial confinement along the height raises the quantum dot ground state (s-shell) as compared to the bottom of InAsP conduction band. For a quantum dot of 4 nm in height, the electron confinement energy is 79 meV, while the confinement energy for heavy holes is 18 meV. From the weaker radial confinement we obtain higher order states (shells) with a separation of about 20 meV for a quantum dot of 30 nm in diameter.

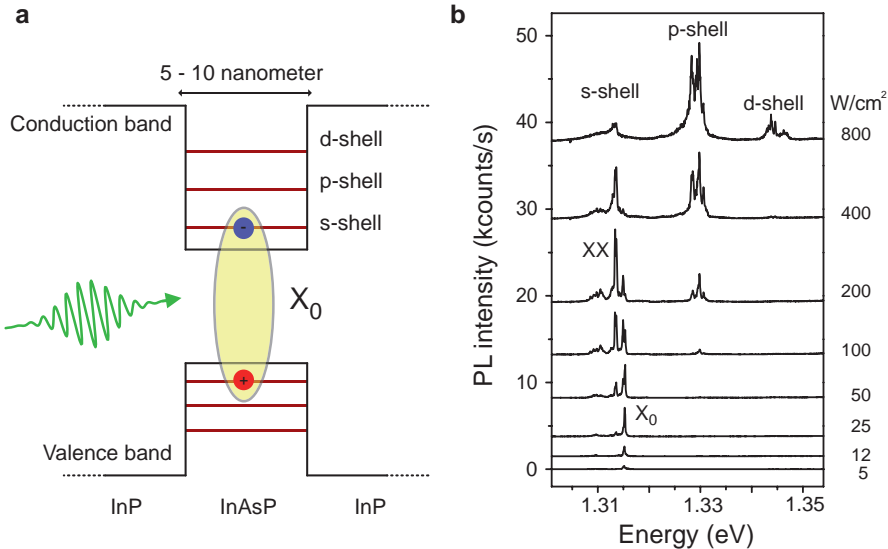


Figure 2.1: Single quantum dot spectroscopy. **a**, Schematics of the quantum dot energy level structure in InAsP/InP system with type I heterostructure band alignment. The quantum dot is excited by a laser pulse, which generates and exciton. **b**, Set of photoluminescence spectra obtained at different laser excitation power (power density on the right). We observe the state filling of the quantum dot as the laser power is increased.

Two different photo-excitation paths can be chosen to generate excitons in a quantum dot. A laser pulse tuned in resonance with one of the quantum dot transitions directly creates an exciton. Alternatively, laser excitation with energy higher than the bandgap of the surrounding semiconductor generates electron-hole pairs, that will subsequently relax inside the quantum dot due to the lower energy. It is still an open question whether photo-generated excitons migrate in the quantum dot or if electron-hole pairs first separate in the semiconductor matrix and then migrate as free charges in the quantum dot where they form excitons. Once in the quantum dot, excitons relax towards the lowest energy empty levels. Energy levels in the quantum dot are typically probed with photoluminescence spectroscopy, that is the collection of photons emitted by the quantum dot upon laser excitation.

In all III–V semiconductors, electrons belong to a s-wave conduction band with zero angular momentum, whereas the holes reside in the p-like valence band and therefore have an angular momentum $L = \hbar$, where \hbar is the reduced Planck constant. Taking the spin into account, the electron has a total angular momentum $J = L + S = \frac{1}{2}\hbar$. Holes in the valence band have $J = \frac{3}{2}\hbar$ and, neglecting the split-off bands, divide in two categories depending on the momentum projection along z : heavy holes ($J_z = m_z\hbar = \pm \frac{3}{2}\hbar$) and light holes ($J_z = \pm \frac{1}{2}\hbar$). The ground state of a single hole in a quantum dot is heavy hole. Light holes are found typically few tens of meV below the heavy holes levels, even though this order can be reversed under certain circumstances, for example by applying tensile stress [2]. Throughout this thesis we only refer to heavy holes neglecting mixing with light holes in the valence band.

Radiative recombination of excitons in the quantum dot only occurs in accordance of selection rules for optical transitions. Electric dipole optical transitions are allowed for $\Delta J = 0$ or $\pm\hbar$ transferred from the electron-hole pair to the photon. In the case of a heavy hole exciton such optical selection rules are attained for two exciton states: $m_z = +\frac{1}{2}$ ($-\frac{1}{2}$) for the electron and $m_z = -\frac{3}{2}$ ($+\frac{3}{2}$) for the hole. For these bright excitons recombination occurs in the nanosecond time scale. Two dark exciton states are found for electron $m_z = +\frac{1}{2}$ ($-\frac{1}{2}$) and $m_z = +\frac{3}{2}$ ($-\frac{3}{2}$) for the hole. The dark exciton states are so-called because of the extremely low probability of undergoing radiative recombination due the not obeyed optical selection rules. However, emission from dark exciton is experimentally observed under applied external magnetic field [3]. After the exciton recombines, the quantum dot becomes empty. Hence, the photon emitted in such a process has exactly energy of the exciton, E_{X_0} . This energy is given by :

$$E_{X_0} = E_e + E_h - V_{eh}, \quad (2.1)$$

where E_e is the electron energy, E_h is the hole energy and the Coulomb interaction energy between electron and hole is expressed by $V_{eh} = e^2/4\epsilon r^2$. In the Coulomb interaction, e is the electron charge, ϵ is the dielectric constant of the semiconductor material and r is the distance between the particles. Coulomb interactions are determined by both the quantum dot composition and importantly by its dimensions. Because of such strong electrostatic interactions within the quantum dot, the nature of excitonic transitions is

identified by the photon emission energy. Two excitons can coexist simultaneously in the same quantum dot or the quantum dot can be electrically charged, meaning that an unpaired charge carrier (electron or hole) is populating the dot. If an additional electron is in the quantum dot, the energy of the exciton gains additional Coulomb terms:

$$E_{X^-} = 2E_e + E_h - 2V_{eh} + V_{ee}. \quad (2.2)$$

The negatively charged exciton X^* is characterized by two electron-hole Coulomb interaction and the interaction between the two electrons residing in the dot, V_{ee} . We refer to biexciton state (XX) when the quantum dot is occupied by two excitons.

$$E_{XX} = 2E_e + 2E_h - 4V_{eh} + V_{ee} + V_{hh}. \quad (2.3)$$

After the recombination of one of these two excitons, the quantum dot goes to the exciton state and a photon is emitted with energy equal to:

$$E_{XX} - E_{X_0} = E_e + E_h - 3V_{eh} + V_{ee} + V_{hh}. \quad (2.4)$$

This photon emission is referred to as biexciton emission and because of multi-particles Coulomb interactions occurs in general at a different energy compared to the exciton emission. In the following the photon obtained in the transition from biexciton to exciton will be denoted with XX and the photon emitted in the exciton recombination will be indicated with X_0 .

Typical quantum dot photoluminescence (PL) spectra acquired for a single quantum dot are shown in Fig. 2.1**b**. The luminescence is recorded upon above-bandgap laser excitation of the surrounding material. In this particular case, the quantum dot is embedded in a semiconductor nanowire. Upon laser excitation, photo-generated charges in the nanowire migrate into the quantum dot. The population of excitons the quantum dot increases as a function of the laser pump power, and as a result, the collected photoluminescence of the quantum dot presents a variety of transitions at different emission energy. At low excitation power density, 5 and 12 W/cm² we observe only a single emission peak that is ascribed to the exciton recombination with energy E_{X_0} . By increasing the excitation power, we increase the average excitonic population in the quantum dot and thereby observe both biexciton and exciton emission. Biexciton and exciton photons are emitted in a cascade, in which first the biexciton emission occurs and then the exciton recombines. However, because of the 1 second integration time of the acquisition, the measurements are not sensitive to the nanosecond time difference in the radiative cascade. At a power density of 200 W/cm² and higher, the quantum dot is filled with more than two excitons. For the Pauli exclusion principle, only two electrons can occupy the conduction band ground state provided they have an opposite spin. The same concept holds for holes in the quantum dot valence band. Electrons and holes in excess created with increased excitation occupy higher excited states, such as p-shell and d-shell, whose recombination yields higher energy photons [4].

2.2 Exciton fine-structure splitting and entanglement generation

In the previous section, we have considered how Coulomb interactions between electrons and holes in the quantum dot determines the exciton energy levels. If spin-spin interactions are neglected, the quantum dot ground state is spin-degenerate. However, the exciton energy level has a fine-structure due to the exchange interaction that depends on the spin orientation of the charge carriers, even without external applied magnetic field. The spin exchange interaction generates a splitting of the exciton energy levels depending on the symmetry of the state. We have thus two non-degenerate states:

$$\begin{aligned} |X_H\rangle &= |\downarrow\uparrow\rangle + |\uparrow\downarrow\rangle, \\ |X_V\rangle &= |\downarrow\uparrow\rangle - |\uparrow\downarrow\rangle. \end{aligned} \quad (2.5)$$

These two states represent the fine structure of the exciton level and their separation in the energy spectrum is defined as fine-structure splitting. The \downarrow, \uparrow arrows refer to the orientation of the electron spin, whereas \downarrow, \uparrow indicate the orientation of the hole spin. The states of Eq. 2.5 are hence characterized by a total spin equal to zero, which allows for radiative exciton recombination. The X_V state recombines emitting a vertically polarized photon (V) and the X_H emits and a photon with horizontal polarization (H). Fig. 2.2a shows the spectrum of a nanowire quantum dot detected for H and V polarization, respectively. We observe that the fine-structure splittings is visible on both exciton and biexciton emission, as the final state of a biexciton is the exciton. Fig 2.2b shows the oscillating energy of the exciton as a function of the detection polarization angle. The displayed case presents a fine-structure splitting of $\sim 10 \mu\text{eV}$ which has been chosen for the clarity of the explanation. However the range of fine structure splitting for quantum dots in nanowire range from $0.5 \mu\text{eV}$ up to $30 \mu\text{eV}$.

The fine-structure splitting of the exciton level has been widely studied in quantum dots because, by reducing the splitting to zero, the biexciton-exciton photon cascade produces polarization entangled photons [5]. Entanglement is a fundamental property of quantum mechanics occurring when the state of two particles cannot be described as the product state of the two separate particles. This fundamental property of quantum mechanics at first puzzled Einstein and his collaborators Podolski and Rosen in the early '30s [6]. The paradox was solved by John Bell and experimentally demonstrated in the seminal work of Aspect and collaborators in 1982 by using a photon cascade of polarization entangled photons in calcium atoms [7].

The polarization entangled state that we typically have in quantum dots is the following:

$$\Psi = \frac{1}{\sqrt{2}}(|HH\rangle + |VV\rangle). \quad (2.6)$$

In the presence of a perfect entangled state, both photons emitted in the biexciton-exciton cascade travel in a superposition of H and V polarization. However, when

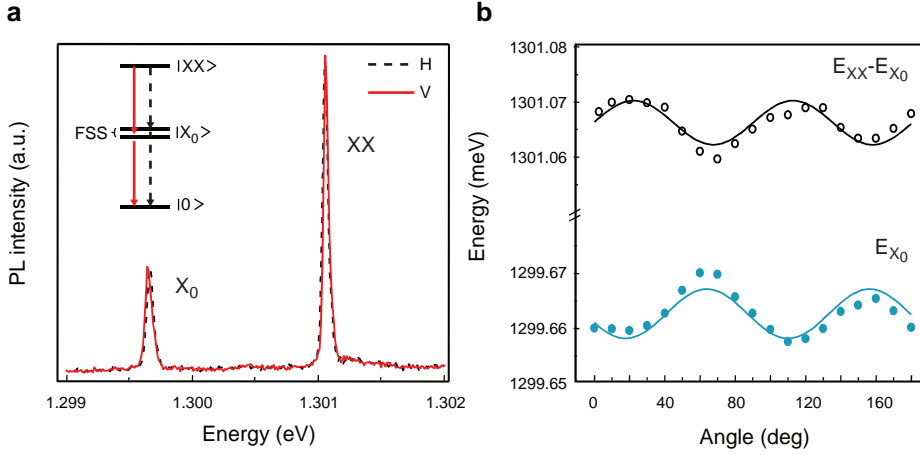


Figure 2.2: Single quantum dot spectroscopy. **a**, PL spectrum of exciton and biexciton emission for horizontal (black dashed curve) and vertical (red curve) linear polarization. **b**, Peak energy of exciton and biexciton emission acquired while scanning the linear polarization angle. The figure is adapted from: D. Dalacu, K. Mnaymneh, J. Lapointe, X. Wu, P.J. Poole, G. Bulgarini, V. Zwiller, M.E. Reimer, *Nano Lett.* **12**, 5919–5923 (2013).

determining the polarization state of one of the two photons with a measurement, the state of the other photon is automatically projected. In other words, since both photons are described by a single wavefunction, by measuring one photon we gain knowledge on the state of the other photon and this persists even by rotating the polarization basis of the measurement. For entangled photon emission from a quantum dot the fine-structure splitting should be zero in order to have a perfect polarization superposition of the emitted photons. A deterministic and efficient source of entangled photon pairs is an important resource for quantum computation and is sought after in quantum communication for the realization of a quantum repeater, as well as in quantum cryptography for the E91 protocol [8].

In order to reduce the fine-structure splitting in semiconductor quantum dots, an external electric field is often applied parallel to the main quantum dot confinement axis (i.e., along the height) [9]. Furthermore, the splitting is deterministically tuned to zero by the simultaneous application of electric field and strain [10]. Alternatively, zero or negligible fine structure splitting is obtained in symmetric quantum dots [11]. Because of the growth technique and the nanowire geometry, quantum dots grown in nanowire are predicted to have a zero or negligible fine structure splitting [12] and hence to be ideal for entangled photon generation. However, asymmetry in the crystalline potential in the quantum dot can be found even in quantum dots that are symmetric in shape. This drawback is mainly due to alloying inhomogeneity inside the quantum dot due to the random position of individual atoms.

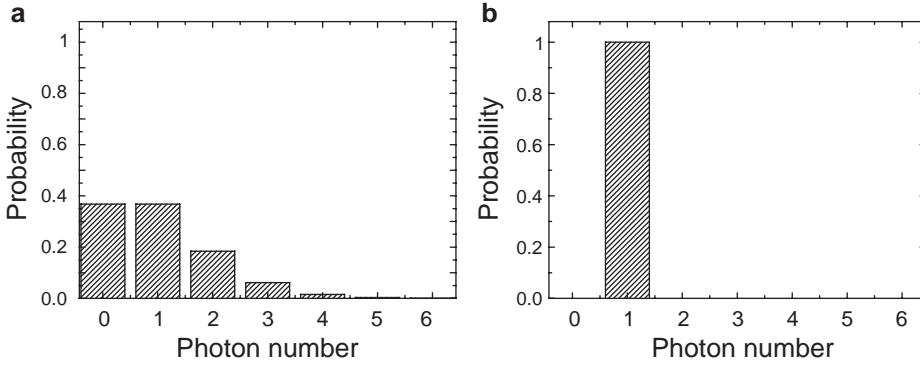


Figure 2.3: Photon correlation measurements. **a**, Photon number probability in a classical light source emitting on average one photon per pulse. **b**, Statistical probability of the photon number measured for a nonclassical light source: a single-photon emitter.

2.3 Photon statistics

Measuring the photon statistics is a powerful tool to characterize a light emitter. Laser light, for instance, follows Poissonian statistics. Let us assume an attenuated laser pulse with an average number of photons per pulse $\langle n \rangle = 1$. If we gather statistics on the number of photons per laser pulses we obtain the histogram shown in Fig. 2.3a. The number of photons per pulse is described by Poissonian statistics. Even though the average photon number is one, we have equal probability of having zero photons as one photon per pulse. Moreover, the probability of having more than one photon per pulse is not negligible and in detail, the variance of the photon number equals the average photon number: $\langle n^2 \rangle = n$ [13]. A non-classical light source behaves completely different and its emission probability is described by sub-Poissonian statistics. The statistics measured for an ideal single-photon source is presented in Fig. 2.3b. The probability of measuring one photon is 100 % and therefore there is no probability of measuring zero photons as well as zero occurrences of multi-photon emission. Such statistics is representative of a photon number state [13], also called Fock state, and is characterized by variance $\langle n^2 \rangle = 0$. The experimental method to determine sub-Poissonian emission statistics consists of measuring the second-order correlation function, $g^{(2)}(\tau)$. The first second-order correlation measurement setup ever realized was build by Hanbury Brown and Twiss for their stellar interferometer [14]. The measurement setup consists of a beam splitter having at both output ports two fast photodetectors. The photons impinging on the detectors are counted. In particular, the time delay between photons detected from detector 1 and photons detected from detector 2 is recorded in order to obtain a histogram of detection events that reflects the photon statistics of the source. A true single-photon source never generates simultaneous detection events at both detectors (i.e., at time delay $\tau = 0$). Hence, a perfect source of single photons has $g^{(2)}(0) = 0$

as shown in Fig. 2.4a. The broadening of the probability dip is related to the lifetime of the source and the pump rate, expressing the probability of re-excitation and emission of a second photon in a short time interval. The $g^{(2)}(\tau)$ measurement, often referred to as antibunching experiment, provides signature of single-photon emission whenever $g^{(2)}(0) < 0.5$. In fact, a source emitting two photons at a time, has a probability of 0.5 to give two simultaneous clicks at both detectors, with the other 0.5 resulting from events with both photons going to the same detector. A coherent source of photons, such as a laser, exhibits a constant coincidence probability as a function of time delay. The same would be obtained from a source consisting of many emitters [15].

Antibunched light from a single-photon source was first demonstrated in 1977 utilizing sodium atoms [16], whereas it has been first measured on a single quantum dot by Michler and co-workers in 2000 [17, 18]. For this measurement the emission of a single exciton is filtered and sent to a Hanbury Brown and Twiss setup. The final state of the quantum dot after the exciton emission is the vacuum, that means that the quantum dot must be populated again for another exciton to recombine. As a result the emission of a single exciton is antibunched. Because of discrete energy levels and the ability to emit single photons, the duality of atoms and quantum dots is often remarked by referring to quantum dots as *artificial atoms* [19]. Fig. 2.4b shows a cross correlation measurement obtained from a quantum dot in nanowire. Here, the biexciton emission is sent to detector 1, starting the correlation measurement, and the exciton is sent to detector 2 to detect the cross-correlated detection events. Since biexciton and exciton are emitted in a photon cascade we observe light bunching, that is a very high probability to detect the exciton emission after the biexciton has been detected. Towards negative delay time we observe antibunching because no exciton can be emitted before the biexciton recombines.

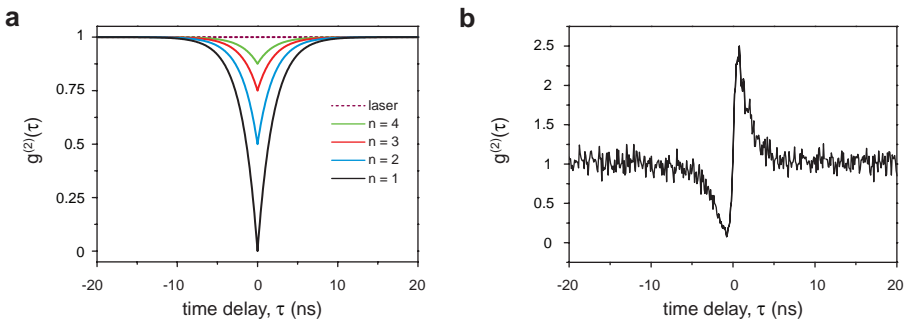


Figure 2.4: Photon correlation measurements. **a**, Expected correlation measurements for different sources under continuous excitation. In the calculation the total emission lifetime is set to 2 ns for all the curves. **b**, Cross correlation measurement of the biexciton-exciton cascade in a quantum dot in nanowire waveguide.

2.4 Photon coherence

As discussed in the previous section, from a statistical point of view, an ideal single-photon source has zero probability of multi-photon emission events. We conclude this chapter by introducing another characteristic of single photons that is of fundamental importance for quantum information applications: the photon coherence.

Coherence is the property that defines the phase stability of light or more in general of a quantum state. The coherence time, T_c , of a photon is the time duration during which phase correlations in the photon wavepacket are maintained. In other words, the coherence defines how monochromatic is a light source. The length over which phase correlations are maintained is defined as the coherence length $L_c = cT_c$, where c is the speed of light. Such phase correlations are measured by interfering the electromagnetic field of the photon for example using a Michelson interferometer as the one presented in the schematics of Fig. 2.5a. Let us assume such monochromatic, collimated light source entering the Michelson interferometer. The propagation of the electric field at the input of the beam splitter, \mathcal{E}_0 , is described by a plane wave that is split into \mathcal{E}_1 and \mathcal{E}_2 at the two arms of the interferometer. After reflections at the mirror, the electric field at the output is:

$$\mathcal{E}_{out} = \mathcal{E}_1 + \mathcal{E}_2. \quad (2.7)$$

The electric field component acquire phase by traveling the interferometer arms.

$$\mathcal{E}_{out} = \frac{1}{2}\mathcal{E}_0 e^{i\frac{4\pi}{\lambda}L_1} + \frac{1}{2}\mathcal{E}_0 e^{i\frac{4\pi}{\lambda}L_2}, \quad (2.8)$$

where the distance between the beam splitter and the two mirrors is given by L_1 and L_2 , respectively. The relative phase shift of the photons at the output is equal to $\phi = \frac{4\pi}{\lambda}(L_2 - L_1)$. When recombined at the beam splitter photons interfere and as a consequence the intensity at the output port oscillates with maxima observed for $\phi = m \cdot 2\pi$. Importantly, the same effect is observed for just a single photon entering the interferometer [20]. Neglecting interactions with the environment, the electromagnetic field of a perfectly monochromatic source maintains indefinitely its phase coherence during propagation. The period of intensity oscillations measured at the output port as a function of the mirror displacement is determined by the photon wavelength. Interference fringes will be infinitely observed for a perfectly monochromatic source. However, a realistic photon source emit in a broader range of frequencies and its coherence is time dependent. As a result, the photon electromagnetic field loses phase coherence during propagation. The temporal coherence of light is quantified by the first-order correlation function $g^{(1)}(\tau)$ defined as:

$$g^{(1)}(\tau) = \langle \mathcal{E}^*(t)\mathcal{E}(t+\tau) \rangle / \langle |\mathcal{E}(t)|^2 \rangle > \quad (2.9)$$

where $\langle \dots \rangle$ indicates the average over a long time interval. An example of a $g^{(1)}(\tau)$ for a realistic source with an exponential decay of the coherence in time is shown in

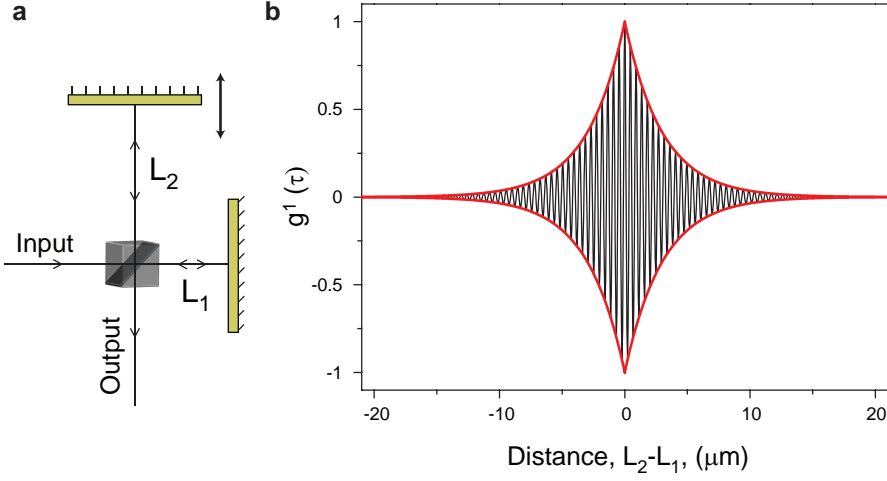


Figure 2.5: Measuring the photon coherence length. **a**, Schematics of a Michelson interferometer. **b**, Decay of the interference fringes for a source emitting at 900 nm having a coherence length of $3\text{ }\mu\text{m}$ and Lorentzian lineshape. $\tau = \frac{L_2 - L_1}{c}$, where c is the speed of light.

Fig. 2.5**b**. The $g^{(1)}(\tau)$ measurement shows the envelope of the interference oscillations with an exponential decay, $e^{-\tau/T_2}$, with $\tau = \frac{L_2 - L_1}{c}$, which represents the temporal decay of the source coherence. The resulting envelope determines the shape of the photon wavepacket. For clarity, Fig. 2.5**b** shows a very short coherence time, $T_2 = 10\text{ fs}$, corresponding to a coherence length $L_c = 3\text{ }\mu\text{m}$. As a consequence, when $L_1 - L_2$ is larger than $15\text{ }\mu\text{m}$, the photons do not any longer interfere. We note that in a real measurement, however, the intensity of the electric field is measured at the interferometer output for evaluating the coherence of a light source. The intensity, I , of the electric field is measured by detecting the photons and thus the outcome of the measurements follows

$$I(\tau) = \frac{1}{2}I_0(1 - \text{Re}[g^{(1)}(\tau)]), \quad (2.10)$$

as shown in the measurements presented in chapter 7 of this thesis. The fundamental limit to the temporal decay of the coherence owes to the uncertainty in the photon emission time, which is statistically expressed by the emission lifetime, T_1 . From the Heisenberg uncertainty principle, the indeterminate emission time reflects in a wider energy spectrum. Therefore, when measuring many photons emitted from the same light source we can measure the statistical distribution of the photon emission energy. The statistical distribution that we expect from such an ideal source, only limited by the uncertainty on the emission time, is Lorentzian with full-width half-maximum (FWHM) equal to $\Delta f = 1/2\pi T_1$ [21]. A photon source with a lifetime of 1 ns, typical value for quantum dots, has a lifetime-limited (or Fourier transform-limited) linewidth of 80 MHz, that is in energy equal to $0.33\text{ }\mu\text{eV}$.

Non-ideal sources are subject to additional broadening mechanisms than that derived from the Heisenberg uncertainty relation and, as a result, the coherence time of the photon source is expressed by

$$\frac{1}{T_2} = \frac{1}{2T_1} + \frac{1}{T_2^*}, \quad (2.11)$$

where the pure dephasing term, T_2^* , can arise from multiple factors due to diverse noise sources [15]. The resulting linewidth of the emitted photon is a Lorentzian with FWHM of $\Delta f = 1/\pi T_2$. [21]

Given the short lifetime of quantum dot emission, an emission linewidth close to the Fourier transform-limit cannot be resolved with a single grating spectrometer. An alternative method to Michelson interferometry for determining the quantum dot emission linewidth is measuring the transmission through a high-finesse tunable Fabry-Perot cavity. Another option to measure the linewidth of a transitions is resonant fluorescence. In this technique, a very narrow bandwidth laser is scanned through the exciton absorption resonance and the intensity of the resulting photoluminescence is recorded as a function of the laser energy. Alternatively, the transmission of the laser scanned through the quantum dot resonances. This latter technique is often referred to as laser transmission spectroscopy. We stress that these spectroscopy methods does not directly measure the properties of the emitted photons but rather those of the absorption lines.

We perform single-photon coherence measurements utilizing a Michelson interferometer; results are presented in chapter 7. Measurements of the coherence length of a photon are sensitive to different noise frequency depending on the integration time of the acquisition. When the emission linewidth is measured via a Michelson interferometer, the signal is integrated over photons emitted over a time scale of several minutes or even hours for high resolution interfererograms. The measurement is thus effected by both the slow and fast processes which are contributing to the broadening of the emission line. As a consequence, the Lorentzian profile is additionally broadened by a Gaussian lineshape, resulting in a Voigt profile (i.e., the convolution of Lorentzian and Guassian). Details on the emission line broadening are reported in chapter 7. Conversely, the interference of two consecutive photons emitted from the same quantum dot, with the second photon delayed by the repetition period of the excitation laser, is only sensitive to fast dephasing processes that occur during the laser repetition period [22]. Slow dephasing processes are usually attributed to charge noise: the charge environment in the vicinity of the quantum dot varies on a slow time scale and by Coulomb interaction the energy of the quantum dot emission is varied. For quantum dots in nanowire a source of traps for charges arises from the possibility of growing InP nanowires in both wurtzite and zincblende crystal phase. The interface between two different crystalline structures offers efficient trapping of charge carriers because each crystal phase has a different energy bandgap [23]. Other common trap sites are attributed to contaminants, point impurities in the lattice as well as dangling bonds located at the nanowire surface. Fast processes which decrease the photon coherence time are attributed to spin-flips origi-

nating from the interaction with the spin of the quantum dot nuclei [24]. This effect is particularly important for semiconductor composed of the alloy of group III and group V elements, both presenting non-zero nuclear spin.

2.5 References

- [1] P. Yu and M. Cardona, *Fundamentals of Semiconductors*, Springer (1999).
- [2] Y.H. Huo et al., A light-hole exciton in a quantum dot. *Nat. Physics* **10**, 46–51 (2014).
- [3] B.J. Witek et al., Measurement of the g-factor tensor in a quantum dot and disentanglement of exciton spins. *Phys. Rev. B* **84**, 195305 (2011).
- [4] M. Korkusinski, M. Zielinski, and P. Hawrylak, Multiexciton complexes in InAs self-assembled quantum dots. *J. Appl. Phys.* **105**, 122406 (2009).
- [5] N. Akopian et al., Entangled photon pairs from semiconductor quantum dots. *Phys. Rev. Lett.* **96**, 130501 (2006).
- [6] A. Einstein, B. Podolsky, and N. Rosen, Can quantum-mechanical description of physical reality be considered complete?. *Phys. Rev.* **47**, 777–780 (1935).
- [7] A. Aspect, P. Grangier, and G. Roger, Experimental realization of Einstein-Podolsky-Rosen-Bohm Gedankenexperiment: a new violation of Bell's inequalities. *Phys. Rev. Lett.*, **49**, 91–94 (1982).
- [8] A.K. Ekert, Quantum cryptography based on Bell's theorem. *Phys. Rev. Lett.* **67**, 661–663 (1991).
- [9] A.J. Bennett et al., Electric-field-induced coherent coupling of the exciton states in a single quantum dot. *Nat. Phys.* **6**, 947–950 (2010).
- [10] R. Trotta et al., Universal recovery of the energy-level degeneracy of bright excitons in InGaAs quantum dots without a structure symmetry. *Phys. Rev. Lett.* **109**, 147401 (2012).
- [11] A. Mohan et al., Polarization-entangled photons produced with high-symmetry site-controlled quantum dots. *Nat. Photon.* **4**, 302–306 (2010).
- [12] G. Singh and G. Bester, Nanowire quantum dots as an ideal source of entangled photon pairs. *Phys. Rev. Lett.* **103**, 063601 (2009).
- [13] C.C. Gerry and P.L. Knight, *Introductory Quantum Optics* Cambridge University Press (2004).
- [14] R. Hanbury Brown, R.Q. Twiss, Correlation between photons in two coherent beams of light. *Nature* **177**, 27–29 (1956).
- [15] C. Santori, D. Fattal, Y. Yamamoto, *Single-photon Devices and Applications*, Wiley-VCH (2010).

- [16] H.J. Kimble, M. Degenais and L. Mandel, Photon antibunching in resonance fluorescence. *Phys. Rev. Lett.* **39**, 691 (1977).
- [17] P. Michler et al., A quantum dot single-photon turnstile device. *Science* **290**, 2282 (2000).
- [18] P. Michler et al., Quantum correlation among photons from a single quantum dot at room temperature. *Nature* **406**, 968–970 (2000).
- [19] R. Bratschitsch and A. Leitenstorfer, Quantum dots: Artificial atoms for quantum optics. *Nat. Mater.* **5**, 855–856 (2006).
- [20] P. Grangier, G. Roger and A. Aspect, Experimental Evidence for a Photon Anticorrelation Effect on a Beam Splitter: A New Light on Single-Photon Interferences. *Eurphys. Lett.* **1**, 173 (1986).
- [21] M. Fox, *Quantum Optics*, Oxford (2006).
- [22] Y.-M. He et al., On-demand semiconductor single-photon source with near-unity indistinguishability. *Nat. Nanotech.* **8**, 213–217 (2013).
- [23] N. Akopian, G. Patriarche, L. Liu, J.-C. Harmand and V. Zwiller, Crystal Phase Quantum Dot. *Nano Lett.* **10**, 1198–1201 (2010).
- [24] A.V. Kuhlmann et al., Charge noise and spin noise in a semiconductor quantum device. *Nat. Phys.* **9**, 570–575 (2013).

CHAPTER 3

Realization of semiconductor single-photon sources

In this chapter, we survey the most established methods for the growth of heterostructured *optically active* quantum dots. The definition *optically-active* refers to quantum dots with strong optical absorption and emission in the visible and near-infrared spectrum, usually based on direct-bandgap semiconductors. In the first part of the chapter we discuss advantages and disadvantages of the most common growth methods. Second, we describe the state of the art of photon collection efficiency from quantum dots by analyzing the most successful dielectric photonic structures with particular focus on nanowire waveguides.

Part of this chapter is adapted from:

G. Bulgarini, M.E. Reimer, V. Zwiller, *Appl. Phys. Lett.* **101** (11), 111112 (2012).

3.1 Self-assembled quantum dots

The first quantum dots that have been spectroscopically studied were interface fluctuations quantum dots, consisting of local monolayer fluctuations in thin quantum wells [1]. However, we owe most of the study on semiconductor quantum dots to the Stranki-Krastanov growth method. In such approach, quantum dots are grown through self-assembly induced by strain. During the growth of a semiconductor heterostructure with a few percent lattice mismatch (e.g., 7 % for InAs on GaAs), strain accumulates in the top layer and, at a critical layer thickness, the semiconductor relaxes the stress by growing as islands, that naturally provide quantum confinement.

Self-assembly is to date the most established growth method for quantum dots and most of the research in the field of optically-active quantum dots is performed on this system. Self-assembled quantum dots have gained popularity among researchers because of their good optical quality, expressed in terms of brightness and emission linewidth, owing to the possibility of growing islands free of crystal defects by tuning the growth parameters. However, in order to preserve the optical properties from surface defects, quantum dots are capped with other semiconductor material, usually the same used for the first layer. This represents an issue for photon collection efficiency that will be addressed in section 3.3. Another important issue is the quantum dot location. Since the growth is driven by strain, the nucleation of these quantum dot is usually random. Great effort has been done during recent years to control the nucleation site in order to isolate individual quantum emitters and various methods have been developed [2, 3, 4].

An alternative route to the self-assembly of quantum dots is by chemical synthesis of colloidal quantum dots, or nanocrystals. Colloidal quantum dots can be produced from a large variety of elements, more commonly II-VI semiconductors but also group IV materials like silicon. To this category of quantum dots we owe the first measurement of antibunched light emission from a nanostructured semiconductor [5]. By tuning the reaction conditions it is possible to go from spherically shaped nanocrystals to elongated structures, known as nanorods, or more complicated geometries. Although very versatile in shape and composition, these quantum dots suffer from bleaching and blinking of the emission and are thus not considered among leading candidates as reliable single-photon sources for quantum communication applications.

3.2 Nanowire quantum dots

The growth of a disk-shaped heterostructure on the axis of a semiconducting nanowire is a recent technique for achieving individual quantum dots. Nanowires are one-dimensional structures, which therefore guarantee two natural confinement directions for the quantum dots that are grown on their axis. The standard growth mechanism is the vapor-liquid-solid mechanism catalyzed by gold nanoparticles. The growth is initiated by semiconductor material (usually III-V) that is incorporated in the gold catalyst, forming an

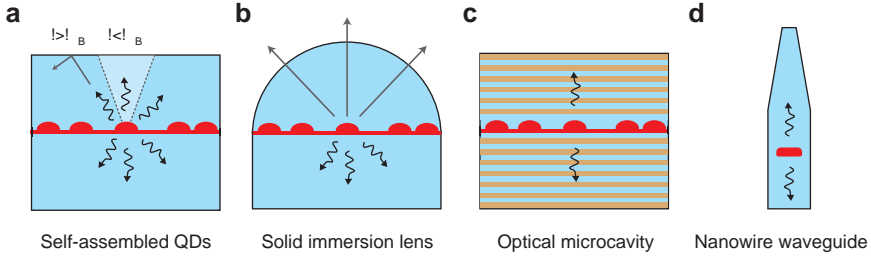


Figure 3.1: Different photon collection strategies. **a**, Basic configuration of a self-assembled quantum dot sample. **b**, A solid-immersion lens is positioned at the top of the sample to avoid total internal reflection. **c**, Quantum dots included in a microcavity sandwiched between dielectric Bragg reflectors. **d**, Nanowire waveguides utilize the coupling to waveguide modes and, in remarkable difference with **a**, **b** and **c**, provide only a single quantum dot per structure.

alloy. After saturation of the group III element is reached in the alloy, material starts to precipitate in the alloy droplet starting a layer by layer deposition. The radial dimension of the layer is defined by the dimension of the alloy, very similar to those of the catalyst, whereas the height is defined by the growth time. Therefore, by utilizing a small enough gold particle as catalyst for the growth, it is possible to grow nanowires with tens of nanometer diameters and micrometers in length.

The ability to position only one quantum dot per nanowire is very advantageous for this technique and additionally, the nucleation of the nanowire on the growth chip can be easily controlled by defining the gold catalyst position via electron beam lithography [6]. In addition, nanowire growth features an unprecedented material freedom. Because of their geometry and small dimensions, nanowires support stress much better than planar growth and thus materials can be grown in crystal orders that are not allowed in bulk [7] or several materials can be combined together to achieve novel functionalities [8].

3.3 Single-photon collection strategies

The most studied quantum dots, grown by self-assembly, suffer from the fact that the quantum emitter is buried into the host semiconductor matrix. This host material has typically a high refractive index ($n \sim 3.5$ for both InP and GaAs in the near-infrared spectral range) and thus total internal reflection at the semiconductor-air interface makes the out-coupling of photons very inefficient. As displayed in Fig 3.1a, photons emitted at an angle θ smaller than the Brewster's angle, $\theta_B \sim 16^\circ$ for GaAs, can propagate to the far field. Photons emitted at higher angles than θ_B , that represent the largest fraction of the radiated light, are trapped inside the host semiconductor matrix by means of total internal reflection. In addition, the photons emitted downwards have no possibility to reach the collection optics that in Fig. 3.1 is meant to be positioned at the top of the sample.

3.3.1 Solid immersion lens

A solution to the total-internal reflection problem is to position a solid-immersion lens on top of the quantum dot, as depicted in Fig. 3.1b. Given the spherical shape of the lens and the quantum dot being positioned in the center of the lens, all photons emitted from the dot are reaching the lens surface with normal incidence, thereby overcoming the total internal reflection problem. This method was first employed by Zwiller and Bjork to improve the light collection efficiency [9]. The refractive index of commercial solid immersion lenses is at best of $n \simeq 2$ and thus a minor but not negligible internal reflection still occurs at the host semiconductor–lens interface. An interesting alternative solution to conventional solid immersion lenses made of quartz are polymer films that can be deposited on quantum dots and shaped into a lens-like structures [10].

3.3.2 Optical microcavity

In Fig. 3.1c the quantum dots are embedded in an optical cavity consisting of a semiconductor layer sandwiched between two distributed Bragg reflectors. The archetype of this kind of structures is the Fabry-Perot resonator, that consists of two highly reflective mirrors, facing each other at a distance d . Between the two mirrors, light is confined by undergoing multiple reflections. The cavity allows resonant standing waves at multiples of the frequency $f = c/2d$, where c is the speed of light. The quality factor $Q = f/\Delta f$ defines the bandwidth, Δf , of the resonator [11]. The quality factor can be also seen in terms of photon lifetime in the cavity: the higher the quality factor, the longer a photon is trapped inside the cavity by internal reflection.

Microcavities use Bragg reflectors instead of mirrors. A distributed Bragg reflector consists of a stack of dielectrics with alternating low and high index of refraction, each layer with thickness corresponding to a quarter wavelength. The structure is designed such as the quantum dot is located between two Bragg reflectors and the quantum dot emission couples to the cavity modes. Such coupling results in a Purcell enhancement of the spontaneous emission rate [12]. Explicitly, the spontaneous emission rate is modified by the environment of the quantum dot and the transition rate depends on the density of available modes inside the cavity. Microcavity are thus utilized to accelerate the spontaneous emission rate of quantum dots in order to improve the photon rate of the emission. The increment in recombination rate is proportional to the quality factor Q and inversely proportional to the modal volume. For the enhancement of the spontaneous emission, the quantum dot must be placed at an anti-node of the cavity field and the emission frequency must precisely match the frequency of the cavity mode. In order to match this stringent condition, the quantum dot emission frequency is tuned by varying the sample temperature as well as applying external electric or magnetic field.

A planar microcavity can be etched in order to obtain light confinement in all three directions into a so-called micropillar. The first demonstration of Purcell enhancement of the quantum dot spontaneous emission rate in such micropillar cavities were performed

using GaAs/AlAs micropillars [13]. In such structures, light is confined both in the axial direction as in a Fabry-Perot resonator and in the radial direction by total internal reflection between the high refractive index semiconductor of the pillar and vacuum. The semiconductor compounds often utilized for the dielectric stack are AlAs/GaAs or AlGaAs/GaAs. Micropillars ensure high Q factors and directionality of the emission, i.e. along the axial direction, which favors the collection of light. Recent work has shown a collection efficiency approaching 80 % at saturation of the exciton emission [14]. The disadvantage of this structures is that the single-photon emission quality is deteriorated under such high pumping power by cavity feeding effects [14, 15, 16].

An alternative route to microcavities is represented by photonic crystals [17]. Photonic crystals, not shown in the schematics, are usually two-dimensional dielectric slabs structured with a periodic variation of refractive index. Similarly to the dispersion of electronic degrees of freedom in solids, photonic crystals have allowed and forbidden photonic energy bands for light propagation. By placing a defect on a perfect photonic crystal lattice (i.e., 3 contiguous holes removed from the crystal for L3 cavities [18]), very high Q factor cavities can be obtained and large Purcell effects due to the very small modal volume. A quantum dot located on this photonic crystal defect can be tuned in resonance with the cavity mode [19].

3.3.3 Tapered nanowire waveguide

The strategy that we follow in this thesis for enhancing the light emission properties and light collection efficiency from quantum dots is the nanowire waveguide, Fig. 3.1d. Nanowire waveguides are one-dimensional semiconductor structures with typically cylindrical or hexagonal cross-section. Waveguides are not based on a periodic variation of refractive index as in microcavities, however the refractive index difference between the waveguide and its surroundings is very important as it governs total internal reflection. In a ray-optics description, light traveling in the waveguide undergoes total internal reflection at the waveguides edges if the angle of incidence is bigger than the critical angle $\theta_c = \arcsin(n_2/n_1)$. The most commonly known waveguides, optical fibers, have changed telecommunication during the last century. Optical fibers are usually composed of a fiber core with refractive index n_1 and a cladding with refractive index $n_2 < n_1$. Fig. 3.2 shows the first three waveguide transversal modes allowed in a one-dimensional slab waveguide composed of a steep variation of refractive index from n_1 to n_2 , with $n_1 > n_2$. Light is confined inside the higher refractive index material, with thickness d , although some of the electric field leaks outside the waveguide. The electric field of the first mode in Fig. 3.2 has a Gaussian distribution of the electric field. Unlike propagation of a Gaussian beam in vacuum, a guided mode maintains the Gaussian profile without spreading in the transverse direction [11]. Higher orders waveguide modes have nodes (zero electric field) along the transversal direction of the waveguide. These modes are allowed for shorter photon wavelength or by enlarging the waveguide diameter for a fixed photon wavelength. Then electric field distribution during propagation in the waveguide

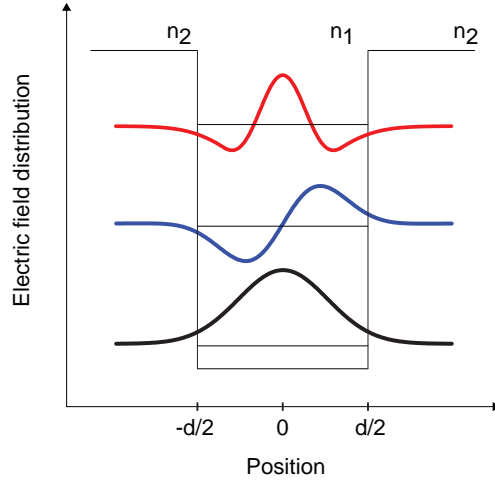


Figure 3.2: Propagating modes in a one-dimensional waveguide. A waveguide of thickness d consisting of a steep variation of refractive index from n_1 to n_2 , with $n_1 > n_2$. The electric field distribution of the first three guided modes allowed in the waveguide is plotted.

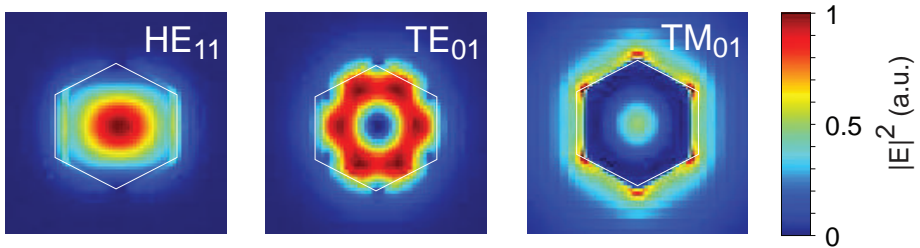


Figure 3.3: Simulations of a nanowire waveguide. Finite-difference time-domain simulations of a three-dimensional nanowire waveguide with hexagonal cross-section. The intensity of the electric field is shown for the first three guided modes and is coded in color.

for higher order modes deviates from a Gaussian profile.

Fig. 3.3 displays finite-difference time-domain simulations a three-dimensional InP waveguide in vacuum. We use here a hexagonal symmetry in the plane perpendicular to the propagation direction and the refractive index of InP, $n \simeq 3.37$ at 950 nm [20]. By considering a three dimensional waveguide with cylindrical symmetry, or in first approximation hexagonal symmetry, we have two degenerate fundamental waveguide modes, HE_{11x} and HE_{11y} , both propagating with a Gaussian electric field distribution. The confinement of the light is two-dimensional and thus results in two degenerate waveguide modes. Fig. 3.3 shows the first three allowed modes in a nanowire waveguide with hexagonal symmetry. The electric field intensity is plotted in a plane perpendicular to the propagation direction along the waveguide. A nanowire waveguide where photons are emitting in a Gaussian mode is very important for practical implementation of single-photon sources in technological application. Remarkably, the Gaussian profile is maintained in the far field by shaping the nanowire tip as a needle featuring a very small tapering angle ($1-2^\circ$). The emission mode adiabatically expands in vacuum conserving its profile, which is very favorable for the coupling of the quantum dot emission to optical fibers or other components of an optical network. Measurements of the far field emission profile are presented in chapter 5. Moreover, this out-coupling strategy enables a reduced emission angle that allows efficient light collection using objectives with limited numerical aperture [21]. The best results are however achieved only when the quantum dot is positioned on the waveguide axis [22]. An alternative to the tapered nanowire waveguide is the trumpet-like waveguide that instead expands the guided mode within the high refractive index material [23].

Finally, a back-reflecting gold mirror can be inserted at the base of the nanowire waveguide to reflect the downward emitted photons and increase the photon collection efficiency [24]. The presence of a mirror at the bottom of the nanowire induces a little cavity enhancement of the spontaneous emission rate. Further details are given in chapter 4. A general advantage of nanowire waveguides is that they operate over a broad spectral range [21]. Nanowire waveguides accommodate both exciton and biexciton emission for the generation of polarization-entangled photons and the coupling to waveguide modes do not require active tuning mechanisms.

3.4 Fabrication of the nanowire waveguide

In this section, we describe in more details the growth of nanowire waveguides which are investigated in this thesis. Two methods are employed for the growth of nanowires with embedded quantum dot and tailored tip: metal-organic vapour phase epitaxy (MOVPE) and chemical beam epitaxy (CBE).

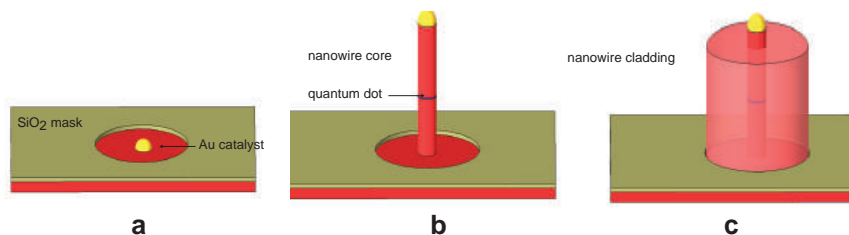


Figure 3.4: Nanowire growth. **a**, Gold catalyst is positioned in the middle of an aperture in a SiO_2 mask. **b**, Catalyzed vapour-liquid-solid growth of a thin nanowire quantum dot. **c**, Growth conditions are modified in order to promote growth from the InP substrate inside the SiO_2 mask. The nanowire core is homogenously clad by InP and the crystal structure of the core is transferred to the clad.

3.4.1 MOVPE growth

Metal-organic vapour-phase epitaxy is a well-known technique used for growing complex crystalline semiconductors. For the growth of compounds semiconductors, high purity precursors materials containing the chemical elements to be deposited, are inserted in the MOVPE reactor. In the reactor, the growth substrate is kept at a controlled temperature, typically a few hundreds $^{\circ}\text{C}$. The precursor materials, in vapour phase, undergo chemical reactions as they reach the substrate surface. Such chemical reactions create the conditions for the material to be epitaxially deposited onto the growth substrate. The versatility of this technique enables for the growth of compound semiconductors containing group III and group V materials.

In this thesis, InP nanowires are grown at a temperature of 420°C by the vapour-liquid-solid (VLS) growth mechanism. The VLS mechanism requires a metal catalyst particle to initiate the growth process. In our case, 20 nm gold colloids were dispersed on a (111)B InP substrate. The precursors used for InP growth were trimethyl-indium and phosphine. An $\text{InAs}_{25}\text{P}_{75}$ quantum dot is incorporated, typically in the middle of the growth process, by addition of arsine in the MOVPE reactor. The quantum dot height is set by the growth time (1-2 seconds) with arsine flow. After nanowire growth, the temperature was raised up to 500°C to favor radial versus axial growth. In this regime a shell is grown around the nanowire to match diameters suitable to waveguide. The shell growth time and temperature were carefully chosen to shape the nanowire geometry and obtain both an optimum nanowire diameter and small tip tapering angle. The total growth time defines the length of the nanowire waveguide.

3.4.2 CBE growth

Chemical beam epitaxy employs pure elements that are inserted pre-cracked in the reaction chamber. For the growth of InAsP/InP nanowire quantum dots using chemical beam epitaxy (CBE), trimethylindium (TMI) and pre-cracked PH_3 and AsH_3 sources are

utilized. The nanowires are grown on a SiO_2 -patterned (111)B InP substrate consisting of circular apertures carved in the oxide mask using electron-beam lithography and a hydrofluoric acid wet-etch. The diameter of this SiO_2 mask defines the final diameter of the nanowire waveguide. Gold (Au) was deposited in these apertures using a self-aligned lift-off process, which allows the nanowires to be positioned at known locations on the substrate [6]. The thickness of the deposited gold is chosen to give 20 nm diameter particles. Fig. 3.4 shows the main steps of the nanowire growth. The nanowire core is grown under conditions which promote VLS growth of pure wurtzite nanowires for gold particles of 20 nm in diameter. Catalyzed growth of defect-free wurtzite nanowire is obtained by controlling the TMI flux and using a temperature of 420 °C. The dot was incorporated by switching from a PH3 to an AsH3 overpressure for 3 s after approximately 200 nm of the nanowire core have been grown from the substrate surface. To clad the nanowire core and reach the optimal waveguide diameter, we used conditions that promotes growth from the InP substrate growth while suppressing VLS growth from the nanowire tip. However, VLS growth is not completely quenched as the clad nanowires are nearly twice as tall as the nanowire cores. Moreover, a tapered tip is obtained when the length of the nanowire overcomes the material diffusion length. As the nanowire gets longer, the substrate growth rate is thus decreased while the catalyzed growth is constant. Importantly, the crystal structure of the core is transferred to the cladding, which means that a pure crystalline nanowire core determines the phase purity of the final nanowire waveguide.

3.5 Photon collection from nanowire devices

In the final section of this chapter we analyze the case of nanowires lying on a substrate with photon collection for the top of the chip, thus the side of the nanowire. This situation, depicted in Fig. 3.5a, is found in the implementation of complex, electrically contacted devices [25, 26, 27]. Two main problems arise from using this geometry. First, photon polarization is altered by the dielectric anisotropy of the one-dimensional nanowire, which acts as a polarizer [28, 29, 30]. As a result, photons emitted from quantum dots in nanowires with polarization parallel to nanowire axis are more likely to be detected compared to photons polarized perpendicular to the nanowire [31, 32], thereby destroying the original polarization information. Second, photon collection is inefficient because most of the emission is directed towards the higher dielectric material, i.e., the substrate.

In this section we analyze the angular distribution of the emitted power for a quantum dot in a nanowire lying on a dielectric substrate. In our calculations, we fixed the distance of the quantum dot from the dielectric interface to 30 nm, assuming a nanowire diameter of 60 nm and the quantum dot to be positioned along the nanowire axis [33]. At this nanowire diameter, the quantum dot emission is not confined in the nanowire and only couples to the continuum of non-guided radiative modes [22, 34]. Such nanowire

dimensions are the most commonly used for electrically contacted doped nanowires, for example as light-emitting diodes or photodetector [35], or in electrically gated nanowires for manipulating electrons spins, where one-dimensional electrical transport is essential [25].

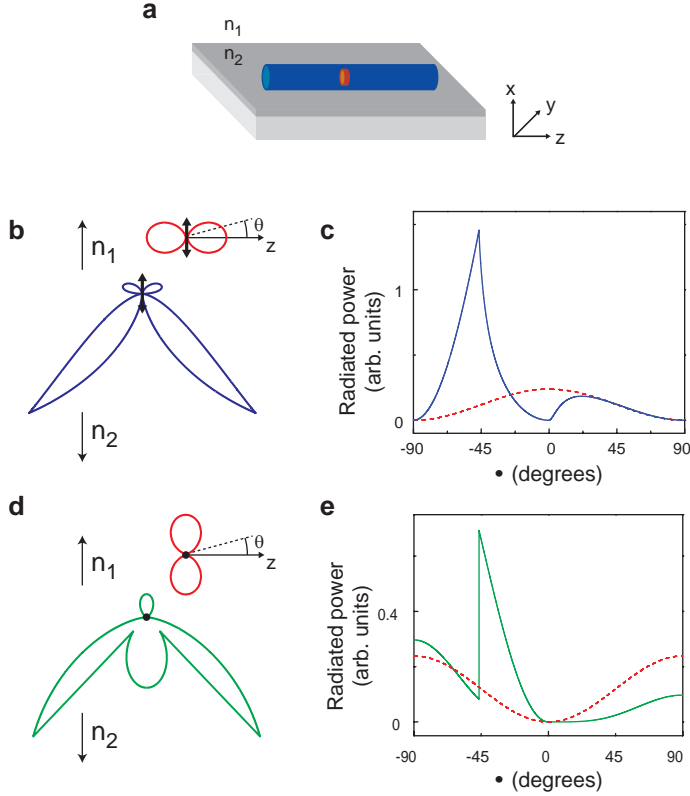


Figure 3.5: Emitted power distribution for a lying nanowire. **a**, Sketch of a lying quantum dot in nanowire sample. Calculated angular radiation pattern for an electric dipole (double arrow) positioned perpendicular **b**, or parallel **d**, to the interface between vacuum (n_1) and SiO₂ ($n_2 \simeq 1.45$). Insets show emission profiles in vacuum. **c**, Radiated power for a dipole perpendicular to the interface (solid) compared to vacuum (dashed). **e**, Power radiated by a dipole parallel to the interface compared to vacuum.

A single exciton confined in the quantum dot is modeled as an electric dipole lying in the xy plane, at the interface between vacuum (n_1) and SiO₂ (n_2). We model the emission pattern using the intrinsic dipole of the quantum dot, which consists of a component perpendicular and a component parallel to the dielectric interface. In Fig. 3.5**b**, we plot the emission angular distribution for $\lambda = 950$ nm in the case of a dipole aligned along x (i.e., perpendicular to the dielectric interface), and in Fig. 3.5**d** we plot the emission profile for a dipole oriented parallel to the y direction. In both cases,

we plot in the inset the emission profile of the same dipole in vacuum. As expected, most of the light is emitted by the dipole downwards, towards the higher refractive index dielectric, SiO_2 .

Explicitly, the density of available photonic modes is larger in a higher refractive index material ($n_2 > n_1$) and therefore, the emitter couples light into medium 2 with higher probability than into medium 1, thus increasing the total emission rate. This effect has been measured and exploited to improve light collection from nanocrystals [36] and molecules [37, 38] on transparent dielectric substrates. By increasing the n_2/n_1 ratio, the portion of photons emitted downwards can be maximized and the emission is collected from the substrate with efficiency approaching 100 % [38].

In the calculations of the radiation pattern, we have separated the quantum dot emission into two components: plane waves and evanescent waves, following the theory developed by Lukosz and Kunz [40, 41]. Plane waves propagate in vacuum and towards medium 2 with incidence angle lower than the Brewster's angle. In contrast, evanescent waves propagate from medium 1 to medium 2 at angles larger than the Brewster's angle, but with a transmission probability that depends exponentially on the distance of the dipole from the interface [40, 41]. In Fig. 3.5c,e we quantitatively compare the radiated power profile of a dipole perpendicular (c) and parallel (e) to the vacuum– SiO_2 interface (solid line) with that of the same dipole in vacuum (dashed line). As shown for both dipole orientations, the presence of the dielectric interface modifies the dipole emission. The total power radiated by the dipole at the interface is approximately double compared to a dipole completely surrounded by vacuum and over 80 % of the total emission is directed downwards. The anisotropy of the emission profile indicates that light collection from the top of the sample is not efficient. Hence, if the emitted light cannot be collected via the substrate the photon collection efficiency results to be poor in lying nanowire devices.

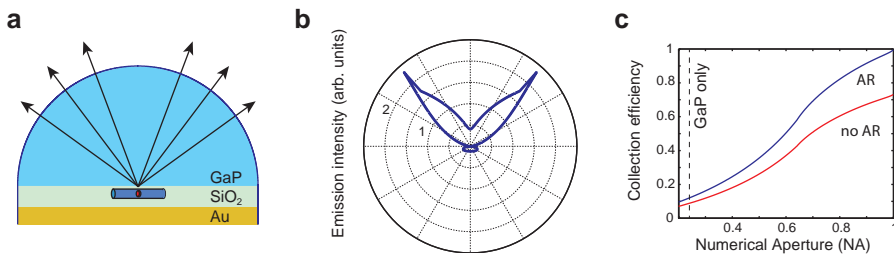


Figure 3.6: Emitted power distribution for a lying nanowire. **a**, Design of a nanowire embedded between a GaP solid immersion lens and a gold mirror. **b**, Calculated angular distribution of the light emitted from the quantum dot. The engineering dielectric stack surrounding the quantum dot results in a highly anisotropic emission, where most of the light is emitted towards the GaP layer. **c**, Collection efficiency calculated for a structure with (red curve) or without (blue) an anti-reflection coating on top of the solid immersion lens.

In Fig. 3.6 we propose a solution to this collection efficiency problem of lying nanowire devices. In Fig. 3.6a a nanowire with embedded quantum dot is sandwiched between a GaP/SiO₂(50nm) and SiO₂(500nm)/Au. The higher refractive index of the GaP layer compared to the thick SiO₂ layer at the bottom of the nanowire induces a high anisotropy of the quantum dot emission as first proposed by Chen et al [39]. The calculated angular distribution of the radiated power is shown in Fig. 3.6b. Most of the light is directed towards the GaP and since GaP is transparent in the near infrared wavelength range, high light collection efficiency is possible from the top of the sample. In our model, the GaP layer is shaped as a solid immersion lens with the quantum dot positioned in the center to avoid total internal reflection at the Brewster's angle at the GaP/vacuum interface. Considering the refractive index of GaP at 950 nm, that is $n=3.13$ [20], total internal reflection would occur at 18.6° thus making the solid immersion lens required in order to achieve high collection efficiency. A gold mirror, positioned at the bottom of the structure further directs light towards the top of the sample, thus increasing the probability of collecting the quantum dot emission. The collection efficiency of our proposed system is calculated in Fig. 3.6c. The red curve refers to the exact structure sketched in 3.6a. The structure presents no anti-reflection (AR) coating on top of the GaP solid immersion lens and therefore the dielectric mismatch between GaP and vacuum still represents a sizeable source of losses, i.e. back reflections. The blue curve refers to the case of an anti-reflection coating tailored for the quantum dot emission and added on the solid immersion lens. In this configuration, and considering the gold layer as a perfect mirror, the collection efficiency is higher than 80% for numerical aperture larger than 0.8. As most of the emission is directed towards the GaP, the calculated efficiency is rather robust against imperfections of the gold mirror. A dashed line indicates the case of no solid immersion lens. The effective numerical aperture, hindered by total internal reflection, limits in this case the collection efficiency to $\sim 10\%$.

3.6 References

- [1] O.Gywat, H.J. Krenner, J. Berezovsky, *Spins in Optically Active Quantum Dots*, Wiley-VCH (2010).
- [2] M.E. Reimer et al., Prepositioned single quantum dot in a lateral electric field. *Phys. Rev. B* **78**, 195301 (2008).
- [3] K.D. Jöns et al., Triggered Indistinguishable Single Photons with Narrow Line Widths from Site-Controlled Quantum Dots. *Nano Lett.* **13**, 126–130 (2013).
- [4] G. Juska, V. Dimastrodonato, L.O. Mereni, A. Gocalinska and E. Pelucchi, Towards quantum-dot arrays of entangled photon emitters. *Nat. Photon.* **7**, 527–531 (2013).
- [5] P. Michler et al., A Quantum Dot Single-Photon Turnstile Device. *Science* **290**, 2282 (2000).
- [6] D. Dalacu et al., Selective-area vapour-liquid-solid growth of InP nanowires. *Nanotechnology* **20**, 395602 (2009).
- [7] S. Assali et al., Direct Band Gap Wurtzite Gallium Phosphide Nanowires. *Nano Lett.* **13**, 1559–1563 (2013).
- [8] M. Hocevar et al., Growth and optical properties of axial hybrid III-V/silicon nanowires. *Nat. Commun.* **3**, 1266 (2012).
- [9] V. Zwiller and G. Bjork, Improved light extraction from emitters in high refractive index materials using solid immersion lenses. *J. Appl. Phys.* **92**, 660-665 (2002).
- [10] M. Gschrey et al., *In situ* electron-beam lithography of deterministic single-quantum-dot mesa-structures using low-temperature cathodoluminescence spectroscopy. *Appl. Phys. Lett.* **102**, 251113 (2013).
- [11] B.E.A. Saleh, M.C. Teich, *Fundamentals of Photonics*, 2nd edition (2007).
- [12] E.M. Purcell, Spontaneous emission probabilities at radio frequencies. *Phys. Rev.* **69**, 681 (1946).
- [13] J.-M. Gérard et al., Enhanced spontaneous emission by quantum boxes in a monolithic optical microcavity. *Phys. Rev. Lett.* **81**, 1110–1113 (1998).
- [14] O. Gazzano et al., Bright solid-state sources of indistinguishable single photons. *Nat. Commun.* **4**, 1425 (2013).
- [15] J. Suffczynski et al., Origin of the optical emission within the cavity mode of coupled quantum dot-cavity systems. *Phys. Rev. Lett.* **103**, 027401 (2009).

- [16] M. Winger et al., Explanation of photon correlation in the far-off-resonance optical emission from a quantum-dot-cavity system. *Phys. Rev. Lett.* **103**, 207403 (2009).
- [17] D. Englund et al., *Phys. Rev. Lett.* **95**, 013904 (2005).
- [18] Y. Akahane, T. Asano, B.S. Song and S. Noda, High-Q photonic nanocavity in a two-dimensional photonic crystal. *Nature* **425**, 944–947 (2003).
- [19] T. Yoshie et al., Vacuum Rabi splitting with a single quantum dot in a photonic crystal nanocavity. *Nature* **432**, 200–203 (2004).
- [20] J. Bass, *Handbook of Optics*, 2nd edition, Vol. 2, McGraw-Hill (1994).
- [21] J. Claudon et al., A highly efficient single-photon source based on a quantum dot in a photonic nanowire. *Nat. Photon.* **4**, 174–177 (2010).
- [22] J. Bleuse et al., Inhibition, Enhancement, and Control of Spontaneous Emission in Photonic Nanowires. *Phys. Rev. Lett.* **106**, 103601 (2011).
- [23] M. Munsch et al., Dielectric GaAs Antenna Ensuring an Efficient Broadband Coupling between an InAs Quantum Dot and a Gaussian Optical Beam. *Phys. Rev. Lett.* **110**, 177402 (2013).
- [24] I. Friedler et al., Solid-state single photon sources: the nanowire antenna. *Opt. Lett.* **33**, 2635–2637 (2008).
- [25] S. Nadj-Perge, S.M. Frolov, E.P.A.M. Bakkers, and L.P. Kouwenhoven, Spin-orbit qubit in a semiconductor nanowire. *Nature* **468**, 1084–1087 (2010).
- [26] M. E. Reimer et al., Electric Field Induced Removal of the Biexciton Binding Energy in a Single Quantum Dot. *Nano Lett.* **11**, 645–650 (2011).
- [27] Y. Hu, F. Kuemmeth, C. M. Lieber, and C.M. Marcus, Hole spin relaxation in Ge–Si core–shell nanowire qubits. *Nat. Nanotech.* **7**, 47–50 (2012).
- [28] J. Wang, M. S. Gudiksen, X. Duan, Y. Cui, and C. M. Lieber, Highly polarized photoluminescence and photodetection from single indium phosphide nanowires. *Science* **293**, 1455–1457 (2001).
- [29] H. Pettersson et al., Infrared photodetectors in heterostructure nanowires. *Nano Lett.* **26**, 229–232 (2006).
- [30] M.P. van Kouwen et al., Single quantum dot nanowire photodetectors. *Appl. Phys. Lett.* **97**, 113108 (2010).
- [31] A. Tribu et al., A high-temperature single-photon source from nanowire quantum dots. *Nano Lett.* **8**, 4326–4329 (2008).

- [32] M.H.M. van Weert et al., Orientation-Dependent Optical-Polarization Properties of Single Quantum Dots in Nanowires. *Small* **5**, 2134–2138 (2009).
- [33] M.E. Reimer et al., Bright single-photon sources in bottom-up tailored nanowires *Nat. Commun.* **3**, 737 (2012).
- [34] G. Bulgarini et al., Spontaneous emission control of single quantum dots in bottom-up nanowire waveguides. *Appl. Phys. Lett.* **100**, 121106 (2012).
- [35] G. Bulgarini et al., Avalanche amplification of a single exciton in a semiconductor nanowire *Nat. Photon.* **6**, 455–458 (2012).
- [36] X. Brokmann, E. Giacobino, M. Dahan, and J.P. Hermier, Highly efficient triggered emission of single photons by colloidal CdSe/ZnS nanocrystals *Appl. Phys. Lett.* **85**, 712–714 (2004).
- [37] L. Luan, P.R. Sievert, B. Watkins, W. Mu, Z. Hong, and J.B. Ketterson, Angular radiation pattern of electric dipoles embedded in a thin film in the vicinity of a dielectric half space. *Appl. Phys. Lett.* **89**, 031119 (2006).
- [38] K.G. Lee et al., A planar dielectric antenna for directional single-photon emission and near-unity collection efficiency. *Nat. Photon.* **5**, 166–169 (2011).
- [39] X.-W. Chen, S. Götzinger, and V. Sandoghdar, 99% efficiency in collecting photons from a single emitter. *Opt. Lett.* **36**, 3545–3547 (2011).
- [40] W. Lukosz and R. E. Kunz, Light emission by magnetic and electric dipoles close to a plane dielectric interface. II. Radiation patterns of perpendicular oriented dipoles. *J. Opt. Soc. Am.* **67**, 1615–1619, (1977).
- [41] W. Lukosz and R. E. Kunz, Light emission by magnetic and electric dipoles close to a plane dielectric interface. III. Radiation patterns of dipoles with arbitrary orientation. *J. Opt. Soc. Am.* **69**, 1495–1503 (1979).

CHAPTER 4

Quantum dot emission coupled to a nanowire waveguide mode

Nanowire waveguides with controlled shape are promising for engineering the collection efficiency of quantum light sources. In this chapter we investigate the exciton lifetime in individual InAsP quantum dots, which are perfectly positioned on-axis of InP nanowire waveguides. First, control over nanowire diameter is obtained by varying wire-to-wire distance in e-beam patterned arrays. Hence, we measure the coupling efficiency of the emitter to the fundamental waveguide mode as a function of the nanowire diameter by measuring the exciton recombination rate. The spontaneous emission rate is inhibited by a factor of 12 in thin nanowires compared to nanowires with optimized waveguide diameter. From the measured inhibition factor and thus long recombination lifetime at small nanowire diameters, we determine a high radiative yield exceeding 92 %.

This chapter is based on:

G. Bulgarini, M.E. Reimer, T. Zehender, M. Hocevar, E.P.A.M. Bakkers, L.P. Kouwenhoven and V. Zwiller, *Appl. Phys. Lett.* **100** (12), 121106 (2011).

4.1 Introduction

Nanowire waveguides enable the efficient collection of single photons emitted from solid-state sources with the promise to reach efficiencies larger than 90 %. High collection efficiency has been demonstrated for self-assembled quantum dots in top-down etched nanowires [1]. One of the key parameters in designing a waveguide structure is the ratio between the nanowire diameter, D , and the emission wavelength, λ . Under optimum waveguide conditions ($D/\lambda = 0.22$ for GaAs [3] and 0.23 for InP [2] nanowires), emitted photons are funneled into the fundamental waveguide mode confined in the nanowire. As a result, the emission is very directional and can be efficiently collected with limited numerical aperture objectives [3]. In contrast, at low D/λ ratios, optical modes are no longer confined in the nanowire and the source only couples to a continuum of non-guided radiative modes yielding a non-directional emission pattern and inefficient collection of the light.

Bleuse et al. [4] demonstrated that the spontaneous emission rate Γ , defined as the inverse of the emission lifetime τ , depends strongly on the nanowire diameter. The spontaneous emission rate for diameters optimized for the waveguide approaches emission rates for the same emitter in a bulk matrix ($\Gamma = 0.9 \times \Gamma_{bulk}$ for GaAs [4]). Conversely, the spontaneous emission is suppressed at smaller nanowire diameters where the emitter weakly couples to waveguide modes in the nanowire. The spontaneous emission rate is further suppressed for randomly positioned quantum dots displaced with respect to the waveguide axis, which is thus far a common issue for self-assembled quantum dots in etched waveguides [1, 4]. Here we overcome this positioning issue by core-shell bottom-up growth of nanowire waveguides with quantum dots perfectly positioned on the waveguide axis. Our growth method enables independent control of the quantum dot location in the nanowire core and the total waveguide diameter set by the shell thickness. In this chapter we study the exciton lifetime for 50 individual quantum dots in nanowire with D/λ ranging from 0.14 to 0.30. Importantly, we are able to accurately tune the waveguide diameter by controlling the nanowire interdistance in arrays patterned on a single chip, while maintaining the same dimensions of the nanowire core where the quantum dot is positioned.

4.2 Sample preparation and characterization

InAsP quantum dots in InP nanowires are grown in a metal-organic vapor phase epitaxy reactor using the vapor-liquid-solid growth mechanism initiated with a gold catalyst. Electron-beam lithography is utilized for defining the gold catalyst size (25 and 50 nm in diameter) and positioning them in arrays [5, 6] with a nanowire interdistance ranging from 0.8 to 5 μm . Prior to growth, a two-step cleaning process including a *Piranha* etch and an in-situ anneal at 550 °C is performed in order to remove resist residues from the InP substrate [7].

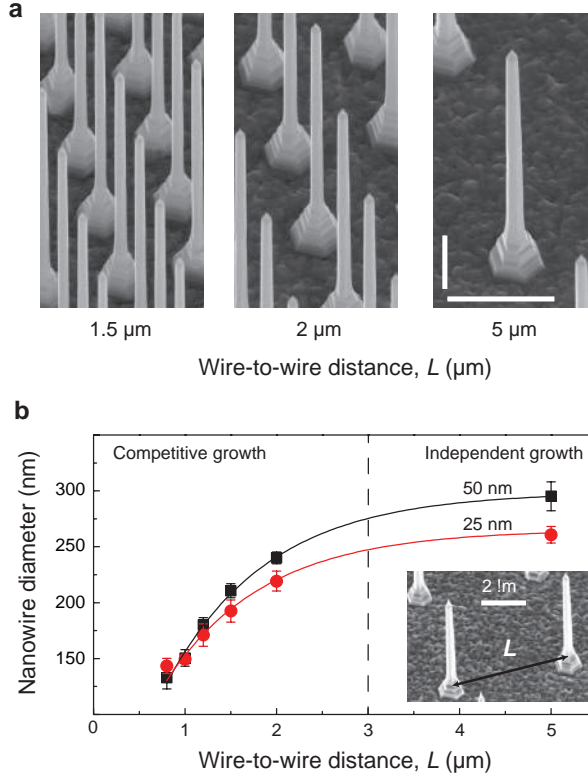


Figure 4.1: Nanowire diameter control during growth. **a**, Scanning electron micrographs of nanowires grown on the same chip using 25 nm gold catalysts and varying pitch. All images were acquired at the same magnification with the sample tilted by 30° with respect to the electron beam. Vertical and horizontal scale bars correspond to 2 μm . **b**, Dependence of the nanowire diameter on the wire-to-wire distance for 25 nm (red circles) and 50 nm (black squares) gold catalysts. Inset shows the pitch of the growth array, L . We observe an increase of the nanowire diameter as L is enlarged from 0.8 to 2 μm with a saturation at larger nanowire spacing. The dashed line indicates the transition from competitive to independent growth at $L \sim 3$ μm .

The growth is initiated with the core of the InP nanowire at 420 $^\circ\text{C}$, where an individual quantum dot is grown at half the nanowire length by adding arsenic to the system. The height of the quantum dot is defined by the growth time and is approximately 10 nm [8], whereas the quantum dot diameter is determined by the size of the gold catalyst. Subsequently to the quantum dot growth, we increase the temperature to 500 $^\circ\text{C}$ in order to enhance radial growth compared to axial growth and surround the nanowire core with a homogenous InP shell. By varying the pitch of the nanowire array for a given catalyst size, we tune the shell growth rate. The shell thickness determines the final diameter of the nanowire waveguide.

Fig. 4.1a shows scanning electron micrographs of nanowires grown from 25 nm gold catalysts in arrays of different pitches. We observe that, as the nanowire length remains constant ($\sim 7 \mu\text{m}$), the nanowire diameter enlarges by increasing the wire-to-wire distance (L). At small L , nanowires grow in the competitive growth regime and compete in the collection of indium atoms diffusing on the substrate surface [9]. By increasing L , the collection area for each nanowire enlarges, resulting in an enhancement of the volume collected per nanowire owed by mass conservation as it has been previously reported for InAs [9] and GaP [10] nanowires. Finally, when the distance between nanowires exceeds the diffusion length of indium atoms, the growth rate becomes independent on the nanowire spacing and saturates. In our work, we exploit these two growth regimes to accurately control the nanowire waveguide diameter. In Fig. 4.1b, we measure the average nanowire diameter at the quantum dot position for each growth array. We observe the transition from the competitive to independent growth regime at $L \sim 3 \mu\text{m}$.

Photoluminescence (PL) spectroscopy is utilized to study the spontaneous emission properties of single InAsP quantum dots in InP nanowire waveguides. Fig. 4.2a shows typical PL spectra of a single quantum dot as a function of the excitation power at 10 K, using a continuous-wave Ti:Sapphire laser at $\lambda = 750 \text{ nm}$ and spot size of $\sim 1 \mu\text{m}$. We observe two emission peaks due to the exciton (X) recombination at 979.1 nm and the biexciton (XX) recombination at 979.6 nm, respectively. Fig. 4.2b shows the integrated emission intensity measured on a silicon CCD for the X and XX peak, respectively, as a function of the excitation power. Experimental data are fit with Poisson statistics using a linear and quadratic coefficient for X and XX, respectively, in order to accurately label the peaks. A PL spectrum at low excitation power is shown in Fig. 4.2c. The exciton emission linewidth is 120 μeV and is separated from the biexciton emission by 0.65 meV. The spectrum is representative of the quantum dots investigated in this work that exhibit a rather narrow distribution of exciton emission wavelength: $975 \pm 5 \text{ nm}$.

4.3 Time-resolved photoluminescence

In the following, we filter the exciton peak in order to measure the exciton lifetime through time-resolved photoluminescence. Fig. 4.3a shows five photoluminescence decays measured on single quantum dots positioned in nanowires with different diameters, corresponding to different D/λ ratios. The quantum dot is now excited with 3 ps laser pulses using a repetition rate of 76 MHz and time-resolved PL is measured with a silicon avalanche photodiode. The background associated with the dark counts of the detector is subtracted from the measurements. The PL intensity (circles) is normalized to 1 for each measurement and the PL decays are fitted with mono-exponential decays displayed by blue lines. The exciton lifetime is significantly shortened by increasing D/λ from 0.14 to 0.24, since the quantum dot couples with increasing efficiency to the fundamental waveguide mode in the nanowire.

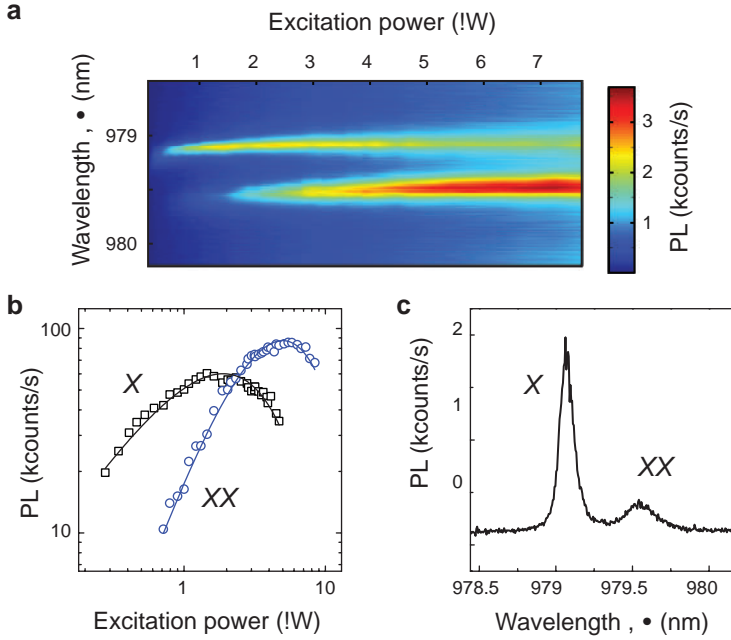


Figure 4.2: Single quantum dot optical characterization. **a**, Power dependent photoluminescence (PL) spectroscopy of a single InAsP quantum dot in an InP nanowire. The intensity of PL emission is displayed as color. **b**, Integrated PL intensity for exciton (X, black squares) and biexciton (XX, blue circles) emission peaks, fitted with Poisson statistics using linear and quadratic coefficients, respectively. **c**, PL spectrum at low excitation power (0.8 μW). The exciton emission exhibits a linewidth (FWHM) of 120 μeV.

In Fig. 4.3b, we plot the exciton lifetime for all investigated quantum dots with D/λ ratios ranging from 0.14 to 0.30. Each experimental data point refers to the exciton lifetime of a single quantum dot and the corresponding D/λ ratio is calculated from the exciton emission wavelength. At small D/λ (0.14-0.15), the quantum dot only couples to a continuum of non-guided radiative modes propagating away from the nanowire axis with a long recombination lifetime ($\tau > 15$ ns). As the nanowire diameter is increased, and accordingly the D/λ ratio, the quantum dot emission mode couples to the fundamental waveguide mode with an increased rate. [3]. Thus, the coupling of the quantum dot to this waveguide mode results in a remarkable shortening of the exciton lifetime until saturation occurs for D/λ ranging between 0.24 and 0.30. At saturation, the exciton lifetime approaches 1.7 ns as predicted for InAs quantum dots buried in a bulk InP matrix [11] (displayed by the red dash-dotted line). The observed behavior is consistent with calculations that assume an in-plane radiative dipole for the quantum dot [3], which are experimentally confirmed in Ref. [4]. Hence, we conclude that the dipole associated with the exciton transition is oriented perpendicular to the waveguide

axis for quantum dots in bottom-up grown nanowires studied in this work. From the dipole orientation, combined with the quantum dot position on the nanowire axis [2], a coupling efficiency to the fundamental waveguide mode above 95 % is expected from fully vectorial calculations under optimum photonic confinement [4]. By comparing the exciton lifetime measured for $D/\lambda \sim 0.245$ (dotted circle, $\tau = 2.0 \pm 0.2$ ns) with that measured for $D/\lambda \sim 0.14$ (black circle, $\tau = 24.0 \pm 0.4$ ns), we obtain an inhibition factor of 12 for thinner nanowires. This inhibition of the spontaneous emission rate is solely due to suppression of the coupling to the fundamental waveguide mode [3]. Similar results have been demonstrated by using the bandgap of 2D photonic crystals [12, 13], 3D photonic crystals [14, 15] or with photonic nanowires [4]. In stark contrast to top-down etched photonic nanowires, the quantum dot emission in bottom-up grown nanowires is still clearly visible for diameters as small as 50-60 nm [8]. In the case of GaAs photonic nanowires with $D < 120$ nm [4] the quantum dot emission is totally suppressed, most likely due to the fast surface recombination velocity in GaAs [16] that could be further enhanced by etching-related defects.

4.4 Conclusions

The measurements of the recombination lifetime of excitons in nanowire waveguides enables us to estimate the radiative quantum efficiency of InAsP quantum dots in bottom-up grown nanowires. The long exciton lifetime that we measure in thin nanowires (i.e., $\tau = 24$ ns for $D/\lambda \sim 0.14$) is suggestive of the high optical quality for quantum dots investigated in this work since non-radiative recombination processes act on time scales longer than 24 ns ($\Gamma = 1/\tau = 42 \mu\text{s}^{-1}$). The total recombination rate, Γ , is composed of both radiative, Γ_R , and non-radiative, Γ_{NR} , decay channels:

$$\Gamma = \Gamma_R + \Gamma_{NR}, \quad (4.1)$$

the slow recombination rate that we measure for thin nanowires sets the highest limit of $\Gamma_{NR} = 42 \mu\text{s}^{-1}$. In reality, however, Γ_{NR} is lower since part of the measured recombination rate is originating from light emission. In order to calculate the radiative quantum efficiency, $\eta = \Gamma_R/\Gamma$, we analyze the recombination rate when the quantum dot couples to the fundamental waveguide mode of the nanowire and we assume that the non-radiative recombination rate, Γ_{NR} , is constant as a function of nanowire diameter. At $D/\lambda \sim 0.245$, the average measured lifetime is $\tau = 2$ ns, corresponding to a recombination rate of $\Gamma = 500 \mu\text{s}^{-1}$. Thus, using $\Gamma_{NR}^{max} = 42 \mu\text{s}^{-1}$ we infer from equation 4.1 that $\Gamma_R = 458 \mu\text{s}^{-1}$. As a result, we obtain a high radiative quantum efficiency, $\eta = 92$ %, which is the first experimental measurement for the efficiency of InAsP quantum dots in bottom-up grown nanowires and should be considered as a lower bound of the actual radiative quantum efficiency.

In conclusion, we have investigated the exciton spontaneous emission lifetime for single InAsP quantum dots positioned on the axis of InP nanowire waveguides. The

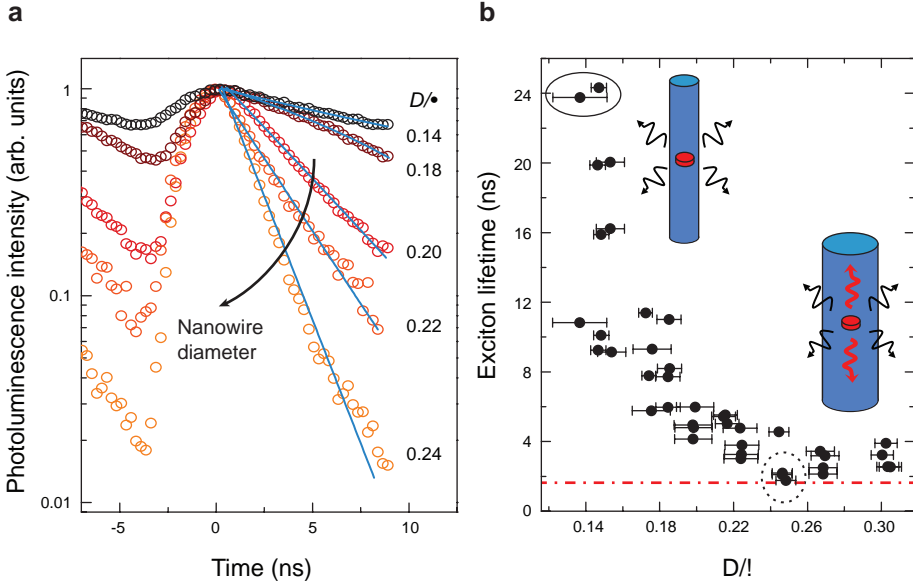


Figure 4.3: Exciton lifetime as a function of the nanowire diameter. **a**, Time-resolved photoluminescence on five different excitons in quantum dots embedded in nanowires with different diameters. The photoluminescence intensity (circles) is shown in a logarithmic scale and each curve is fitted with a mono-exponential decay (blue lines). The result is a significant shortening of the exciton lifetime. **b**, Each experimental point represents the exciton lifetime measured for a single quantum dot. The shortest exciton lifetime (dotted circle) approaches the lifetime predicted for the same material system in bulk (red dash-dotted line). Error bars are provided for D/λ ratio due to the variation of nanowire diameter measured within the same growth pattern.

bottom-up approach employed for the growth of nanowires enables us to analyze a wide range of diameters on the same chip. The e-beam positioning of gold catalysts allows for an accurate control of nanowire diameter during growth and for obtaining high uniformity within the same growth array. We have demonstrated that the spontaneous emission rate is maximum for $D/\lambda \sim 0.245$ when the quantum dot efficiently couples to the fundamental waveguide mode and the emission is well confined in the nanowire. At smaller nanowire diameters, we observe an inhibition of the spontaneous emission by a factor of 12, from which we obtain a radiative quantum efficiency exceeding 92 % for quantum dots in bottom-up grown nanowires.

4.5 References

- [1] J. Claudon et al., A highly efficient single-photon source based on a quantum dot in a photonic nanowire. *Nat. Photon.* **4**, 174–177 (2010).
- [2] M.E. Reimer et al., Bright single-photon sources in bottom-up tailored nanowires. *Nat. Commun.* **3**, 737 (2012).
- [3] I. Friedler et al., Solid-state single photon sources: the nanowire antenna. *Opt. Express* **17**, 2095–2110 (2009).
- [4] J. Bleuse et al., Inhibition, Enhancement, and Control of Spontaneous Emission in Photonic Nanowires. *Phys. Rev. Lett.* **106**, 103601 (2011).
- [5] J. Heinrich et al., Single photon emission from positioned GaAs/AlGaAs photonic nanowires. *Appl. Phys. Lett.* **96**, 211117 (2010).
- [6] D. Dalacu et al., Selective-area vapor-liquid-solid growth of tunable InAsP quantum dots in nanowires. *Appl. Phys. Lett.* **98**, 251101 (2011).
- [7] A. Pierret et al., Generic nano-imprint process for fabrication of nanowire arrays. *Nanotechnology* **21**, 065305 (2010).
- [8] M.H.M. van Weert et al., Selective excitation and detection of spin states in a single nanowire quantum dot. *Nano Lett.* **9**, 1989–1993 (2009).
- [9] L.E. Jensen et al., Role of surface diffusion in chemical beam epitaxy of InAs nanowires. *Nano Lett.* **4**, 1961–1964 (2004).
- [10] M. T. Borgstrom, G. Immink, B. Ketelaars, R. Algra, and E. P. A. M. Bakkers, Synergetic nanowire growth. *Nat. Nanotech.* **2**, 541–544 (2007).
- [11] M. Gong, W. Zhang, G. C. Guo, and L. He, Atomistic pseudopotential theory of optical properties of exciton complexes in InAs/InP quantum dots. *Appl. Phys. Lett.* **99**, 231106 (2011).
- [12] M. Fujita, S. Takahashi, Y. Tanaka, T. Asano, and S. Noda, Simultaneous inhibition and redistribution of spontaneous light emission in photonic crystals. *Science* **308**, 1296–1298 (2005).
- [13] W.-H. Chang et al., W.-Y. Chen, H.-S. Chang, T.-P. Hsieh, J.-I. Chyi, and T.-M. Hsu, Efficient single-photon sources based on low-density quantum dots in photonic-crystal nanocavities. *Phys. Rev. Lett.* **96**, 117401 (2006).
- [14] P. Lodahl et al., Controlling the dynamics of spontaneous emission from quantum dots by photonic crystals. *Nature* **430**, 654–657 (2004).

-
- [15] M.D. Leistikow et al., Inhibited spontaneous emission of quantum dots observed in a 3D photonic band gap. *Phys. Rev. Lett.* **107**, 193903 (2011).
 - [16] H. Joyce et al., Ultralow Surface Recombination Velocity in InP Nanowires Probed by Terahertz Spectroscopy *Nano Lett.* **12**, 5325–5330 (2012).

CHAPTER 5

Bright single-photon sources in bottom-up tailored nanowire waveguides

The ability to achieve near-unity light extraction efficiency is necessary for a truly deterministic single-photon source. The most promising method to reach such high efficiencies is based on single-photon emitters embedded in tapered photonic waveguides. In this chapter, we demonstrate a 24-fold enhancement in the single-photon flux that we measured using tapered nanowire waveguides compared to quantum dots in thin nanowires. We further compare top-down fabrication techniques to the bottom-up growth approach that we employ. Currently, light extraction efficiencies top-down approaches are limited by fabrication imperfections and etching induced defects. The efficiency is further tempered by randomly positioned off-axis quantum emitters. Utilizing bottom-up growth, instead, only a single quantum dot is grown per nanowire and it is always positioned on the waveguide axis.

This chapter is based on:

M.E. Reimer, G. Bulgarini, N. Akopian, M. Hocevar, M. Bouwes Bavinck, M. A. Verheijen, E.P.A.M. Bakkers, L.P. Kouwenhoven and V. Zwiller, *Nat. Commun.* **3**, 737 (2012).

5.1 Introduction

A deterministic single-photon source with unity extraction efficiency would revolutionize the fields of quantum computation [1], quantum cryptography [2] and quantum optics [3]. Recently, significant progress has been made toward achieving high efficiency single-photon sources [4, 5, 6, 7, 8, 9, 10]. Amongst these sources, semiconductor quantum dots show particular promise since they can be embedded in devices enabling electrical injection, while maintaining efficient light emission [11, 12]. The most frequent approach to enhance the light extraction efficiency η of a single-photon source, defined as the fraction of photons collected by the first lens, is to embed the quantum dots in microcavities and utilize the Purcell effect when the exciton emission is resonant with a cavity mode. However, to reach a high efficiency, a high quality factor and low mode volume are required, which therefore limits the bandwidth to a fraction of a nanometer in wavelength [3]. Moreover, η is further limited due to losses such as fabrication imperfections or absorption losses in the cavity [13].

A more recent approach that overcomes the narrow bandwidth limitation of microcavities and thus allows for broadband spontaneous emission control is based on tapered photonic waveguides [6]. In that work, the tapered photonic waveguides were achieved by etching a GaAs wafer containing InAs quantum dots with random position. The light extraction efficiency was increased by optimizing the photonic waveguide diameter to maximize the amount of light emitted from the quantum dot into the fundamental mode of the waveguide as compared to higher-order modes, and by tapering the waveguide tip to minimize total internal reflection at the semiconductor-air interface [6]. Such reflections were avoided due to a smooth reduction in the effective refractive index towards the nanowire tip and adiabatic expansion of the fundamental mode during propagation. An additional advantage of the nanowire taper is the good directionality of photon emission from the nanowire, which allows for efficient collection by a commercial objective [6]. However, due to the random positions of the quantum dots, there are multiple dots in each individual etched waveguide. Consequently, the quantum dots are not likely to be found exactly on the waveguide axis, which diminishes the coupling of the emitter to the fundamental waveguide mode, thus drastically reducing the overall light extraction efficiency [14].

In this work, we increase the light extraction efficiency of a quantum dot emitter in a tailored nanowire waveguide using a bottom-up growth approach through independent control of both the nanowire shape and quantum dot location. Under the appropriate growth conditions, we have positioned a single InAsP quantum dot exactly on the axis of an InP nanowire waveguide with a very small tapering angle towards the tip ($\alpha = 2^\circ$). Our bottom-up approach has the potential to reach near-unity light extraction efficiency ($\eta = 97\%$), assuming a perfect mirror below the nanowire, a 1° nanowire taper and high coupling of the quantum emitter into the fundamental waveguide mode compared to higher order modes (i.e., β -factor of 0.95) for a quantum dot emitter on-axis of the nanowire waveguide [15]. Single, on-axis quantum emitters and reduced tapering angles

are possible with our nanowire tailoring bottom-up growth technique and out of reach of current top-down etching techniques [16, 6].

5.2 Fabrication of a tapered nanowire waveguide

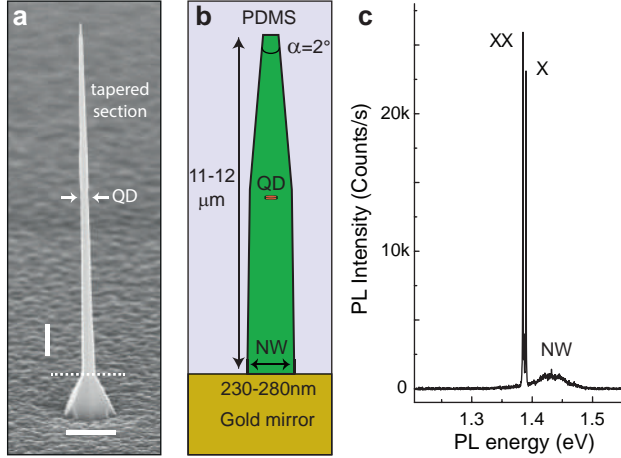


Figure 5.1: Tailored nanowire waveguide geometry. **a**, SEM image of tapered InP nanowire waveguide containing a single InAsP quantum dot (QD). The tapering angle of the nanowire is $\alpha = 2^\circ$. The nanowire breaks at the dotted line after transfer into PDMS. Vertical and horizontal scale bar: 1 μm . **b**, Tailored nanowire geometry embedded in PDMS with bottom gold mirror. The quantum dot (QD) is indicated by the red dot and, by design, is positioned on the nanowire waveguide axis where the emission is efficiently coupled to the fundamental waveguide mode. **c**, Typical single dot PL of exciton (X) and biexciton (XX) in an individual nanowire, exhibiting a clean optical spectrum over a large energy range. The broad peak at 1.43 eV originates from the InP nanowire (NW).

Fig. 5.1a shows an SEM image of our tailored nanowire waveguide with nanowire diameter of 200 nm, length of 11.2 μm and 2° taper at the tip. Each individual nanowire contains, by design, a single quantum dot exactly on the nanowire axis. To achieve such a high level of control, we first grow the nanowire core, which consists of a thin segment of InAsP (quantum dot) embedded in an InP nanowire. At this stage, the nanowire and quantum dot have a diameter that is approximately equal to the size of the gold particle (~ 20 nm) used as a catalyst in the vapour-liquid-solid growth mechanism. After growth of the quantum dot and nanowire, the temperature is increased in order to suppress axial growth and favor shell growth. The final result is a waveguide section at the quantum dot position and a very small nanowire taper towards the tip. These two effects combined together are used to efficiently extract the light of our single-photon emitter.

Since single photons emitted by the quantum dot can travel both directions in the nanowire waveguide, losses can be reduced by adding a metallic mirror at the nanowire

base to reflect downward emitted photons. As our growth technique does not allow for growth of nanowires on top of a metallic mirror, we have integrated a gold mirror at the nanowire base by transferring them into a flexible and fully transparent polydimethylsiloxane (PDMS) polymer film as sketched in Fig. 5.1b. The first section of the nanowire before quantum dot growth exhibits a small tapering angle of 0.4° , whereas the second section of the nanowire after quantum dot growth features a tapering angle of $\alpha = 1.5^\circ \pm 0.2^\circ$. From SEM analysis of the as-grown nanowire sample, the nanowire diameter that surrounds the quantum dot was determined to be 160–220 nm. We conclude from finite-difference time-domain (FDTD) simulations of InP nanowires, to be presented later, that the most efficient coupling of quantum dot emission into the fundamental mode in the nanowire waveguide for emission wavelength, λ of 950 nm occurs for a nanowire diameter, D of 220 nm (i.e., $D/\lambda = 0.23$).

A photoluminescence (PL) spectrum from a single InAsP quantum dot in an InP tapered nanowire is presented in Fig. 5.1c. Such behavior illustrates a significant advantage of quantum dots in nanowires [17, 18, 19, 20] as compared to randomly grown quantum dots by the self-assembly growth process [4, 5, 6]. Since the nanowire contains only a single quantum dot by nature of the bottom-up growth process, the observed PL spectrum exhibits only emission from a single quantum dot over a large energy range, originating from exciton and biexciton recombination. The broad emission peak at higher energy originates from the InP nanowire. Most important is the natural location of the quantum dot on the nanowire axis, which therefore couples to the optical field of a waveguide more efficiently than randomly positioned quantum dots [6, 14].

5.3 Quantum dot location and composition

We verify that the quantum dot is exactly positioned on the nanowire waveguide axis by high resolution scanning transmission electron microscopy (STEM) images, as well as analysis of the chemical composition, presented in Fig. 5.2(a-c). As it is very difficult to image the quantum dot when surrounded by a thick shell of approximately 200 nm, a nanowire sample with a thinner shell of approximately 100 nm is measured. The STEM image in Fig. 5.2a is used to exhibit the thickness of the core and shell. Fig. 5.2b shows the same STEM image as in Fig. 5.2a, but now using contrast/brightness settings optimized for visibility of the quantum dot. The quantum dot is of the pure wurtzite structure without stacking faults. From the resulting image, a quantum dot height of 7 ± 1 nm and diameter of 20 nm is obtained.

Confirmation of the quantum dot location is established by performing an energy-dispersive X-ray (EDX) spectroscopy line scan along the nanowire growth axis, indicated by the arrow in Fig. 5.2b. The results of the EDX line scan are shown in Fig. 5.2c, which shows an increase in the As concentration at the location of the quantum dot we infer from Fig. 5.2b. By subtracting the contribution of the shell around the quantum dot, we conclude that the As concentration of the quantum dot is 12.5 atomic %, corresponding

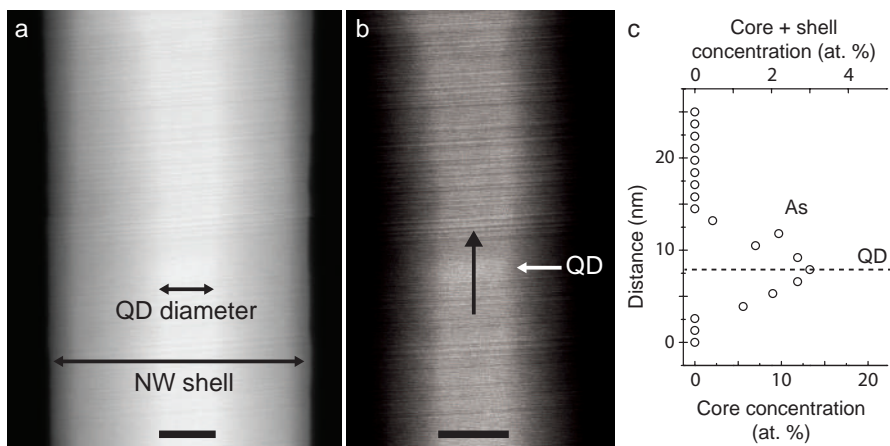


Figure 5.2: Single quantum dot on the nanowire waveguide axis. High angle annular dark field (HAADF) scanning transmission electron microscopy images confirming that the quantum dot is perfectly positioned on the nanowire waveguide axis. Optimized contrast settings for visibility of nanowire (NW) core and shell in **a** and quantum dot in **b**. The quantum dot is recognized along the black arrow in **b** by the contrast change from dark to bright regions along the nanowire. Scale bar: 20 nm. **c**, Energy-dispersive X-ray spectroscopy line scan along the arrow in **b** confirming the presence of the quantum dot. The As concentration reaches a maximum of 12.5 % in the core only, thus resulting in a chemical composition for the quantum dot of $\text{InAs}_{0.25}\text{P}_{0.75}$.

to a chemical composition of $\text{InAs}_{0.25}\text{P}_{0.75}$. The As concentration of the quantum dot is confirmed by independent measurements based on the resulting intensities obtained from the high angle annular dark field (HAADF) STEM images presented in Fig. 5.2. At the position of the quantum dot, the brightness after background subtraction is 2.8 % higher. Since the HAADF intensity scales with tZ , where t is the local sample thickness and Z is the atomic number, thus, the composition is determined. The total brightness consists of both the core and shell contributions. Using the HAADF intensity, $I = tZ_{\text{average}}^{1.7}$, where $Z_{\text{average}} = \{Z_{\text{In}} + xZ_{\text{As}} + (1 - x)Z_{\text{P}}\}/3$, we find that $x = 0.26 \pm 0.06$, which is in excellent agreement with the quantum dot composition of $\text{InAs}_{0.25}\text{P}_{0.75}$ obtained from the EDX results.

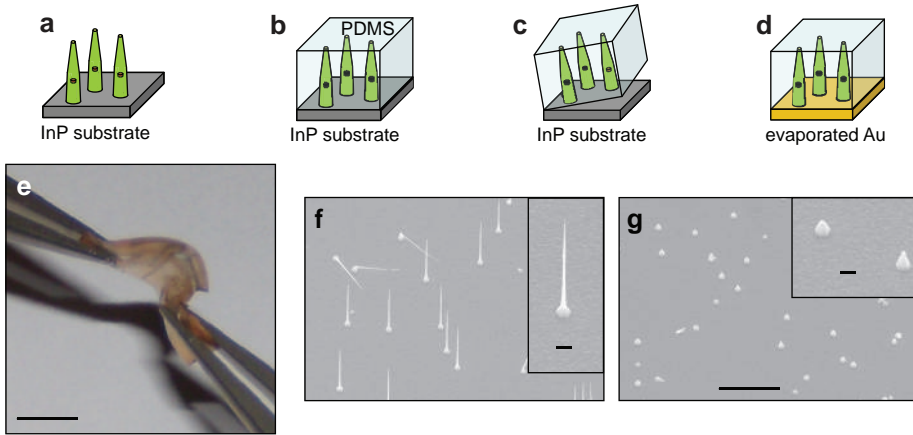


Figure 5.3: PDMS nanowire transfer method for integration of bottom gold mirror. **a**, Growth of single InAsP quantum dots embedded in InP nanowires on an InP substrate. **b**, PDMS is spin-coated and subsequently cured to obtain a thin layer ($\sim 10\ \mu\text{m}$) comparable to the nanowire length. **c**, Embedded nanowires in PDMS are removed from the InP substrate using tweezers and a razor blade to scrape the substrate surface. **d** An 80 nm gold layer is evaporated at the nanowire base. The red dots in **a-d** indicate the quantum dots in individual nanowires. **e**, Optical image of finished flexible device containing very bright single-photon emitters, which are held between two tweezers. **f,g**, SEM images of the as-grown sample before **f** and after **g** nanowire transfer. Since there are no nanowires remaining in **g**, we conclude that 100% of nanowires are successfully transferred into PDMS. Scale bar: $10\ \mu\text{m}$. The insets of **f** and **g** show a magnified view of their respective image with scale bar of $1\ \mu\text{m}$.

5.4 Sample preparation

A gold mirror is integrated at the nanowire base by transferring the nanowires into polydimethylsiloxane (PDMS), followed by metal evaporation as displayed in Fig. 5.3**a-e**. The preparation of the PDMS solution consists of mixing a polymer base and a curing agent with a weight ratio of 10:1. The polymer used is Sylgard 184 PDMS elastomer kit from Dow Corning. The uncured polymer was diluted with methylene chloride (0.5 g/ml) in order to decrease the viscosity of the polymer and enable the realization of thin films by spin coating the polymer solution on the nanowire substrate [28]. Using a spin coating speed of 6000 rpm for 1 minute, we obtain a PDMS layer with thickness comparable to the nanowire length, $10\ \mu\text{m}$. After depositing the PDMS film, a waiting time of 15 hours was used to allow the polymer to set. This process improved the peeling of the polymer film containing the nanowires after curing at 125°C for 20 minutes. An SEM image of the as-grown sample is shown before (Fig. 5.3**f**) and after (Fig. 5.3**g**) the nanowire transfer process. Since only the thick nanowire bases are left in Fig. 5.3**g**, we conclude that 100 % of nanowires are transferred successfully into PDMS. The wires in Fig. 5.3**f** that appear to be lying on the substrate are a small fraction of wires that

are kinked and continue to grow along other crystallographic directions instead of the normal (111).

5.5 Single-photon extraction efficiency

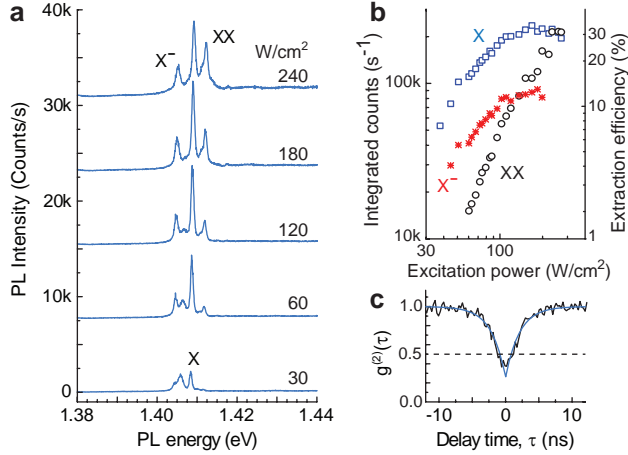


Figure 5.4: Bright single-photon emission of tailored nanowire waveguides. **a**, Typical power dependence of single quantum dot in tailored nanowire waveguide under pulsed laser excitation. The PL spectra are offset for clarity. **b**, Integrated counts of exciton (X), biexciton (XX), and charged exciton (X^-) from **a** as a function of increasing excitation power. Remarkably, the X line saturates at values as high as 236,000 counts per second measured on the CCD detector, resulting in a photon collection efficiency of $\sim 30\%$. Accounting for competition between recombination of X^- and X, we estimate an η for the nanowire waveguide of 42%. We note that the calculated collection efficiencies are only valid at quantum dot saturation where the generation efficiency is maximum. **c**, Second order correlation function, $g^{(2)}(\tau)$, of single X line. The anti-bunching dip below 0.5 is characteristic of a single-photon emitter. Accounting for the finite time response of our single-photon detectors, we obtain $g^{(2)}(0)$ of 0.12 and X lifetime of $1.7\text{ ns} \pm 0.1\text{ ns}$.

We characterize the collection efficiency enhancement of our single-photon emitter through PL studies under pulsed laser excitation at a repetition rate of 76 MHz. Pulsed excitation provides a good estimate of the extraction efficiency since it is expected that the quantum dot returns to the ground state and cannot emit until the next excitation pulse. Power dependent PL spectra for a single quantum dot after transfer into PDMS and integration of the bottom gold mirror are shown in Fig. 5.4a. At low excitation power, the main PL peak observed at 1.409 eV is attributed to the neutral exciton (X) involving electron-hole recombination in the quantum dot s-shell. Further increase of the excitation power results in biexciton (XX) emission, 3 meV above the exciton line. In our nanowire samples, the biexciton emission can appear either above [18] or below

[21, 22] depending on the dot height. Both exciton and biexciton are identified by the observed linear and quadratic power dependence, respectively, as shown in Fig. 5.4b. The identification of exciton and biexciton was further verified in other quantum dots on the same sample that exhibit a fine-structure splitting. Exciton fine-structure splittings up to 30 μeV are observed for in InAsP quantum dots in nanowires [18]. The singly charged exciton, X^- , is 4 meV below the exciton line and was determined from the observed linear power dependence in Fig. 5.4b and electric field measurements of dots in nanowires studied in earlier work [21, 22].

The brightness of our single-photon source is presented in Fig. 5.4b, which shows the integrated count rate from Fig. 5.4a as a function of excitation power. At saturation, the integrated count rate of the single exciton line measured on the CCD detector is 236,000 counts per second. The measured count rate is a factor of 24 times brighter than previously reported on InAsP quantum dots in InP nanowires [18]. Taking into account the measured collection efficiency of our experimental setup ($\sim 1\%$), a single-photon flux at the first lens of 24 MHz is estimated. This estimation results in a light extraction efficiency, η of our single-photon emitter of $\sim 30\%$, corresponding to 0.3 photons per pulse arriving at the first lens. We note that since there is a competition between the charged exciton and neutral exciton states in the observed PL emission spectra, we in fact underestimate the efficiency of the nanowire waveguide. From the integrated intensity at saturation (Fig. 5.4b), we estimate that approximately one-quarter of the time an electron is captured into the quantum dot resulting in recombination of the charged exciton instead of the neutral exciton. Taking into account the competition between recombination of charged exciton and neutral exciton states, our estimated collection efficiency of the nanowire waveguide is 42%. The deviation from the expected 71% when assuming a 2° nanowire taper may be due to several factors such as the quality of the gold mirror, internal quantum efficiency of the quantum dot, and unwanted reflections at the PDMS-air interface. The main source of discrepancy between the theoretical and measured η is due to the quality of the gold mirror. If we assume a modal reflectivity for the guided mode on the mirror of 30% with $D/\lambda = 0.22$ according to calculations by Friedler et al. [23], and 4% total internal reflection losses at the PDMS-air interface, the expected η matches the measured 42% for a quantum dot internal quantum efficiency of 95%. In order to approach the theoretical η of 71%, the modal reflectivity of the guided mode on the mirror may be improved by adding a thin dielectric between the mirror and semiconductor nanowire as suggested by Friedler et al. [23], while losses at the PDMS-air interface can be diminished by using silica aerogel with an index of refraction close to 1.

In Fig. 5.4c, we demonstrate single-photon emission by filtering the single X line close to saturation and perform photon correlation measurements in a standard Hanbury-Brown and Twiss setup. The second order correlation function $g^{(2)}(\tau)$ indicates strong multi-photon suppression evident by the absence of coincidence counts at zero time delay and is a signature of single-photon emission. We measure $g^{(2)}(0)$ of 0.36. Taking into account the finite time response of the Si avalanche photodiodes, we obtain $g^{(2)}(0)$ of

0.12. The remaining contribution to $g^{(2)}(0)$ is due to background photons that originates from the tail of the InP nanowire emission. We have thus subtracted this background emission from our measured photon fluxes to estimate the collection efficiencies.

5.6 Modeling of the fundamental waveguide mode

Finite-difference time-domain (FDTD) simulations were performed using a nanowire waveguide geometry similar to the experimentally investigated nanowires in order to quantify the light intensity enhancement due to the bottom gold mirror, which replaces the InP substrate after the nanowire transfer process.

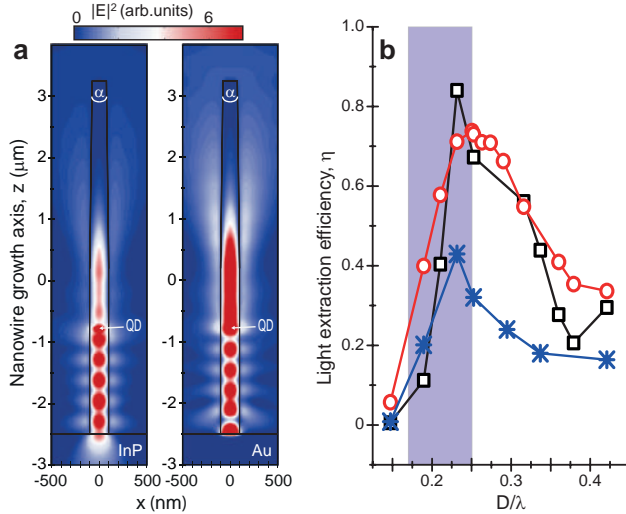


Figure 5.5: Calculated light extraction efficiency from single quantum dot in tailored nanowire waveguides. **a**, Finite-difference time-domain simulations showing the intensity profile for a 2D-cut along the nanowire growth axis. The integrated intensity at the nanowire end is a factor of 2.7 larger on the gold (Au) substrate (right) as compared to the InP substrate (left). The nanowire dimensions are similar to the experimentally investigated nanowires using a tapered nanowire geometry with full-angle of $\alpha = 2^\circ$ and nanowire diameter of 200 nm. An in-plane electric dipole emitter is used to represent the quantum dot (QD). **b**, Calculated light extraction efficiency, η , at nanowire end using an NA of 1 for tapered nanowire surrounded by air (black squares) or embedded in PDMS (red circles), both on top of a gold substrate. The absence of the nanowire taper (blue stars) reduces the maximum η through reflections at the nanowire top. The shaded region indicates the range of D/λ used in the present experiments.

The results of these calculations, excluding PDMS, are shown in Fig. 5.5a for a nanowire on an InP and gold substrate. In both cases, the intensity profile is plotted for a two-dimensional cut along the nanowire growth axis for an in-plane electric dipole emitter, which is used to represent a flat quantum dot in III-V nanowires [24]. In each

case, a standing wave of the fundamental mode HE_{11} is observed between the emitter and substrate for a nanowire diameter of 200 nm and emission wavelength λ of 950 nm. The emitter location has been optimized by positioning it at one of the antinodes of the electric field. It is very important that the reflected light from the downward emitted photons is in-phase at the emitter position so that they interfere constructively. The light intensity at the nanowire end is determined from the simulations for a numerical aperture of 1 and increases by a factor of 2.7 with the addition of a gold substrate as compared to InP only. The increase in light emission at the nanowire end with gold substrate is evident in Fig. 5.5a. Including PDMS in Fig. 5.5b, the light enhancement of 2.7 is reduced to 2.4 as the effective index of refraction surrounding the electric dipole is modified. The deviation from the intuitive factor of 2 is because the presence of the gold mirror modifies the electromagnetic environment of the quantum emitter. As a result, the single-photon flux is increased due to a shortening of the quantum dot exciton radiative lifetime for a quantum dot positioned at the electric field anti-node [14]. In the following, we optimize the calculated light extraction efficiency, η , at the nanowire end for a numerical aperture (NA) of 1 by modifying the nanowire diameter with (red circles) and without (black squares) PDMS on top of a gold substrate (Fig. 5.5b). The optimum η only shifts from D/λ of 0.23 without PDMS to D/λ of 0.25 with addition of PDMS as the effective refractive index of PDMS ($n=1.5$) is slightly larger than air. These D/λ values are within the range of nanowires investigated in this work, indicated by the shaded region in Fig. 5.5b. For comparison, we also show η without nanowire tapering in air (blue stars). The effect of the tapered nanowire tip results in a ~ 2 -fold enhancement in the maximum η as compared to no nanowire taper. By varying the NA in the FDTD simulations from 1 to 0.75 (NA of our objective in experiment), there is only a reduction of $\sim 3\%$ in the calculated η due to the good directionality of photon emission from the nanowire taper.

5.7 Extraction efficiency enhancement

In Fig. 5.6, we demonstrate an enhancement of the single quantum dot PL intensity with our tailored nanowires in comparison to non-tailored nanowires. The comparison is made for our brightest quantum dot obtained for three different nanowire geometries: no waveguide (Fig. 5.6a); tapered nanowire waveguide (Fig. 5.6b); and tapered nanowire waveguide with gold mirror and PDMS (Fig. 5.6c). The single exciton (X) integrated PL intensity exhibits a clear enhancement with optimum tapered nanowire waveguide and further increase with integration of gold mirror in comparison to no waveguide. The main factors that influence the observed enhancement are nanowire diameter and quantum dot position along the nanowire growth axis. When these conditions are fulfilled, single-photon emission flux obtained by the integrated peak area is enhanced 20-fold with tapered nanowire waveguide and gold mirror (Fig. 5.6c) as compared to no waveguide (Fig. 5.6a). Since we cannot measure the exact same quantum dot for all three cases,

a statistical distribution of integrated PL intensity for the single exciton (X) line at saturation for ten quantum dots is shown in Fig. 5.6d. A clear trend is observed in the distribution of integrated PL intensity. The implementation of the gold mirror at the bottom of nanowire waveguides yields an average enhancement of 2.4 in the detected photon flux, which is in agreement with the theoretical predictions from Fig. 5.5.

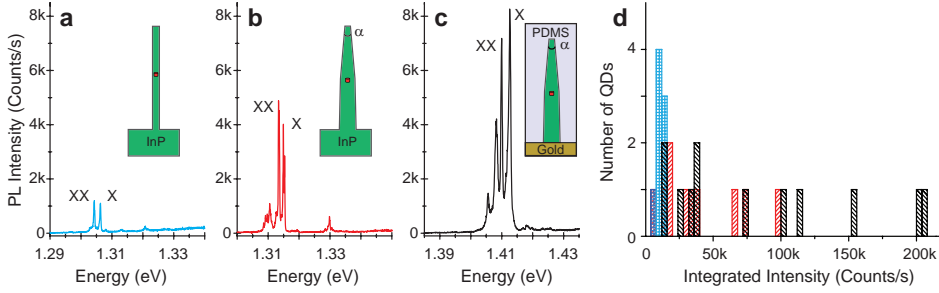


Figure 5.6: Enhanced single quantum dot emission. Comparison of PL intensity for the brightest quantum dots obtained utilizing three different nanowire geometries: **a**, no waveguide; **b**, tapered nanowire waveguide; and **c**, tapered nanowire waveguide + gold + PDMS. The integrated PL intensity of the exciton (X) increases by a factor of up to 20 with the tapered nanowire waveguide and bottom gold mirror in **c** as compared to no waveguide in **a**. Note that **a-c** shows the emission of different quantum dots which are representative for the respective case. The inset depicts schematically the nanowire geometry. XX: biexciton. **d**, Histogram of integrated PL intensity of single exciton (X) peak at saturation. The y-axis represents the number of quantum dots with measured PL intensity for a bin size of 4,000 counts/s. The dispersion of data originates from the variable distance of the quantum dot to the mirror. Blue: no waveguide; red: tapered nanowire waveguide; black: tapered nanowire waveguide + gold + PDMS. We observe an average enhancement of 2.4 with tapered nanowire waveguide and gold mirror in comparison to no mirror, which is in good agreement with our simulations.

5.8 Conclusions

The 20-fold enhancement in single-photon emission that we observe for individual quantum dots in tailored nanowire geometries using a bottom-up growth approach compared to non-tailored nanowire geometries makes future experiments in the combination of both transport and optics more realistic. As an example, a single quantum dot embedded in a nanowire waveguide can be coupled to an electrostatic defined quantum dot [25] within the same nanowire to coherently convert a single electron spin into the polarization state of a photon. Coherent spin to photon conversion makes the long-distance transfer of quantum information between remote stationary qubits a possibility. Additionally, the nanowire transfer technique presented here using PDMS is promising for the realization of efficient electrically driven single-photon sources [26] and solar cells [27] based on one-dimensional nanowires with controlled shape and tapering.

Finally, we comment on possible improvements to our tailored nanowire geometry in order to achieve light extraction efficiencies exceeding 90 % in future work. First, the quality of the gold mirror may be improved by adding a thin dielectric layer between the semiconductor and nanowire as suggested by Friedler et al. [23]. Second, the quantum dot blinking from neutral to charged exciton states can be circumvented by precise control of the charge state with the use of electrostatic gates positioned around an individual nanowire [21, 22] such that a well-defined frequency of the single-photon source is attained. Lastly, the distance between the quantum dot and the cleaved nanowire interface should be precisely controlled to ensure that the quantum dot is positioned at the anti-node of the electric field.

5.9 References

- [1] E. Knill, R. Laflamme and G.J. Milburn, A scheme for efficient quantum computation with linear optics *Nature* **409**, 46–52 (2001).
- [2] N. Gisin, G. Ribordy, W. Tittel, and H. Zbinden, Quantum cryptography. *Rev. Mod. Phys.* **74**, 145–195 (2002).
- [3] S. Strauf, Quantum optics: Towards efficient quantum sources. *Nat. Photon.* **4**, 132–134 (2010).
- [4] M. Pelton et al., Efficient source of single photons: a single quantum dot in a micropost microcavity. *Phys. Rev. Lett.* **89**, 233602 (2002).
- [5] S. Strauf et al., High-frequency single-photon source with polarization control. *Nat. Photon.* **1**, 704–708 (2007).
- [6] J. Claudon et al., A highly efficient single-photon source based on a quantum dot in a photonic nanowire. *Nat. Photon.* **4**, 174–177 (2010).
- [7] T.M. Babinec et al., A diamond nanowire single-photon source. *Nat. Nanotech.* **5**, 195–199 (2010).
- [8] K.G. Lee, A planar dielectric antenna for directional single-photon emission and near-unity collection efficiency. *Nat. Photon.* **5**, 166–169 (2011).
- [9] M. Munsch et al., Dielectric GaAs Antenna Ensuring an Efficient Broadband Coupling between an InAs Quantum Dot and a Gaussian Optical Beam. *Phys. Rev. Lett.* **110**, 177402 (2013).
- [10] O. Gazzano et al., Bright solid-state sources of indistinguishable single photons. *Nat. Commun.* **4**, 1425 (2013).
- [11] T. Heindel et al. *Appl. Phys. Lett.* **96**, 011107 (2010).
- [12] N. Gregersen, T.R. Nielsen, J. Mørk, J. Claudon, and J.M. Gérard, Designs for high-efficiency electrically pumped photonic nanowire single-photon sources. *Opt. Express* **18**, 21204–21218 (2010).
- [13] W. L. Barnes et al., Solid-state single photon sources: light collection strategies. *Eur. Phys. J. D* **18**, 197–210 (2002).
- [14] J. Bleuse et al., Inhibition, Enhancement, and Control of Spontaneous Emission in Photonic Nanowires. *Phys. Rev. Lett.* **106**, 103601 (2011).
- [15] I. Friedler et al., Solid-state single photon sources: the nanowire antenna. *Opt. Express* **17**, 2095–2110 (2009).

- [16] Gregersen, N., Nielsen, T. R., Claudon, J., Gérard, J. M., and Mork, J. *Opt. Lett.* **33**, 1693–1695 (2008).
- [17] M.T. Borgström, V. Zwiller, E.Müller, and A. Imamoglu, Optically bright quantum dots in single nanowires. *Nano Lett.* **5**, 1439–1443 (2005).
- [18] M.H.M. van Weert et al., Selective excitation and detection of spin states in a single nanowire quantum dot. *Nano Lett.* **9**, 1989–1993 (2009).
- [19] J. Heinrich et al., Single photon emission from positioned GaAs/AlGaAs photonic nanowires. *Appl. Phys. Lett.* **96**, 211117 (2010).
- [20] D. Dalacu et al., Selective-area vapor-liquid-solid growth of tunable InAsP quantum dots in nanowires. *Appl. Phys. Lett.* **98**, 251101 (2011).
- [21] M.P.van Kouwen et al., Single electron charging in optically active nanowire quantum dots. *Nano Lett.* **10**, 1817–1822 (2010).
- [22] M. E. Reimer et al., Electric Field Induced Removal of the Biexciton Binding Energy in a Single Quantum Dot. *Nano Lett.* **11**, 645–650 (2011).
- [23] I. Friedler et al, Solid-state single photon sources: the nanowire antenna. *Opt. Lett.* **33**, 2635–2637 (2008).
- [24] Y.M. Niquet and D.C. Mojica, Quantum dots and tunnel barriers in In As/ In P nanowire heterostructures: Electronic and optical properties. *Phys. Rev. B* **77**, 115316 (2008).
- [25] S. Nadj-Perge, S. M. Frolov, E. P. A. M. Bakkers and L. P. Kouwenhoven, Spin-orbit qubit in a semiconductor nanowire. *Nature* **468**, 1084–1087 (2010).
- [26] E.D. Minot et al., Single quantum dot nanowire LEDs. *Nano Lett.* **7**, 367–371 (2007).
- [27] M.D. Kelzenberg et al., Enhanced absorption and carrier collection in Si wire arrays for photovoltaic applications. *Nature Mater.* **9**, 239–244 (2010).
- [28] K.E. Plass et al., Flexible Polymer-Embedded Si Wire Arrays. *Adv. Mater.* **21**, 325–328 (2009).

CHAPTER 6

Gaussian far field emission for ideal fiber-coupling

Quantum communication as well as integrated photonic circuits require single photons propagating in a well-defined Gaussian mode. However, tailoring the emission mode to a Gaussian remains an unsolved challenge for solid-state quantum emitters due to their random positioning in the host material or photonic structure. These limitations are overcome by utilizing nanowire waveguides. In this chapter, we demonstrate Gaussian far-field emission by imaging the luminescence intensity profile in Fourier-space and consequently we demonstrate coupling of single photons into a single-mode optical fiber with negligible insertion losses.

This chapter is based on:

G. Bulgarini, M.E. Reimer, M. Bouwes Bavinck, K.D. Jöns, D. Dalacu, P.J. Poole, E.P.A.M. Bakkers, V. Zwiller, *manuscript under review*.

6.1 Introduction

The most established method to date in order to achieve a very bright single-photon source using nanowires is by coupling the quantum dot emission to the fundamental waveguide mode and to shape the tip of the nanowire for efficiently directing the single photons towards the collection optics [1, 2, 3]. Two alternative routes have been experimentally realized for out-coupling of the light. The first strategy is to shape the nanowire tip with a narrow taper [4]. This narrow taper gradually transfers the guided mode from inside the nanowire waveguide to outside, thus avoiding reflections at the semiconductor-air interface. The expanded mode also reduces the far field emission angle, which enables efficient light collection with limited numerical aperture optics. This gradual transfer of the light from the guided mode to the far field exhibits the best performance at very small tapering angles [5], i.e. the transmission is nearly 100 % for angles smaller than 2° . These very small angles are currently state-of-the-art and are only achievable by growing the nanowire structure with bottom-up techniques [2]. Alternatively, the nanowire can be shaped with a trumpet-like microstructure with the base being smaller than the tip [6]. In this case, the guided mode expands inside the waveguide instead of outside before being transmitted to the far field. To preserve high collection efficiency an anti-reflection coating was implemented. Both approaches promise a Gaussian emission profile, which is ideal for coupling to single-mode fibers for long distance communication. In this work, we measure the photoluminescence intensity of individual quantum dots in tapered nanowire waveguides in the Fourier space and we demonstrate a 99 % overlap of the emission with a Gaussian profile.

The scanning electron micrograph of Fig. 1a presents our system: an InP nanowire, with an ultra-smooth tapered tip (1°), containing a single InAsP quantum dot. Importantly, the site-selective growth with only one quantum dot per nanowire waveguide allows us to select single emitters and image their emission profile down to the single exciton level. Details on the precise positioning of the quantum dot and the bottom-up growth technique in chapter 3 of this thesis.

6.2 Numerical simulations of the far field emission profile

We first investigate the spatial distribution of the quantum dot emission in the far field depending on the dipole orientation associated to the ground state exciton transition. We model a single exciton confined in the quantum dot as an electrical dipole positioned exactly on the nanowire axis and calculate numerically the emission profile propagating upwards from the nanowire tip in the far field using finite difference time domain (FDTD) simulations. We use nanowire dimensions that correspond to the experimentally investigated ones: diameter, $D = 200$ nm, emission wavelength, $\lambda = 950$ nm and 1° taper at the tip.

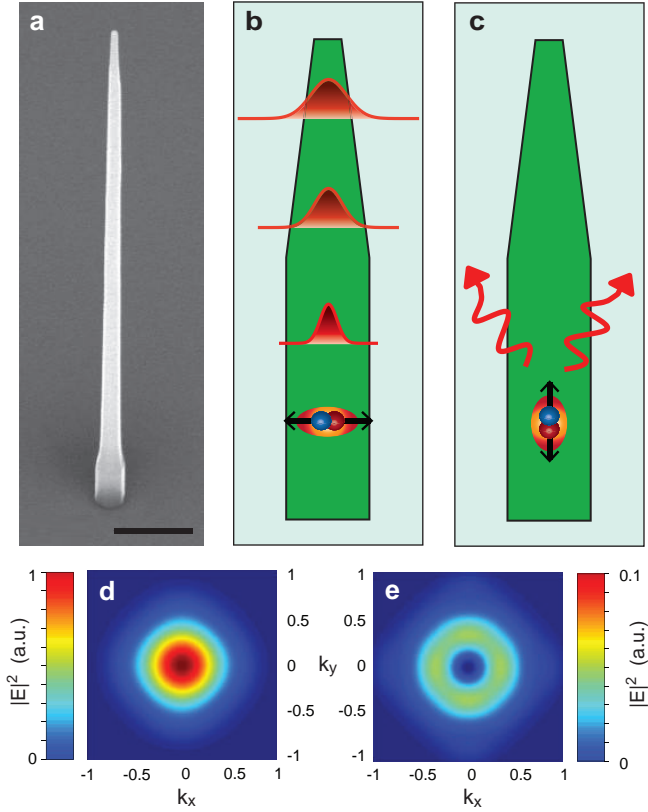


Figure 6.1: Tapered nanowire waveguide. **a**, Scanning electron micrograph of a nanowire waveguide containing a single quantum dot on its axis. Nanowire diameter ~ 200 nm, tapering angle $\sim 1^\circ$. Scale bar is $0.5 \mu\text{m}$. **b,c**, Schematics of waveguide containing a perpendicular **b** or parallel **c** dipole used for FDTD simulations of the emission profile in the far field. Results are shown in the lower panel for **d** perpendicular and **e** parallel dipole. The intensity of the electric field, E , is normalized to the maximum intensity of **d** for both simulations. k_x and k_y indicate the momentum in a plane perpendicular to the nanowire axis.

We consider two orthogonal orientations of the dipole: perpendicular (Fig. 6.1**b**) or parallel (Fig. 6.1**c**) to the nanowire axis. The direction of the electrical dipole is shown schematically in Fig. 6.1**b** and 1**c** as a double sided arrow. In Fig. 6.1**d** and 1**e** we present the calculated electric field intensity of the far field at the top of the nanowire for the configurations displayed in Fig. 6.1**b** and 6.1**c**, respectively. When the quantum dot dipole is oriented perpendicular to the nanowire axis (Fig. 6.1**d**), an excellent coupling ($> 95\%$) of the quantum dot emission to the fundamental waveguide mode is achieved [7]. This emission is guided along the nanowire, adiabatically transferred outside the waveguide to the far field and a large fraction of the light is collected at small angles. In contrast, the emission of a dipole oriented along the nanowire axis couples very poorly to

the fundamental waveguide mode. In this latter case, the emission propagates through non-guided leaky channels, resulting in an emission pattern having a minimum intensity at $k_{\parallel} = \sqrt{k_x^2 + k_y^2} = 0$ and maximum intensity for $k_{\parallel} = 0.34$ (which corresponds to an angle of $\sim 20^\circ$ with the nanowire axis), as shown in Fig. 6.1e. Moreover, because of this weak coupling to guided modes, the integrated electric field intensity in the far field is 11 times lower for the parallel dipole configuration as compared to a perpendicular dipole, which is in agreement with the inhibition of the spontaneous emission that is obtained for suppressed waveguide conditions [8, 9].

section Fourier microscopy of a single quantum emitter In Fig. 6.2 we present the far field emission profile of a single quantum dot in a tapered nanowire waveguide obtained by Fourier imaging. The emission spectrum of the quantum dot at 5 K is displayed in Fig. 6.2a. Photoluminescence spectroscopy and Fourier microscopy have been conducted exciting the quantum dots with a continuous wave HeNe laser at 632.8 nm. The samples were cooled down to 5 K in a closed-cycle dry cryostat and the luminescence was collected with a 0.8 numerical aperture objective situated inside the cryostat. A single peak is observed that is attributed to the recombination of a single exciton in the quantum dot *s*-shell. We verify the single-photon statistics with the correlation measurement shown in the inset.

Operation of the Fourier microscopy technique used to measure the single quantum dot angular emission distribution is explained in the schematics of Fig. 6.2b. The quantum dot emission is collected with a high numerical aperture (NA=0.8) objective with the emitter positioned at the objective focus. As a consequence, the Fourier-plane information of the emitter is obtained at the back-focal plane of the objective [10, 11, 12, 13], where the angular distribution of collected photons is set by their *k*-vector in the reciprocal space. In order to measure the light intensity distribution in the Fourier-space of the quantum dot, we image the back-focal plane of the objective onto a CCD forming a so-called Fourier image. We position a lens of focal distance *f* in the middle of objective and CCD camera as displayed in Fig. 6.2b. Thus, the back-focal plane of the objective is reproduced onto the CCD with a one to one image, thereby mapping the emission intensity as a function of *k* coordinates without altering the emission profile information via transmission through the optical setup. The black dashed lines indicate how the Fourier image is formed on the CCD by classic ray-optics description. For the Fourier microscopy, we used a second CCD camera (pixel size = 13.5 x 13.5 μm) in order to switch from PL spectroscopy to Fourier imaging for each investigated quantum dot. The image on the CCD camera was formed using a lens with focal length *f* = 20 cm. Therefore, the distance from the objective back-focal plane and the lens, as well as the distance between the CCD camera and the lens was chosen to be *d* = 2*f* = 40 cm. The resulting Fourier image has a size of about 300x300 pixels, corresponding to an image of the objective back-focal plane of ~ 4 mm in diameter. For the calibration of the Fourier microscope, we utilized the diffraction on a grating of known pitch and we measured the luminescence from the InP bandgap recombination of individual nanowires reproducing results from the literature [13].

The angular distribution of the single exciton photoluminescence, presented in Fig. 6.2a, is shown in the color plot of Fig. 6.2c. The intensity of collected PL is mapped out in the Fourier-plane of the quantum emitter. We observe that most of the light is collected at small k , corresponding to a small angular distribution.

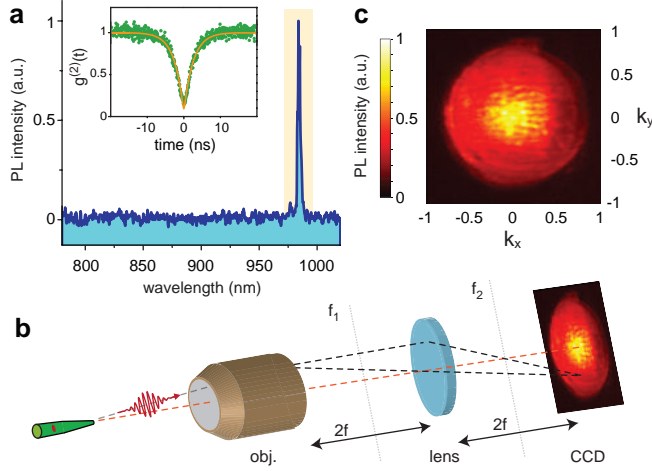


Figure 6.2: Fourier imaging of single quantum emitter. **a**, Typical photoluminescence spectrum of a single quantum dot in a nanowire waveguide well-below exciton saturation. Inset shows typical anti-bunching of the second order intensity correlation function for the single exciton line (green) and fit to the data (yellow, $g^{(2)}(0) = 0.05$). **b**, Schematics of the Fourier microscopy setup. An image of the objective back-focal plane, containing the Fourier-space information of the emitter, is acquired on a silicon CCD. **c** Far field emission profile measured via Fourier imaging from the spectrum in **a**. Most of the photoluminescence is collected around $k = 0$, which indicates a perpendicular orientation of the dipole with respect to the waveguide axis.

This result is in excellent agreement with the numerical simulations presented in Fig. 6.1d and confirms that the electrical dipole associated with a single exciton in the quantum dot is oriented perpendicular to the nanowire axis. We note here that two key requirements are needed to obtain Fourier images of a single quantum emitter. First, the brightness of the source, which is described in our previous work [2], allows for a high count-rate per pixel to image the emission profile of a single quantum dot. Second, the site-selected growth technique that we employ allows for a single quantum dot per nanowire waveguide and thus only a single quantum dot is addressed with a nearly diffraction limited laser spot. This latter feature is of special importance for Fourier imaging, because in order to conserve the k -vector of the photons, no diffraction grating can be utilized for the spectral filtering of the emission lines.

Fig. 6.3a presents the measured 3D far field emission profile of a single quantum dot in a tapered nanowire waveguide. The experimental results are in excellent agreement

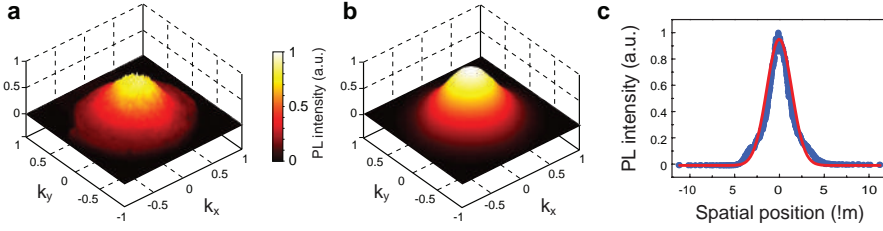


Figure 6.3: Near-unity Gaussian emission profile of single-mode nanowire waveguide. **a**, Three-dimensional image of the emission profile for $D/\lambda = 0.21$. The intensity of the PL collected as a function of k_x and k_y is both color-coded and displayed on the z-axis. The emission profile has a Gaussian shape and matches very well the calculated profile for a taper length of $1\ \mu\text{m}$, shown in **b**. **c**, The overlap integral of the emission profile from **a** with the Gaussian mode of a single-mode fiber is $98.8 \pm 0.1\%$. The excellent overlap is shown with a 2D cut through the measured profile from **a**, in blue color, compared with the guided mode in the fiber displayed in red.

with the numerical calculations shown in Fig. 6.3**b**. Remarkably, the 3D plot evidences a Gaussian far field profile, with an overlap integral of $98.8 \pm 0.1\%$ with the guided mode of a single-mode fiber. We show in Fig. 6.2**c** a 2D cut through the measured profile (blue) in spatial coordinates as compared to the mode of a single-mode fiber, using a mode field diameter of $5.6\ \mu\text{m}$, in red, for a design wavelength of $950\ \text{nm}$. Typically, we observe an average overlap exceeding 97% on several nanowire waveguides operating in the single-mode regime, thus outperforming photonic crystal cavities [12, 14]. Compared to photonic crystals, nanowire waveguides have the additional advantage of having a single emitter per waveguide which is deterministically coupled to the waveguide mode and thus the possibility of fabricating arrays of single-photon emitters. We note that the emission profile from higher excited states of the quantum dot, i.e. p-shell and d-shell, is not Gaussian. Fourier imaging of different shells of the same quantum dot are shown in Fig. 6.4. The blue curve shows Gaussian emission profile from the quantum dot s-shell. Both s-shell transitions (i.e., exciton and biexciton) couple to the fundamental waveguide mode of the nanowire and transfer to the far field with a Gaussian spatial distribution. This feature is particularly important for the generation of polarization-entangled photon pairs utilizing the biexciton-exciton cascade, since both entangled photons propagate in the same emission mode. Conversely, when increasing the excitation power to populate higher order excited states, we observe that a significant fraction of light is emitted at high angles. We observe a 77% overlap with a Gaussian profile for the p-shell emission and 73% overlap for the d-shell. We interpret these results as originating from dipoles oriented both perpendicular and parallel to the nanowire axis. The difference in emission wavelength measured from the s-shell transitions to higher shells ($\sim 15\ \text{nm}$) does not enable substantial coupling to higher order waveguide modes in the nanowire, which are discussed in the following section.

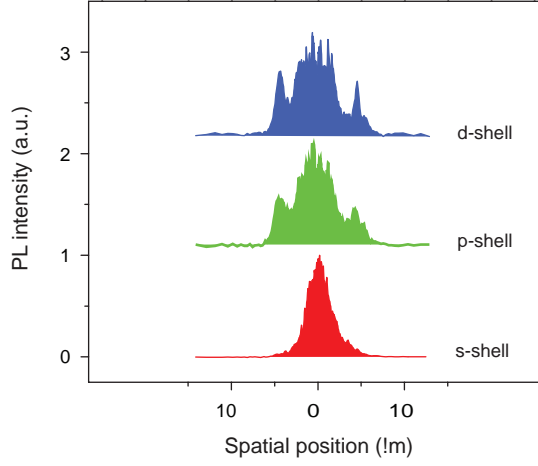


Figure 6.4: Emission profile from excited states. Far field emission profile measured for different shells of same quantum dot. The profiles are plotted in spatial coordinates and vertically offset for clarity. The emission of the quantum dot s-shell (blue) is Gaussian. In contrast, higher excited states such as p-shell (green) and d-shell (blue) exhibit more complex profiles, with high PL intensity collected at larger angles. We attribute this effect to different orientation of the dipoles, both perpendicular and parallel to the nanowire axis, in the quantum dot excited states.

6.3 Diameter dependent analysis: high order waveguide modes

As a function of the nanowire diameter more than one order of waveguide modes becomes allowed in the nanowire [15]. We now investigate the influence of the nanowire diameter on the spatial profile of the emission in the far field. First, we calculate the available guided modes in the nanostructure. Fig. 6.5a shows a calculation of the effective refractive index for the first three guided modes as a function of the nanowire waveguide diameter, D , and the photon wavelength, λ . We observe that as a function of the nanowire diameter, the coupling of the quantum dot emission to different waveguide modes modifies the far field emission pattern. For diameters around 0.2λ , the nanowire is a single-mode waveguide since only propagation of the fundamental guided mode, HE_{11} , is supported. Note that the HE_{11} mode consists of two orthogonal components that in a circularly symmetric waveguide are degenerate. At a larger nanowire diameter, the nanowire becomes a multi-mode waveguide. We show the first two allowed higher order modes, namely the TE_{01} and TM_{01} . The electric field intensity distribution for TE_{01} and TM_{01} guided modes are displayed in Fig. 6.5b .

In Fig. 6.5c we plot four Fourier images obtained by collecting the s-shell photoluminescence of individual quantum dots located in nanowires with increasing diameters.

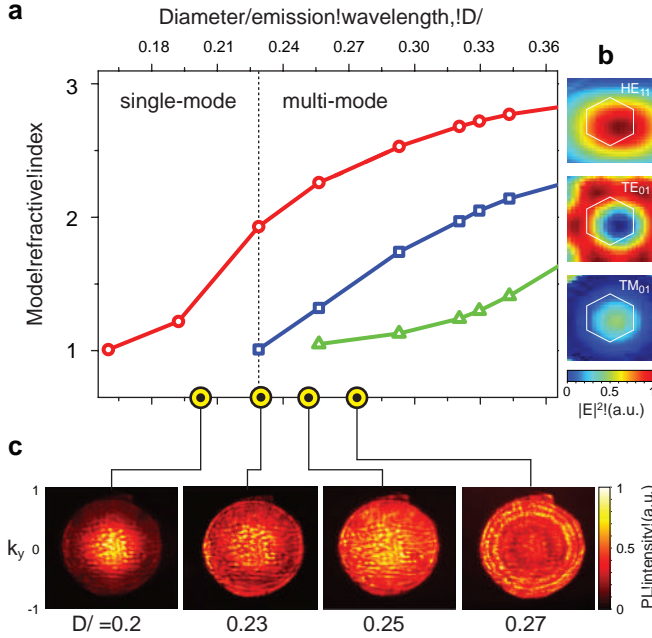


Figure 6.5: Nanowire waveguide modes. **a**, Confined guided modes in a nanowire waveguide at varying nanowire diameter. For D/λ below 0.23 the nanowire supports only a single guided mode (HE_{11}) and becomes a multi-mode waveguide for higher diameters. The first two higher order modes: TE_{01} and TM_{01} are shown. Calculations give equal mode confinement using hexagonal or circular cross-sections [15], for a side s of the hexagon such that $2s = 1.14 \times D$. The spatial distribution of the electric field of the modes inside the waveguide is shown in **b**. **c**, Far field emission pattern of s-shell luminescence from for increasing waveguide diameters. The emission is collected at small angles for a single-mode nanowire waveguide and is directed to higher angles by increasing the nanowire diameter. For diameters larger than $D/\lambda = 0.27$ a doughnut-like emission pattern appears.

When only the HE_{11} mode is supported by the nanowire waveguide ($D/\lambda < 0.23$), the majority of the quantum dot PL is collected at small angles, similarly to Fig. 6.2b. As a general trend, we observe an increase in PL collected at higher angles as the nanowire diameter is enlarged and the nanowire becomes a multi-mode waveguide. As a consequence, the far field emission loses affinity with the Gaussian profile. As observed in the Fourier images at different nanowire diameters, the emission pattern flattens for $D/\lambda = 0.25$ and assumes eventually a subtle doughnut profile with a slightly pronounced maximum of the PL intensity between 30° and 40° at $D/\lambda = 0.27$. This latter emission profile is completely different compared to that of single-mode operation and is attributed to the coupling of the quantum dot emission to the TE_{01} and TM_{01} waveguide modes.

6.4 Coupling to single-mode optical fiber

We finally illustrate the practicality in coupling the Gaussian emission from the tapered nanowire waveguide to a single-mode fiber. To determine the coupling efficiency we measure the single quantum dot PL intensity either with or bypassing the single-mode fiber coupling optics and detecting the photons on a CCD camera after filtering individual exciton lines with a high resolution single grating spectrometer. The schematics of the experiment is shown in Fig. 6.6a. For the coupling to a single-mode optical fiber we utilized a 4X Olympus Plan Achromat Objective, NA 0.1.

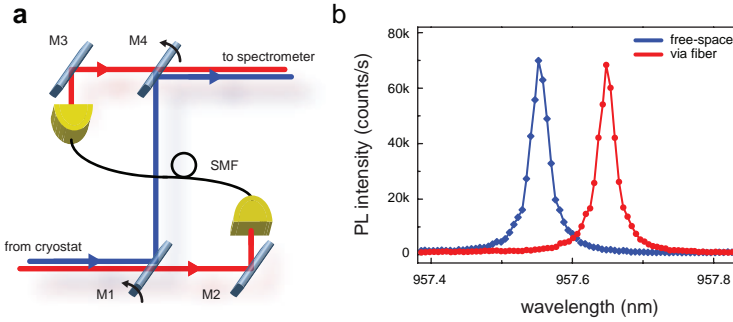


Figure 6.6: Coupling to single-mode fiber. **a**, Experiment schematics. In blue, the photoluminescence (PL) is collected in free-space via mirror M1 and M4. Alternatively, in red the PL is collected via M2, coupled to a single-mode optical fiber (SMF) and directed to the spectrometer via M3. **b**, Comparison of PL counts measured via free-space collection (blue) or via a single-mode fiber (red) on the same CCD. Spectra are horizontally offset for clarity. From the peak integrated count-rate averaged over multiple spectra and two separate coupling attempts we obtain $93 \pm 3\%$ coupling efficiency.

The integrated PL count-rate that we observe via the fiber (red curve in Fig. 6.6b) is $93 \pm 3\%$ of that measured by free-space propagation (blue spectrum). The efficiency is obtained from peak integrate counts averaged over multiple spectra and from two separate coupling attempts. This measured efficiency compares with 45 % reported for self-assembled quantum dots in planar cavities [16] and with 70 % estimated for quantum dots in micropillar cavities [17]. Coupling efficiencies of 73.77 % and 78.59% has been instead measured using laser parametric down-conversion by Giustina et al. [18]. Remarkably, our source provides higher coupling efficiencies than both state-of-the-art on-demand single-photon emitters and probabilistic single-photon sources. The Gaussian profile provided by nanowire waveguides enables us for extending fiber-coupling efficiency towards unity within remaining technological limitations of commercially available optical components.

6.5 Conclusions

We have measured the far field emission profile of individual quantum dots in tapered nanowire waveguides by imaging the photoluminescence intensity distribution in Fourier-space. Our findings indicate that the angular emission distribution depends on the nanowire diameter. For D/λ lower than 0.23, the nanowire supports only the fundamental waveguide mode, HE_{11} , characterized by a Gaussian profile. Importantly, this Gaussian profile is maintained in the far field due to the ultra-smooth tapering towards the nanowire tip. Hence, the quantum dot emission couples into a single-mode fiber with a record efficiency of $93 \pm 3\%$ coupling efficiency. Our results lead the way for the implementation of semiconductor light sources in fiber-based quantum cryptography [19] and communication [20, 21, 22, 23], as well as integrated circuits [24, 25] for processing quantum algorithms [26] using single photons. Moreover, the site-selected growth method provides Gaussian emission without post-growth processing and the possibility of realizing large arrays of independently fiber-coupled bright single-photon sources.

6.6 References

- [1] J. Claudon et al, A highly efficient single-photon source based on a quantum dot in a photonic nanowire. *Nat. Photon.* **4**, 174–177 (2010).
- [2] M.E. Reimer et al, Bright single-photon sources in bottom-up tailored nanowires. *Nat. Commun.* **3**, 737 (2012).
- [3] D. Dalacu et al, Ultraclean emission from InAsP quantum dots in defect-free wurtzite inp nanowires. *Nano Lett.* **12**, 5919–5923 (2012).
- [4] N. Gregersen, T.R. Nielsen, J. Claudon, J.-M. Gerard, and J. Mørk, Controlling the emission profile of a nanowire with a conical taper. *Opt. Lett.* **33**, 1693–1695 (2008).
- [5] J. Claudon, N. Gregersen, P. Lalanne, and J.-M. Gerard, Harnessing light with photonic nanowires, Fundamentals and applications to quantum optics. *ChemPhysChem* **14**, 2393–2402 (2013).
- [6] M. Munsch et al, Dielectric gaas antenna ensuring an efficient broadband coupling between an inas quantum dot and a gaussian optical beam. *Phys. Rev. Lett.* **110**, 177402 (2013).
- [7] I. Friedler et al., Solid-state single photon sources: the nanowire antenna. *Opt. Express* **17**, 2095–2110 (2009).
- [8] J. Bleuse et al., Inhibition, Enhancement, and Control of Spontaneous Emission in Photonic Nanowires. *Phys. Rev. Lett.* **106**, 103601 (2011).
- [9] G. Bulgarini et al., Spontaneous emission control of single quantum dots in bottom-up nanowire waveguides. *Appl. Phys. Lett.* **100**, 121106 (2012).
- [10] M. Andreas Lieb, J. M. Zavislan and L. Novotny, Single-molecule orientations determined by direct emission pattern imaging. *J. Opt. Soc. Am. B* **21**, 1210–1215 (2004).
- [11] A. G. Curto et al, Unidirectional emission of a quantum dot coupled to a nanoantenna. *Science* **329**, 930–933 (2010).
- [12] J. Hagemeier et al, H1 photonic crystal cavities for hybrid quantum information protocols. *Opt. Expr.* **20**, 24714–24726, (2012).
- [13] G. Grzela et al, Nanowire antenna emission. *Nano Lett.* **12**, 5481–5486, (2012).
- [14] M. Toishi, D. Englund, A. Faraon and J. Vuckovic, High-brightness single photon source from a quantum dot in a directional-emission nanocavity. *Opt. Expr.*, **17**, 14618–14626 (2009).

- [15] A.-L. Henneghien, B. Gayral, Y. D., and J.-M. Gerard, Simulation of waveguiding and emitting properties of semiconductor nanowires with hexagonal or circular sections. *J. Opt. Soc. Am. B* **26**, 2396–2403, (2009).
- [16] Y.-M. He et al., On-demand semiconductor single-photon source with near-unity indistinguishability. *Nat. Nanotech.* **8**, 213–217 (2013).
- [17] O. Gazzano et al., Entangling Quantum-Logic Gate Operated with an Ultrabright Semiconductor Single-Photon Source *Phys. Rev. Lett.* **110**, 250501.
- [18] M. Giustina et al., Bell violation using entangled photons without the fair-sampling assumption. *Nature* **497**, 227–230 (2013).
- [19] H. Takasue et al., Quantum key distribution over a 40-dB channel loss using superconducting single-photon detectors. *Nat. Photon.* **1**, 343–348 (2007).
- [20] I. Marcikic et al., Distribution of time-bin entangled qubits over 50 km of optical fiber. *Phys. Rev. Lett.* **93**, 180502 (2004).
- [21] H. Jayakumar et al., Time-bin entangled photons from a quantum dot. *doi: arXiv:1305.2081* (2013).
- [22] K. De Greve et al., Quantum-dot spin-photon entanglement via frequency down-conversion to telecom wavelength. *Nature* **491**, 421–425 (2012).
- [23] W. B. Gao, J. Miguel-Sanchez, P. Fallahi, E. Togan, and A. Imamoglu, Observation of entanglement between a quantum dot spin and a single photon. *Nature* **491**, 426–430 (2012).
- [24] W.H.P. Pernice et al., High-speed and high-efficiency travelling wave single-photon detectors embedded in nanophotonic circuits. *Nat. Commun.* **3**, 1325 (2012).
- [25] J. C. F. Matthews, A. Politi, A. Stefanov, and J.L. O’Brien, Manipulation of multiphoton entanglement in waveguide quantum circuits. *Nat. Photon.* **3**, 346–350 (2009).
- [26] A. Politi, J. C. F. Matthews, and J.L. O’Brien, Shor’s quantum factoring algorithm on a photonic chip. *Science* **325**, 1221 (2009).

CHAPTER 7

Single-photon interference measurements

The coherence length of photon is the distance that the photon can travel while maintaining phase correlations. In this chapter we measure the coherence length of single photons emitted from quantum dots in nanowire with a pure wurtzite crystal structure. The dependence of the coherence length is measured as a function of sample temperature down to 300 mK and as a function of the pump power. Remarkably, we observe that the photon linewidth improves by increasing the excitation power towards exciton saturation. This mechanism is explained by the filling of charge traps in the vicinity of the quantum dot and is supported by Monte Carlo simulations.

This chapter is based on:

M.E. Reimer, G. Bulgarini, R.W. Heeres, B.J. Witek, M.A.M. Veerstegh, D. Dalacu, P.J. Poole, V. Zwiller, *manuscript submitted*.

7.1 Introduction

A quantum network is constituted by local nodes where quantum information is generated, processed, and stored, as well as communication channels between these nodes to coherently transfer quantum states across the entire network [1]. The messengers of choice to distribute quantum information over long distances are single photons since they interact very weakly with the environment, thereby preserving coherence properties. Semiconductor quantum dots embedded in photonic structures are leading candidates to generate coherent and bright sources of single photons with high purity. However, the photon coherence generally degrades by increasing the excitation power, resulting in a broadened emission spectrum [2, 3, 4, 5]. This effect, known as ‘power-broadening’, is attributed to an increase in the charge fluctuations of the quantum dot environment that leads to spectral wandering of the emission line [2]. Here, we report on the single-photon coherence from an ultra-clean material system comprising of a single quantum dot in a pure wurtzite InP nanowire, where dephasing mechanisms are suppressed by either cooling or higher excitation power. Remarkably, in stark contrast to conventional self-assembled quantum dots [2 – 10], we obtain the longest coherence at the highest detected single-photon flux, where the single-photon purity is also preserved. In contrast, cavity-based structures present increased multiphoton events at saturation of the exciton emission due to cavity feeding of other quantum dots or detuned transitions of the same quantum dot [11, 12]. Finally, by cooling the sample to 300 mK we show that the coherence can be enhanced by a factor of ~ 2 as compared to operation at 4.5 K by further suppressing interactions with phonons.

An SEM image of a typical InP tapered nanowire waveguide containing a single InAsP quantum dot used in the present experiments is shown in Fig. 7.1a. The nanowire consists of a pure wurtzite InP crystal structure that is free of stacking faults. Importantly, this crystal phase purity is obtained for nanowire core diameters of 25 nm or less and is maintained during shell growth to construct the waveguide [13]. The crystal phase purity is essential in obtaining a narrow emission spectrum. In fact, the measured linewidth is reduced by more than two orders of magnitude as compared to nanowires with stacking faults [14, 15, 16, 17], since such defects in the crystalline structure acts as efficient charge traps.

7.2 Single-photon coherence measurements

To determine the coherence length (time) of single photons originating from quantum dots in nanowire waveguides, and obtain a precise measurement of the emission spectrum, we employ field-correlation measurements using a Michelson interferometer [18, 19, 20]. The quantum dot emission is coupled to a single mode fiber before entering the Michelson interferometer in order to ensure good overlap of the spatial modes in the interferometer. When the path difference between both paths is varied we observe

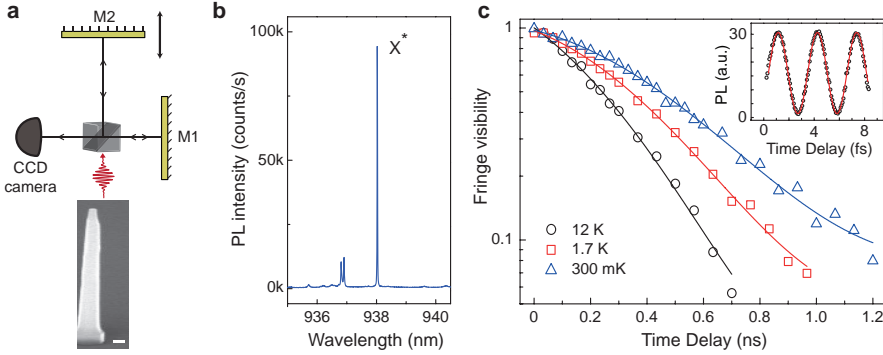


Figure 7.1: Single-photon interference measurements at 300 mK. **a**, Schematic view of Michelson interferometer comprising of a beam-splitter, fixed mirror M1, movable mirror M2 and charge-coupled device (CCD) detector. Single photons are emitted by a quantum dot in the tapered nanowire waveguide. **b**, Quantum dot photoluminescence spectrum. X*: single charged exciton. **c**, First-order correlation measurements of a single quantum dot at 300 mK (blue triangles), 1.7 K (red squares), and 12 K (black circles). The solid lines are a fit to the data using a Voigt profile (described in the text). Shown in the inset are the interference fringes obtained at identical distance in the two arms of the Michelson interferometer.

single-photon interference through oscillations in the measured intensity at the interferometer output. The decay of the interference fringe visibility in the $g^{(1)}(\tau)$ measurement is set by the temporal coherence of the source, as explained in chapter 3.

The photoluminescence spectrum of the quantum dot used for the field-correlation measurements is presented in Fig. 7.1b. The brightest line for this particular quantum dot at 938 nm is a charged exciton, X*. Assignment of X* is confirmed by a combination of both polarization analysis (i.e., absence of fine-structure splitting) and cross-correlation measurements. At saturation of the exciton emission, we measured count rates of 460 kilocounts per second on a silicon avalanche photodiode (APD) under pulsed excitation. We excite the dot above the nanowire bandgap at 750 nm using 3 ps laser pulses at a repetition rate of 76 MHz. Accounting for transmission losses in the optical setup ($\sim 1.4(1)\%$), we calculate a single-photon source efficiency of 43(4)%, which can be further enhanced by integrating a bottom gold mirror with a thin dielectric at the base in order to collect the downward emitted photons as shown in chapter 5.

The results of the single-photon interference measurements are presented in Fig. 7.1c for three different temperatures from 12 K down to 300 mK. The inset of Fig. 7.1c depicts the raw interference fringes of the charged exciton line at 300 mK obtained around zero path difference between both arms of the Michelson interferometer for a step size of 20 nm. A fit to the data (red line) yields a maximum raw fringe visibility of 95 %. Correcting for the Michelson system response, a maximum fringe visibility of 99% is attained. The photon coherence length (time) is extracted from the decay of fringe visibility observed for increasing path difference (time delay).

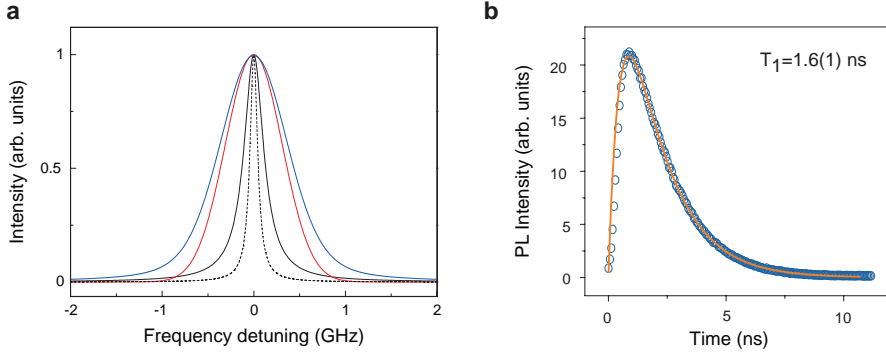


Figure 7.2: Exciton emission lineshapes **a**, Single quantum dot emission linewidth is represented by a Voigt profile (blue) with full-width half-maximum of 880(90) MHz, which is a convolution of a Lorentzian of with 260(40) MHz (black) with a Gaussian (red) lineshape (full-width of 730(80) MHz). These parameters are extracted from the fit of the interference data at 300 mK. The dotted black line shows the lifetime Fourier-transform limit of 100 MHz. **b**, Measurement of the exciton lifetime, T_1 , of 1.6(1) ns. The fit to the data (yellow curve) is a mono-exponential decay convoluted with the photodetector time response.

We now discuss the nature of the lineshape that is obtained from the single-photon interference measurements in Fig. 7.1c. The decay in the visibility of interference fringes suggests a Voigt profile, which is an inhomogeneously broadened Lorentzian. During the measurement time needed to acquire each visibility data point (~ 5 minutes in our measurements), dephasing processes that are longer than the exciton lifetime lead to Gaussian broadening of the excitonic Lorentzian lineshape. From a fit to the data (open symbols) at 300 mK, we extract a homogeneous linewidth of 260(40) MHz and inhomogeneous linewidth of 730(80) MHz. Details of the fit are in the chapter appendix. Both components of the Voigt profile are plotted in Fig. 7.2a, represented by the black (Lorentzian) and red (Gaussian) line. The convolution of both lineshapes yields the measured Voigt profile with a full-width half-maximum of 880(90) MHz, shown in blue. For comparison the dotted black line shows the lifetime Fourier-transform limit of 100 MHz, for our measured exciton lifetime, T_1 , of 1.6(1) ns. Time-resolved photoluminescence measurement of the exciton lifetime is shown in Fig. 7.2b and fit with a mono-exponential decay convoluted with the system response.

The deviation of the measured linewidth from the Fourier-transform limit is mainly due to charge noise [21]. Counteracting this broadening mechanism is crucial for implementation of multiple sources in a quantum network since broadenings will be uncorrelated in independent quantum dots and thus unavoidably lead to deterioration of two-photon interference visibility [22, 23, 24]. We point out that this Gaussian line broadening mechanism due to charge fluctuations in the environment is also observed in resonant fluorescence [3, 4].

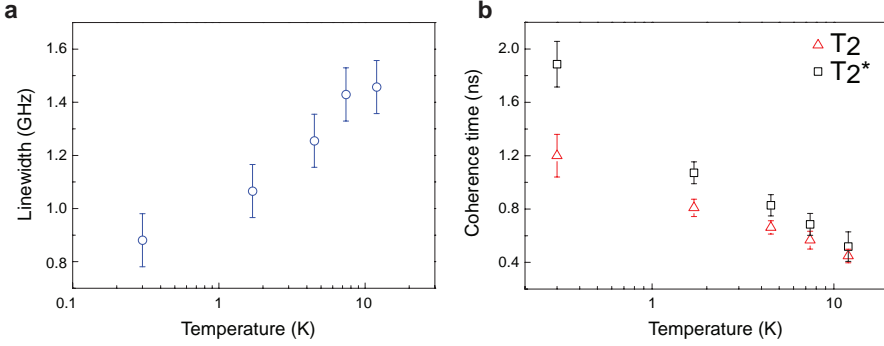


Figure 7.3: Temperature dependent single-photon coherence **a**, Single quantum dot emission linewidth measured as a function of temperature. As expected, broadening mechanisms are increasingly suppressed by cooling down the sample. **b**, Coherence time, T_2 , and corresponding pure dephasing time, T_2^* , extracted from the fit to the lineshapes. At 300 mK the pure dephasing time is longer than the exciton lifetime, T_1 , of 1.6(1) ns.

7.3 Counteracting dephasing mechanisms

In Fig. 7.3a, we present the exciton emission linewidth as a function of temperature. As expected, decreasing the temperature results into an enhancement in the single-photon coherence as interactions with phonons are suppressed [25]. In Fig. 7.3b, we present the coherence time, T_2 , as extracted from the fitted Voigt profile, and corresponding pure dephasing time, T_2^* , from the relation

$$\frac{1}{T_2} = \frac{1}{2T_1} + \frac{1}{T_2^*}, \quad (7.1)$$

as a function of temperature. Here, T_2^* is the pure dephasing, and T_2 is the coherence time that includes both relaxation and pure dephasing processes. Decreasing the temperature results into an enhancement in the single-photon coherence as interactions with phonons are suppressed. Both T_2 and T_2^* increase while cooling. Interestingly, the coherence time doubles to 1.2(2) ns when cooling from 4.5 K to 300 mK, while the pure dephasing time surpasses the measured exciton lifetime at 300 mK. Furthermore, we present in Fig. 7.4a the single-photon interference measurements at 300 mK as a function of excitation power. The longest coherence at saturation of the exciton emission where the measured count rates on the single-photon detectors are highest (see Fig. 7.4b). The resulting emission linewidth, to be discussed subsequently, is reduced from 2.7(3) GHz at the lowest excitation power to 0.8(2) GHz at saturation of the exciton emission (see Fig. 7.5d). Excellent fits to the data in Fig. 7.4a are made by fixing T_2 to 1.2(2) ns at the saturation power, P_{sat} , of the quantum dot emission and increasing the width of Gaussian broadening as the excitation power is reduced. We point out that the observation of power narrowing for the single quantum dot emission spectrum is

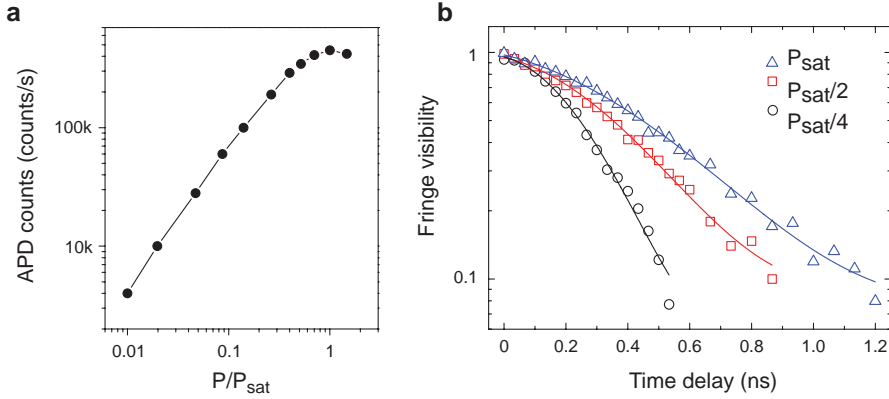


Figure 7.4: Power dependence of the emission linewidth. **a**, First-order correlation measurements of a single quantum dot at 300 mK as a function of excitation power, P . The best coherence is observed at exciton saturation, $P_{\text{sat}} \sim 1 \mu\text{m}$. **b**, Power dependence of charged exciton emission line. The exciton emission saturates at 460,000 counts per second measured on an avalanche photodiode.

not limited to 300 mK, but is also observed at temperatures up to 12 K. This outcome suggests that the activation energy of charge traps in the nanowire is above 12 K. In our nanowires, we observe weak emission associated with donor-acceptor levels, at approximately 50 meV below the pure wurtzite InP peak at 1.49 eV [13]. We attribute these shallow donor/acceptor trap sites in our nanowires to carbon as this element is present in chemical beam epitaxy systems.

It is worth mentioning why we reach the power narrowing regime for the first time. We attribute this effect to both the clean crystal structure and the reduced nanowire dimensionality. Photo-generated charges remain localized in the vicinity of the quantum dot and may saturate the filling of nearly all of the surrounding charge traps at high excitation photon flux. In contrast, saturating trap sites surrounding a quantum dot positioned in a bulk sample is extremely difficult owing to the significant increase in available material, where charge carriers may diffuse to charge traps located far away from the quantum dot.

7.4 Monte Carlo simulations of the quantum dot emission spectrum

We now present simulations of the quantum dot emission spectrum which take into account charge fluctuations in the quantum dot environment. We model 1000 randomly positioned electron and hole traps in the nanowire, corresponding to a density of $\sim 1 \times 10^{16} \text{ cm}^{-3}$.

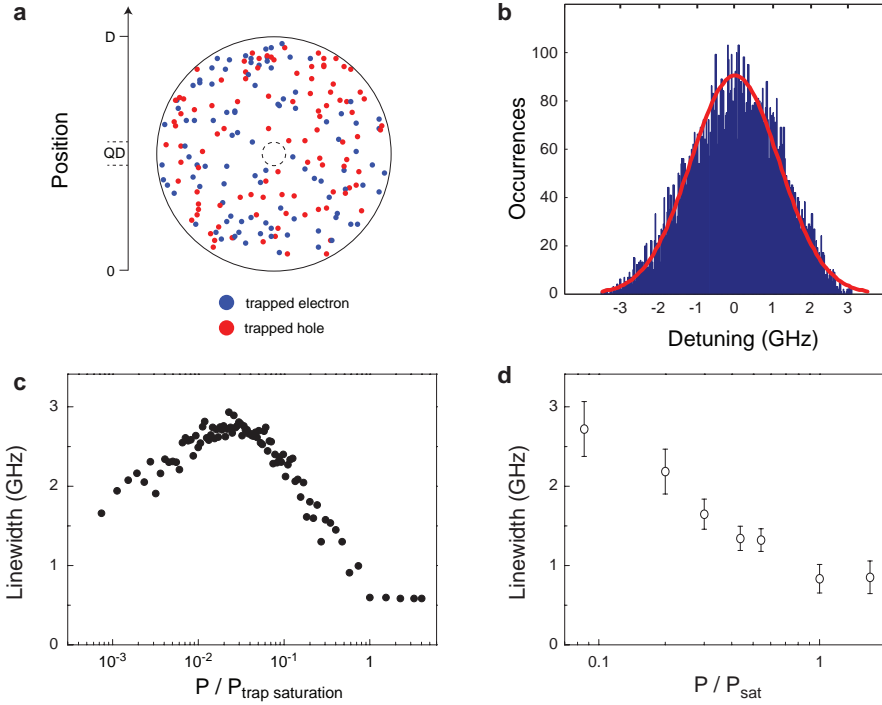


Figure 7.5: Simulations of the Gaussian broadening. **a**, A projection of randomly positioned trap sites for both electrons (blue) and holes (red dots) over a 400 nm nanowire segment. The nanowire diameter, D , is 200 nm. The quantum dot, QD, in the center of the nanowire is represented as a dotted circle with diameter of 20 nm. **b**, Resulting histogram of Stark shift induced on the exciton transition for 10,000 random charge configurations. Due to the random nature of charge fluctuations, the line broadening is Gaussian (fit in red). **c**, Monte Carlo simulations showing the quantum dot emission linewidth as a function of excitation power. **d**, Experimental emission linewidth as a function of excitation power at 300 mK. P_{sat} is the excitation power required to saturate the X^* emission.

This trap density yields about 50 trap sites within a radius of 200 nm from the dot. Fig. 7.5a displays the random positioning of electron (blue) and hole (red) trap sites in the nanowire. Trap sites in the nanowire are filled by charge carriers photo-generated by the excitation laser. The interaction between the trapped charges and the quantum dot exciton results in a shifting of the exciton emission energy via the Stark effect. The result of the Monte Carlo simulations iterating over 10000 possible charge configurations of traps occupied with probability of 0.5 is shown in Fig. 7.5b. Owing to the random nature of the charge fluctuations, the resulting broadening of the emission line is a Gaussian (red fit to the histogram).

Our Monte Carlo simulation gives the emission linewidth as a function of trap occupancy. The correspondence between laser power and trap occupancy follows a non-linear

relation and is calculated with a rate equation model presented in the second appendix to this chapter. The results of the emission linewidth as a function of excitation power used to saturate the charge traps are shown in Fig. 7.5c. We identify two regimes with excitation power. First, we observe that the linewidth broadens with increasing excitation power. This regime is consistent with the typical power broadening observed for self-assembled quantum dots. The broadest emission linewidth is attained when half of the trap sites are occupied, thereby providing the highest number of possible charge configurations in the quantum dot environment. By further increasing the excitation power, the power narrowing regime is reached corresponding to a decrease in the emission linewidth of 2.5 GHz/decade. In this power narrowing regime, the higher number of traps sites that are occupied results in a reduction of the disorder in the quantum dot environment. The linewidth of the dot may therefore be used to probe the entropy of the system. Finally, no further improvement of the emission linewidth with increasing power is expected for saturated occupation of the charge traps. The simulation results are in very good agreement with the observed emission linewidth decrease of 1.9 GHz per decade with increasing power as presented in Fig. 7.5d.

7.5 Conclusions

The first single-photon coherence measurements on quantum dots embedded in nanowires are reported, with narrowest linewidth of 880 MHz obtained at 300 mK. The narrowest linewidth is not attained at very low excitation power, but at the excitation power where the exciton photon flux is the highest. We overcame power broadening by growing ultraclean wurtzite InP nanowires without stacking faults to reduce the trap density. This reduced trap density combined with the nanowire geometry allowed us to fill nearly all of the trap sites surrounding the quantum dot and thereby reduce the charge-induced broadening of the exciton emission.

7.6 Appendix 1: single-photon interference and spectral lineshapes

The interference fringe visibility is defined as:

$$V = \frac{I_{\max} - I_{\min}}{I_{\max} + I_{\min}}, \quad (7.2)$$

where I_{\max} and I_{\min} correspond to the case of optimal constructive and destructive interference, respectively. We measure a maximum raw interference fringe visibility for the quantum dot of 95 %, whereas for a coherent laser with 4 MHz linewidth we obtain a raw interference fringe visibility of 96 %. In all of the single-photon interference measurements, the fringe visibility is corrected for the Michelson system response obtained with the narrow-band laser in order to account for the phase instability of the interferometer.

The form of the fringe visibility decay, $g^{(1)}(\tau)$, for coherent light depends on the type of spectral broadening that applies. For light with a Lorentzian lineshape, the decay of the fringe visibility is exponential, where:

$$g^{(1)}(\tau) \sim \exp\left(-\frac{|\tau|}{T_2}\right). \quad (7.3)$$

The relationship between the full-width half-maximum in frequency, Δf , and the coherence time, T_2 , for the Lorentzian lineshape is given by:

$$\Delta f_L = \frac{1}{\pi T_2}, \quad (7.4)$$

whereas for a Gaussian lineshape, the fringe visibility decay follows the form:

$$g^{(1)}(\tau) \sim \exp\left[-\frac{\pi}{2} \left(\frac{\tau}{\tau_c}\right)^2\right]. \quad (7.5)$$

In this case, the full-width half-maximum for a Gaussian is:

$$\Delta f_G \sim \frac{\sqrt{2 \ln 2}}{\sqrt{\pi} \tau_c}, \quad (7.6)$$

where τ_c is the coherence time for the Gaussian component. The decay of the fringe visibility were fit for all data using a Voigt profile. In the time domain the Voigt profile is a product of a Gaussian and Lorentzian:

$$g^{(1)}(\tau) \sim \exp\left[-\frac{\pi}{2} \left(\frac{\tau}{\tau_c}\right)^2 - \frac{|\tau|}{T_2}\right]. \quad (7.7)$$

The resulting Voigt profile with a full-width half-maximum is [24]:

$$\Delta f_V = 0.535 \Delta f_L + \sqrt{0.217 \Delta f_L^2 + \Delta f_G^2}. \quad (7.8)$$

7.7 Appendix 2: details of Monte Carlo simulations

Here we present details of our simulation model that explains the broadening mechanism of a quantum dot exciton emission line due to the fluctuating charge environment. We account for the dynamics of charges randomly distributed in the vicinity of the quantum dot in order to calculate the exciton emission spectrum. The model describes a quantum dot in a nanowire, but it is easily extendable to other geometries.

Power dependent population of trapped charges

The model accounts for the line broadening of the quantum dot exciton emission due to the interaction with charges in the environment. Electrons and holes are photo-generated by the above-bandgap excitation laser in the nanowire. We assume that those charges immediately separate and are captured into trap sites in the nanowire at a rate Γ_g . We assume the trapping time to be faster than the exciton lifetime in the quantum dot, which is found to range from 2 to 20 ns, depending on the nanowire diameter [26]. The interaction between the trapped charges and the quantum dot exciton results in a detuning of the exciton emission energy. Trapped charges have a finite probability of recombination at a recombination rate Γ_r . Alternatively, a trapped charge may overcome the trapping potential and escape the trap site with an escape rate Γ_e . We employed the following rate equation in order to obtain a relation between the density of occupied charge traps in the quantum dot environment and the laser excitation power.

$$\frac{dm}{dt} = (N - m)\Gamma_g - m\Gamma_e - m\Gamma_r, \quad (7.9)$$

Where m is the density of occupied traps and N is the total density of traps. The density of occupied trap sites increase at a rate Γ_g and it is proportional to the density of free trap sites, $N-m$.

$$\Gamma_g = \frac{\eta}{N} \cdot \frac{P}{h\nu \cdot A \cdot L} \quad (7.10)$$

The trap generation rate, Γ_g is inversely proportional to the total number of traps and proportional to η , which represents the trapping probability for a photo-generated charge. Moreover, the trap generation rate is proportional to the ratio between excitation power, P , and photon energy $h\nu$, spot area A and sample thickness L , under the assumption of unity absorption efficiency used for simplicity.

We introduce here the excitation photon flux that is the number of photons per unit time and unit area impinging on the sample. The photon flux is directly proportional to the excitation power:

$$\Phi = \frac{P}{(h\nu \cdot A)}. \quad (7.11)$$

Two mechanisms are responsible to reduce the density of occupied traps in Eq. 7.9: escape and recombination. At low temperatures such as few kelvin, we assume that

thermally activated escape is suppressed and the absorption of a laser photon is needed to overcome the trapping potential. The escape rate is hence proportional to excitation photon flux with a probability, x , that a charge is re-excited by the laser:

$$\Gamma_e = \frac{x\Phi}{N \cdot L}. \quad (7.12)$$

By combining 7.10 and 7.11, equation 7.9 can be written in the following form:

$$\frac{dm}{dt} = (N - m) \frac{\eta}{L} \frac{\Phi}{N} - m \frac{x}{L} \frac{\Phi}{N} - m\Gamma_r, \quad (7.13)$$

At equilibrium we have a steady number of trapped charges.

$$\frac{dm}{dt} = 0. \quad (7.14)$$

Hence, the density of occupied traps in the semiconductor structure is

$$m = \frac{\Phi \frac{\eta}{L}}{\Phi \left(\frac{\eta+x}{L} \right) / N + \Gamma_r}. \quad (7.15)$$

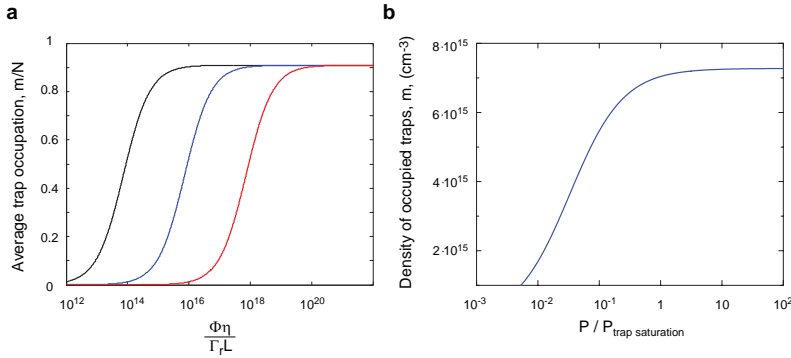


Figure 7.6: **a**, Average trap occupation for trap density, N , equals to $8 \times 10^{13} \text{ cm}^{-3}$ (black), $8 \times 10^{15} \text{ cm}^{-3}$ (blue) and $8 \times 10^{17} \text{ cm}^{-3}$ (red). **b**, Density of occupied traps as a function of the excitation power, P , compared to the power required for trap saturation obtained from **a**.

Fig. 7.6 shows the average trap occupation for different trap densities as a function of excitation photon flux. The probability of laser-induced escape process is assumed to be 10 % as compared to the trapping probability. This sets the occupation saturation at 90 % of the total number of traps. We observe that a higher density of traps implies a required higher power to saturate their occupation. This excitation power may extend beyond the power used for saturating the exciton population in the quantum dot.

Numerical simulations of the exciton emission spectrum

The interaction between fluctuating trapped charges on the exciton emission line is calculated using Monte Carlo simulations. We first generate randomly distributed trap sites for electrons and holes in the nanowire. The nanowire is a cylinder of 200 nm diameter and 4 micron length. No trap sites are placed in the quantum dot. These traps are randomly occupied with a probability set by the average trap occupation, which is calculated via the rate equation model presented in the previous section. Detuning of the exciton emission energy arises from interaction with the charge environment and is determined by the Stark effect. The electric field generated from a trapped charge is calculated in the single particle picture,

$$F = e/4\pi\epsilon r^2, \quad (7.16)$$

where ϵ is the dielectric constant of the semiconductor matrix and r is the distance between the exciton and the trapped charge. The Stark shift of the exciton subject to an electric field, F , is given by,

$$V = \beta F^2, \quad (7.17)$$

where β is a material dependent constant. The Stark shift is thus proportional to $1/r^4$. For our material system, InAsP quantum dot embedded in InP, we used the value of β calculated for InAs in InP of $1.7 \mu\text{eV}\cdot\text{cm}^2/\text{kV}^2$ [27] and the dielectric constant of InP, $\epsilon = 12.4$.

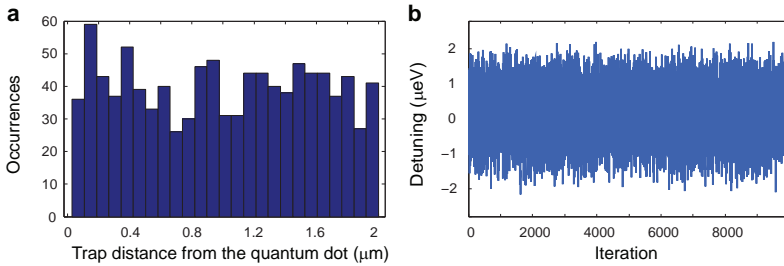


Figure 7.7: **a**, Distribution of the distance of trap sites with respect to the quantum dot for 1000 electron traps. **b**, Stark shift induced on the exciton transition for each charge configuration. We consider 1000 electron traps and 1000 hole traps at an average trap occupancy of 0.5.

In the example of Fig. 7.7a, we show the statistical distribution of 1000 trapped charges as a function of the distance to the quantum dot center. We calculate the Stark shift for 10000 randomly selected configurations of electrons and holes in the traps. As an example, Fig. 7.7b shows a simulation for an average trap occupancy of $\frac{m}{N} = 0.5$. The statistical distribution of the Stark shift is plotted in the histogram of Fig. 7.5b in the main text of the chapter.

We now calculate the exciton emission broadening as a function of the average trap occupation, m/N . In this further step, we include in the model the possibility for the quantum

dot environment of being n-doped. This background doping is often found in nanowires and typically attributed to the growth mechanism. We choose for the simulation shown in Fig. 7.8 a concentration of $8 \times 10^{14} \text{ cm}^{-3}$ for n-dopants. The result of the excess electron is to increase the occupation for electron traps compared to the non-doped case. We observe in the simulation results shown in Fig. 7.8 that the exciton transition linewidth increases while increasing the average trap occupation from 0 to 0.5, where the line broadening is maximum. The interaction with the fluctuating environment broadens the energy spectrum of the emitted photons. The maximum multiplicity of charge configurations in the environment is thus found for a trap occupation probability of 0.5. If more than half of the traps are filled the system goes towards a more stable charge environment: the number of possible charge configurations is limited and the emission linewidth decreases. Eventually, when all the traps are filled, the charge environment of the quantum dot would be stationary. However, this condition is never fulfilled because of the finite of de-trapping charges via laser absorption. The background doping of the quantum dot environment increases the broadening at very low excitation power thus giving asymmetry of the simulated linewidth curve as a function of trap occupation. Furthermore, depending on the specific position of the randomly located charges, the maximum of the curve varies from simulation to simulation in a range from 6 μeV to 11 μeV . This explains the variance in quantum dot emission linewidth from quantum dot to quantum dot on the same sample. Finally, by combining the rate equations with the Monte Carlo simulations, we obtain the results presented in Fig. 4c in the main text of the chapter where the line broadening is plotted as a function of excitation power.

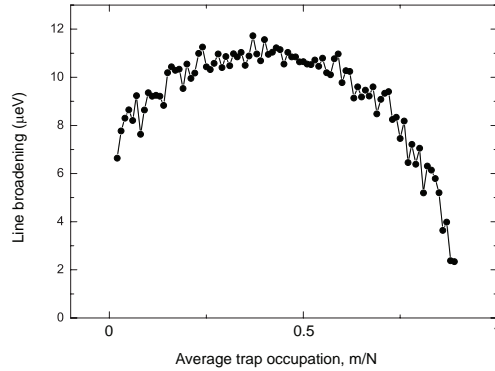


Figure 7.8: Result of Monte Carlo simulations of the exciton line broadening for 1000 electron traps and 1000 hole traps, corresponding to a density of $8 \times 10^{15} \text{ cm}^{-3}$, as a function of average trap occupation.

Transcription of the Matlab code

```

Rn=1000 Number of random generated traps
e=1.6e-19; eps=12.4*8.85e-12 Beta=1.7e-16;
for t = 1:Rn
Generation of random position in a circle.
rc=100e-9; Nanowire radius
r0=10e-9; Quantum dot radius, no traps are supposed to be inside the
quantum dot
a=2*pi*rand; b=2*pi*rand;
r=r0+(rc-r0)*sqrt(rand);
Xn(t)=(r)*cos(a)+x1;
Yn(t)=(r)*sin(a)+y1;
Random position along the nanowire length
Zn(t)=(-1 +(2)*rand(1))*2e-6;
Holes coordinates
Xh(t)=(r)*cos(b)+x1;
Yh(t)=(r)*sin(b)+y1;
Zh(t)=(-1 +(2)*rand(1))*2e-6;
Distance of the trapped charge from the origin where the quantum dot
exciton is assumed to be located.
dist_n(t) = sqrt(Xn(t).^2 + Yn(t).^2 + Zn(t).^2);
dist_h(t) = sqrt(Xh(t).^2 + Yh(t).^2 + Zh(t).^2);
for i=1:imax Iteration loop
for t=1:Rn Random sites occupation
pr=rand(1);
If random number overcome (1-Probability of occupation), the trap is
occupied and we thus calculate the electric field F for the Stark
interaction. Else, the trap is unoccupied and has no interaction with
the quantum dot exciton.
if pr >= (1-P-doping)
F=e/(4*pi*eps*dist_n(t)^2);
else
F=0;
end;
Trapped holes have a contribution opposite in sign compared to the
trapped electrons.
if pr >= (1-P)
Fh=-e/(4*pi*eps*dist _ h(t)^2) ;
else
Fh=0;
end;

```


Position with respect to the origin.

```
coord(t)=(Xn(t)/abs(Xn(t))+Yn(t)/abs(Yn(t))+Zn(t)/abs(Zn(t)));
```

Holes coordinates

```
coord _ h(t)=(Xh(t)/abs(Xh(t))+Yh(t)/abs(Yh(t))+Zh(t)/abs(Zh(t)));
```

Stark shift calculation for one trap site for electrons and one for holes in eV

```
V(t)=((Beta*F.2) * coord(t)) + ((Beta*1e-16*Fh.2) *coord _ h(t));
```

Total Stark shift obtained by the sum of the individual contributions.

```
Shift(i) = sum(V);
```

7.8 References

- [1] H.J. Kimble, The quantum internet. *Nature* **453** 1023–1030 (2008).
- [2] A. Berthelot et al., Unconventional motional narrowing in the optical spectrum of a semiconductor quantum dot. *Nat. Phys.* **2**, 759–764 (2006).
- [3] S. Ates et al., Post-selected indistinguishable photons from the resonance fluorescence of a single quantum dot in a microcavity. *Phys. Rev. Lett.* **103**, 167402 (2009).
- [4] Y.-M. He, On-demand semiconductor single-photon source with near-unity indistinguishability. *Nat. Nanotech.* **8**, 213–217 (2013).
- [5] O. Gazzano et al., Bright solid-state sources of indistinguishable single photons. *Nat. Commun.* **4**, 1425 (2013).
- [6] J. Houel et al., Probing Single-Charge Fluctuations at a GaAs/AlAs Interface Using Laser Spectroscopy on a Nearby InGaAs Quantum Dot. *Phys. Rev. Lett.* **108**, 107401 (2012).
- [7] H.D. Robinson and B.B. Goldberg, Light-induced spectral diffusion in single self-assembled quantum dots. *Phys. Rev. B* **61**, 5086–5089 (2000).
- [8] A. Muller et al., Resonance Fluorescence from a Coherently Driven Semiconductor Quantum Dot in a Cavity. *Phys. Rev. Lett.* **99**, 187402 (2007).
- [9] S. Stufliker, P. Ester, A. Zrenner and M. Bichler, Power broadening of the exciton linewidth in a single InGaAs/GaAs quantum dot. *Appl. Phys. Lett.* **85**, 18 (2004).
- [10] M.E. Ware et al., Polarized Fine Structure in the Photoluminescence Excitation Spectrum of a Negatively Charged Quantum Dot. *Phys. Rev. Lett.* **95**, 177403 (2005).
- [11] J. Suffczynski et al., Origin of the optical emission within the cavity mode of coupled quantum dot-cavity systems. *Phys. Rev. Lett.* **103**, 027401 (2009).
- [12] M. Winger et al., Explanation of photon correlation in the far-off-resonance optical emission from a quantum-dot-cavity system. *Phys. Rev. Lett.* **103**, 207403 (2009).
- [13] D. Dalacu et al, Ultraclean emission from InAsP quantum dots in defect-free wurtzite InP nanowires. *Nano Lett.* **12**, 5919–5923 (2012).
- [14] N. Sköld, et al., Microphotoluminescence studies of tunable wurzite inasp quantum dots embedded in wurzite inp nanowires. *Phys. Rev. B* **80**, 041312 (2009).
- [15] J. Heinrich et al., Single photon emission from positioned GaAs/AlGaAs photonic nanowires. *Appl. Phys. Lett.* **96**, 211117 (2010).

- [16] D. Dalacu et al., Selective-area vapor-liquid-solid growth of tunable InAsP quantum dots in nanowires. *Appl. Phys. Lett.* **98**, 251101 (2011).
- [17] M.E. Reimer et al., Bright single-photon sources in bottom-up tailored nanowires *Nat. Commun.* **3**, 737 (2012).
- [18] C. Kammerer et al., Interferometric correlation spectroscopy in single quantum dots. *Appl. Phys. Lett.* **81**, 2737–2739 (2002).
- [19] V. Zwiller, T. Aichele and O. Benson, Single-photon fourier spectroscopy of excitons and biexcitons in single quantum dots. *Phys. Rev. B* **69**, 165307 (2004).
- [20] C. Matthiesen, A.N. Vamivakas and M. Atatüre, Subnatural linewidth single photons from a quantum dot. *Phys. Rev. Lett.* **108**, 093602 (2012).
- [21] A.V. Kuhlmann et al., Charge noise and spin noise in a semiconductor quantum device. *Nat. Phys.* **9**, 570–575 (2013).
- [22] E.B. Flagg, Interference of single photons from two separate semiconductor quantum dots. *Phys. Rev. Lett.* **104**, 137401 (2010).
- [23] R.B. Patel et al., Two-photon interference of the emission from electrically tunable remote quantum dots. *Nat. Photon.* **4**, 632 (2010).
- [24] P. Gold, Two-photon interference from remote quantum dots with inhomogeneously broadened linewidths. *Phys. Rev. B* **89**, 035313 (2014).
- [25] M. Bayer and A. Forchel, Temperature dependence of the exciton homogeneous linewidth in InGaAs/GaAs self-assembled quantum dots. *Phys. Rev. B* **65**, 041308 (2002).
- [26] G. Bulgarini et al., Spontaneous emission control of single quantum dots in bottom-up nanowire waveguides. *Appl. Phys. Lett.* **100**, 121106 (2012).
- [27] M.E. Reimer et al., Single electron charging in deterministically positioned InAs/InP quantum dots. *Appl. Phys. Lett.* **94**, 011108 (2009).

CHAPTER 8

Nanowire opto-electronics: a quantum dot in a nanowire photodiode

Interfacing single photons and electrons is a crucial for future opto-electronic devices needed to share quantum information between remote solid-state qubits. Semiconductor nanowire p-n junctions are attractive candidates for the conversion of single electron-hole pairs into light as a quantum light-emitting diodes. Similarly, single photons may be converted into single excitons for transferring information from a flying qubit to a stationary qubit in a nanowire. In this chapter we study the opto-electronic properties of an individual quantum dot embedded within a nanowire p-n junction. A single exciton, which is resonantly generated in the quantum dot, is converted into charge carriers in the nanowire and by utilizing the avalanche multiplication effect we demonstrate high yield of carriers for just a single generated exciton.

This chapter is based on:

G. Bulgarini, M.E. Reimer, M. Hocevar, E.P.A.M. Bakkers, L.P. Kouwenhoven and V. Zwiller, *Nat. Photon.* **6** (7), 455-458, (2012).

8.1 Introduction

Semiconductor quantum dots have been proposed as fundamental elements of a quantum information processor [9]. Quantum bits (qubits) can be stored in either the spin state of a single electron [3, 4], the spin state of a single hole [5] or the bright exciton state [2, 8]. Among these, exciton qubits are particularly attractive for long distance quantum communication through the exciton-to-photon and photon-to-exciton transfer of quantum information [10, 11]. Coherent optical control of a single exciton qubit in quantum dots has been demonstrated with both optical [8] and electrical [1, 6] read-out. However, current read-out schemes demand millions of excitation events in order to produce a measurable signal. To reduce the number of excitation events towards single-shot measurements, an internal pre-amplification electrical gain and generate a macroscopic current in response to a single photon absorbed [12]. As a result, single photons can be efficiently detected [13]. The avalanche process has been shown at the nano-scale using semiconductor nanowires [14, 15, 16] and carbon nanotubes [17], with sensitivity limited to, at best, approximately 100 photons. Importantly, semiconductor nanowires grown via bottom-up techniques offer an unprecedented material freedom in growing advanced heterostructures [18, 19] due to reduced strain achieved in the growth of highly mismatched materials [20]. Potentially, hetero-structured [21] and electrically defined [7] quantum dots can be combined within the same nanowire for quantum information processing.

In this work, we have integrated a single quantum dot at the p-n interface of a nanowire photodiode. The nanowire device is utilized in the avalanche multiplication regime under applied voltage bias. By spectrally and spatially separating the absorption region from the multiplication region, we can selectively generate a single exciton in the quantum dot that is multiplied after tunneling in the nanowire depletion region. We characterize the opto-electronic properties of the device by photocurrent measurements with both excitation about the nanowire bandgap and resonant excitation in the quantum dot.

8.2 Device characterization

A scanning electron microscopy (SEM) image of our device containing a single quantum dot embedded in a contacted InP nanowire is depicted in Fig. 8.1a. Typical devices are 4 to 6 μm long and have thickness of about 100 nm at the center of the nanowire. From the SEM image of the device, we observe that the nanowire is tapered. The tapering is not voluntary in this particularly case but is a consequence of the growth mechanism. The InP nanowire has been doped in-situ during vapor-liquid-solid growth in order to obtain a p-n junction. In addition to the standards precursor gases used for the growth on InP nanowires (Tri-methyl-indium and phosphine), the n-doping was achieved by supplying hydrogen sulfide and diethyl-zinc was used for the p-doping.

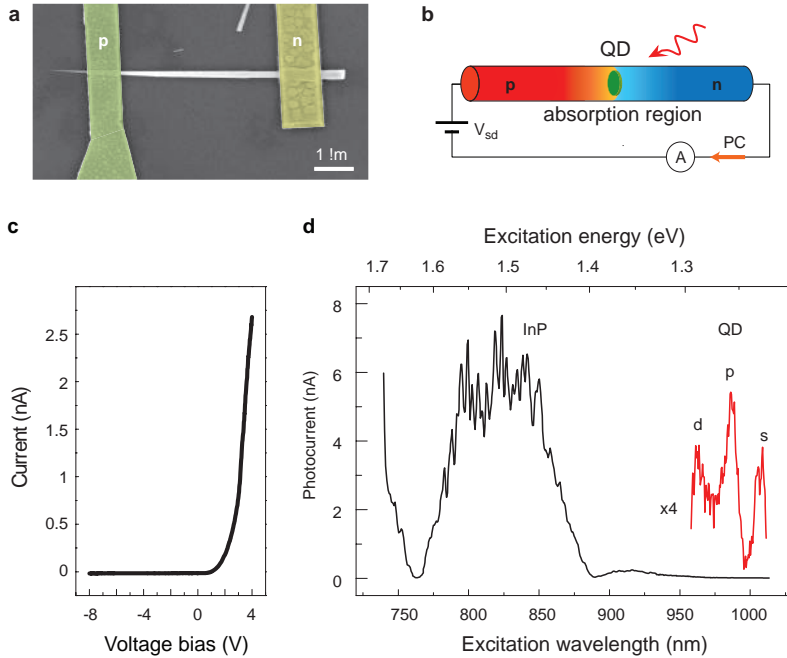


Figure 8.1: A single quantum dot in a nanowire photodiode. **a**, Scanning electron micrograph of the nanowire photodiode. **b**, A single quantum dot (QD) is located within the nanowire depletion region, where multiplication of the photocurrent (PC) is achieved under reverse voltage bias, V_{sd} . **c**, Current-voltage characteristic curve of the device. **d**, Photocurrent spectroscopy at $V_{sd} = -2$ V with $1 \mu\text{W}$ and $20 \mu\text{W}$ excitation power for the black and red curve, respectively. Band-edge absorption in the nanowire is observed around 825 nm (black). Absorption in the quantum dot s-, p- and d-shell is observed at longer wavelengths (red).

The growth is initiated with the n-InP section, followed by the InAsP quantum dot and the p-InP section. The quantum dot height is 6 ± 2 nm and the diameter is approximately 30 nm. Subsequently to the growth, nanowires were transferred on a SiO_2/Si substrate and contacts were defined by electron beam lithography. The n-side of nanowires was contacted with evaporated Ti/Au (100/10 nm), whereas Ti/Zn/Au (1.5/30/70 nm) was used for p-contacts. A rapid thermal annealing at 350°C was consequently performed to induce zinc diffusion from the contact into the nanowire and thus to reduce total resistance of the device. The absorption region of the nanowire is the depletion region of the p-n junction, as sketched in Fig. 8.1b. Under applied voltage bias, the p-n junction is used as an avalanche multiplication region to multiply both electrons and holes as they gain enough energy to initiate the multiplication process. In darkness, the p-n junction behaves as a standard diode. At positive applied voltage, the current increases with applied voltage due to the diffusion of majority carriers across the junction. The current is very low under applied reverse bias ($V_{sd} < 0$) because the conduction channel through the p-n junction is energetically forbidden. Under reserve

bias, the diode current is thus very sensitive to the generation of extra carriers due to light absorption. In Fig. 8.1c we probe the quantum dot and nanowire absorption spectra by tuning the laser excitation wavelength. The measured photocurrent shows a broad absorption peak around 825 nm, originating from InP band-edge transitions and suggests the presence of both wurtzite and zincblende crystal structures in the device [23]. Three photocurrent peaks are observed at higher excitation wavelengths: at 1007, 986 and 963 nm. By comparison with typical photoluminescence spectroscopy of single quantum dots in intrinsic nanowires, we assign these three peaks to absorption in the quantum dot s-, p-, and d-shell, respectively. From photoluminescence spectroscopy of the device at $V_{sd} = 0$ V, we confirm that the peak at 1007 nm is due to absorption in the quantum dot ground state (s-shell).

We now characterize the photo-response of the nanowire device. Optical excitation above the InP bandgap, E_g in Fig. 8.2c, is used in order to excite the entire nanowire depletion region. We use a continuous-wave laser at wavelength $\lambda = 532$ nm that is mechanically chopped at 120 Hz. The laser light impinging on the sample is linearly polarized along the nanowire elongation axis in order to maximize the absorption. Current-voltage characterization of the device is shown in the main panel of Fig. 8.2a as a function of incident optical power on the sample. Fig. 8.2b shows the temporal response of the photocurrent (blue line) to the laser trigger (dashed line). We obtain a time constant of 1 ms, which is a direct result of the high resistance of the device (60 M Ω). At $V_{sd} = 0$ V only the p-n junction built-in electric field separates electron-hole pairs to produce a measurable photocurrent without multiplication gain. Here, we measure a linear dependence for the ratio of charge carriers collected at the contacts to the number of photons absorbed by the nanowire. The number of absorbed photons is obtained by estimating of the absorption efficiency, details can be found in the appendix to this chapter. We determine that a single photon absorbed in the nanowire is converted into one electron (hole) worth of current with 96 % probability. This efficiency is comparable to state-of-the-art nanowire solar cells [24] and conventional quantum dot photodiodes [1]. In the reverse bias region ($V_{sd} < 0$), the dark current is less than 1 pA (dashed line). Under illumination, the photocurrent increases rapidly as the applied reverse bias is larger than $V_{sd} \sim -1$ V, since the absorption of a photon triggers an avalanche multiplication of carriers. The multiplication gain reaches saturation at stronger applied electric field and, at saturation, the photodiode current-voltage slope is set by the total series resistance, which decreases at higher photon flux. The occurrence of a light-induced avalanche at rather low applied bias is attributed to the small depletion region (~ 200 nm in length and 100 nm in diameter) and the low impact ionization energy threshold of InP. This photo-response is reproducible and similar behavior has been observed on six different devices. A schematic explanation of the avalanche process is shown in Fig. 8.2c for the case of absorption in the quantum dot. A single photon incident on the device with a frequency of one of the quantum dot energy levels is absorbed and creates a single exciton. Under reverse bias ($V_{sd} < 0$), the electron and hole separate and tunnel into the nanowire.

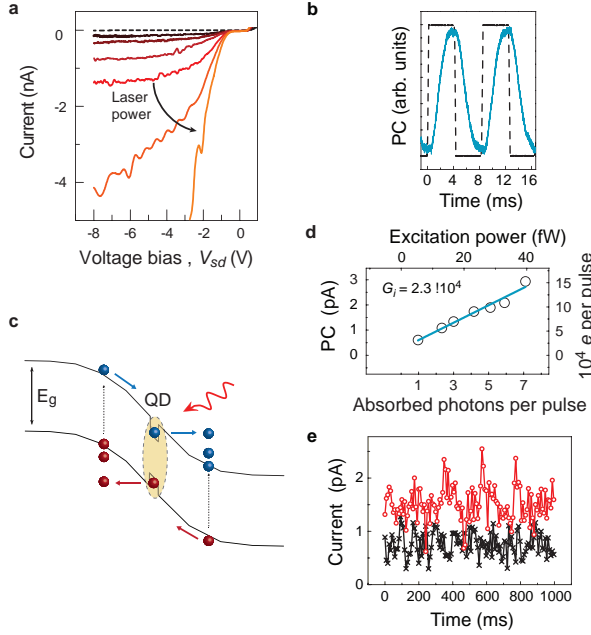


Figure 8.2: Single-photon detection with a nanowire photodiode. **a**, Device characteristics in dark (dashed line) and as a function of incident optical power (100 pW, black - 100 nW, orange) at $\lambda = 532$ nm (colored curves). **b**, Photocurrent temporal response (blue line) to 120 Hz laser pulses (black dashed line). **c**, Schematics of carrier multiplication starting from an exciton generated in the quantum dot, followed by tunneling in the nanowire avalanche region. **d**, Nanowire photodiode response at $V_{sd} = -8$ V. The photocurrent (PC) is obtained by subtracting the dark current (crosses in **e**) from the current measured upon illumination (circles in **e**).

Next, both the electron and hole accelerate under the applied electric field and once the carriers gain enough energy, additional electron-hole pairs are created by impact ionization. These additional electron-hole pairs can further trigger carrier multiplication and strongly enhance the photocurrent. The final result is that each exciton created in the quantum dot is multiplied into a macroscopic current. A unique feature of InP nanowires is that the impact ionization energy is similar for both electrons and holes: 1.84 eV and 1.65 eV, respectively [22]. Both carriers can thus contribute to the avalanche multiplication process and large gains can be obtained.

In Fig. 8.2d, we strongly attenuate the excitation pulses for investigating the multiplication gain in the few-photon regime. The device is operated below breakdown voltage at saturation of the light-induced avalanche multiplication ($V_{sd} = -8$ V) and at a temperature of 40 K in order to optimize the signal-to-noise ratio of the photocurrent. Each experimental data point (black circles) corresponds to the current averaged over 120 excitation pulses and with the dark current subtracted in order to obtain the net photocurrent (PC). From the linear fit (blue line) to the experimental data, we determine

an internal gain, $G_i = 2.3 \times 10^4$.

This high multiplication factor, combined with the low noise of the device (~ 0.2 pA), enables for the detection of a single photon absorbed per excitation pulse. In Fig. 8.2e the current measured for on average one photon absorbed per excitation pulse (circles) is compared to the dark current (crosses). We observe that the absorption of a single photon per pulse yields a signal well distinguished from the dark current with a signal-to-noise ratio of 2.5.

8.3 Resonant quantum dot excitation

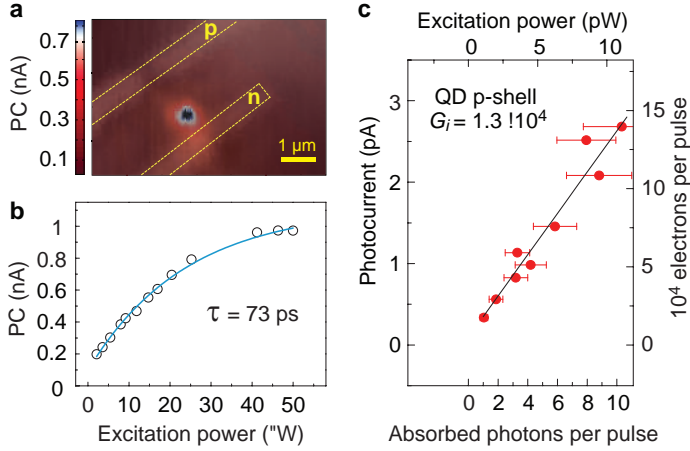


Figure 8.3: Resonant single-photon detection in the quantum dot. **a**, A photocurrent (PC) image for QD p-shell excitation is superimposed with a laser reflection image. As expected, the maximum occurs within the p-n junction where the quantum dot is located. **b**, Quantum dot p-shell photocurrent under continuous-wave excitation at zero applied bias. From the exponential fit (blue line), we determine the tunneling time τ of 73 ps for the slowest of the two carriers. **c**, At $V_{sd} = -8$ V, we obtain a gain of 1.3×10^4 per each photon generated in the quantum dot p-shell. Error bars ($\sim 30\%$) are determined by the variance in the measured quantum dot height.

In the following, we use the single quantum dot as the only absorption region of the nanowire photodiode. We selectively excite only the quantum dot p-shell transition and utilize the nanowire as a multiplication channel for the photo-generated exciton. In Fig. 8.3a we measure the photocurrent from the p-shell resonance (chosen for the highest absorption measured in Fig. 8.1d) as a function of the laser spot position. The photocurrent image is superimposed with a laser reflection image to exclude contribution from Schottky contacts. The photocurrent maximum is reached when the laser spot impinges between the metallic contacts. The same photocurrent maximum position

is obtained when exciting the entire nanowire with $\lambda = 532\text{ nm}$, confirming that, as expected, the quantum dot is positioned within the nanowire depletion region.

In Fig. 8.3b, we resonantly pump the quantum dot p-shell with continuous-wave excitation at zero applied bias, corresponding to a built-in electric field of 70 kV/cm . We observe a saturation of the photocurrent at $I_{sat} \sim 1\text{ nA}$ for high excitation power.

At saturation the current is limited by the tunneling time, τ , of the generated electron and hole. From the exponential fit to the data, we determine the tunneling time of the slowest carrier, $\tau = e/2I_{sat} = 73\text{ ps}$, similarly to Ref. [26], which represents the ultimate limit to the coherence of the exciton qubit.

Finally, we estimate the gain obtained after a single photon is resonantly absorbed in the quantum dot p-shell and tunnels into the nanowire multiplication region at $V_{sd} = -8\text{ V}$. Remarkably, we measure a large multiplication gain of 1.3×10^4 (Fig. 8.3c). As a result, a rate of one absorbed photon in the quantum dot per excitation pulse at 120 Hz is detected. The number of charge carriers collected per absorbed photon is four orders of magnitude larger than previously reported on self-assembled quantum dots embedded in diode structures [1] and seven orders of magnitude larger with respect to photodetectors based on a single contacted quantum dot in a nanowire [25].

The significant gain ($> 10^4$) we report for resonant absorption in a single quantum dot is promising towards single-shot electrical read-out of an exciton qubit state for the transfer of quantum information between flying and stationary qubits [10, 11]. The extremely small active area represents the fundamental limit to the device external efficiency, which can be enhanced by light harvesting with plasmonic antennas [27] and by reducing the optical excitation spot size with a solid immersion lens [28]. On the other hand, in the present configuration the quantum dot absorption region is spectrally and spatially separated from the multiplication region. The material freedom available during nanowire growth enables for engineering the quantum dot absorption properties, while preserving single-photon sensitivity with a unique sub-wavelength spatial resolution.

8.4 Appendix: Photon number estimation

We estimate the number of absorbed photons per pulse as follows. First, we calculate the overlap of the nanowire active area with the laser spot, assuming a rectangular nanowire cross-section. Next, the overall absorption efficiency, η_{abs} , is determined using the calculated overlap, bulk InP absorption coefficients [29] and taking into account reflections at the nanowire-air and nanowire-SiO₂ interfaces. Finally, the number of photons in a laser pulse is measured with a calibrated power-meter to obtain the number of absorbed photons, $P/(h\nu) \times \eta_{abs}$, where P is the laser power and $h\nu$ is the energy of a single photon. Laser transmission through filters and optical elements in the optical excitation path was measured for determining the optical power impinging on the sample.

The laser spot size is measured by photocurrent imaging and is determined to be $1.2\ \mu\text{m}$ for $\lambda = 532\ \text{nm}$ and $1.8\ \mu\text{m}$ for $\lambda = 986\ \text{nm}$ (QD p-shell). The photodiode active area was determined by SEM imaging and by four-point resistivity measurements to obtain doping concentrations of the p-n junction. Resistivity measurements are performed on homogeneous n- and p-doped InP nanowires, which have been grown under the same conditions of the nanowire p-n junction. From the measured doping levels of $10^{18}\ \text{cm}^{-3}$ for the n-side and $10^{17}\ \text{cm}^{-3}$ for the p-side, we estimate a p-n junction depletion region width of $140\ \text{nm}$ at $V_{sd} = 0\ \text{V}$.

The calculated absorption efficiency for $\lambda = 532\ \text{nm}$ at $V_{sd} = 0\ \text{V}$ is $0.3\ \%$. The active area of the photodiode (i.e. the depletion region) enlarges with applied reverse bias ($370\ \text{nm}$ at $-8\ \text{V}$), resulting in a higher absorption efficiency of $0.8\ \%$. The estimation for the absorption efficiency is only valid for polarization aligned along the nanowire axis, as the absorption for polarization perpendicular to the nanowire is strongly suppressed. The absorption efficiency obtained under resonant excitation in the quantum dot is $0.003\ \%$. The main source of error for the absorption efficiency is related to the measurement of the quantum dot height. We took into account this error with error bars ($\sim 30\ \%$) displayed in Fig. 8.3c.

8.5 References

- [1] A. Zrenner, et al., Coherent properties of a two-level system based on a quantum-dot photodiode *Nature*, **418**, 612–614 (2002).
- [2] X. Li. et al., An all-optical quantum gate in a semiconductor quantum dot. *Science*, **301**, 809–811 (2003).
- [3] F.H.L. Koppens et al., Driven coherent oscillations of a single electron spin in a quantum dot. *Nature*, **442**, 766–771 (2006).
- [4] D. Press, T.D. Ladd, B. Zhang and Y. Yamamoto, Complete quantum control of a single quantum dot spin using ultrafast optical pulses. *Nature*, **456**, 218–221 (2008).
- [5] D. Brunner et al., A coherent single-hole spin in a semiconductor. *Science*, **325**, 70–72 (2009).
- [6] S. Michaelis de Vasconcellos, S. Gordon, M. Bichler, T. Meier and A. Zrenner, Coherent control of a single exciton qubit by optoelectronic manipulation. *Nat. Photon.*, **4**, 545–548 (2010).
- [7] S. Nadj-Perge, S.M. Frolov, E.P.A.M. Bakkers and L.P. Kouwenhoven, Spin-orbit qubit in a semiconductor nanowire. *Nature*, **468**, 1084–1087 (2010).
- [8] Y. Benny et al., Coherent optical writing and reading of the exciton spin state in single quantum dots. *Phys. Rev. Lett.*, **106**, 040504 (2011).
- [9] D. Loss and D.P. DiVincenzo, Quantum computation with quantum dots. *Phys. Rev. A*, **57**, 120–126 (1998).
- [10] R. Vrijen and E. Yablonovitch, A spin-coherent semiconductor photo-detector for quantum communication. *Physica E*, **10**, 569–575 (2001).
- [11] H. Kosaka et al., Spin state tomography of optically injected electrons in a semiconductor. *Nature*, **457**, 702–705 (2009).
- [12] F. Capasso, Band-gap engineering: From physics and materials to new semiconductor devices. *Science*, **235**, 172–176 (1987).
- [13] B.E. Kardynal, Z.L. Yuan and A.J. Shields, An avalanche-photodiode-based photon-number-resolving detector. *Nat. Photon.*, **2**, 425–428 (2008).
- [14] C. Yang, C.J. Barrelet, F. Capasso and C.M. Lieber, Single p-type/intrinsic/n-type silicon nanowires as nanoscale avalanche photodetectors. *Nano Lett.*, **6**, 2929–2934 (2006).

- [15] O. Hayden, R. Agarwal and C.M. Lieber, Nanoscale avalanche photodiodes for highly sensitive and spatially resolved photon detection. *Nat. Mater.*, **5**, 352–356 (2006).
- [16] M.E. Reimer et al., Single photon emission and detection at the nanoscale utilizing semiconductor nanowires. *J. Nanophoton.*, **5**, 053502 (2011).
- [17] N.M. Gabor, Z. Zhong, K. Bosnick, J. Park and P.L. McEuen, Extremely efficient multiple electron-hole pair generation in carbon nanotube photodiodes. *Science*, **325**, 1367–1371 (2009).
- [18] K. Tomioka, J. Motohisa, S. Hara, K. Hiruma and T. Fukui, GaAs/AlGaAs core multishell nanowire-based light-emitting diodes on Si. *Nano Lett.*, **10**, 1639–1644 (2010).
- [19] M. Heurlin et al., Axial InP Nanowire Tandem Junction Grown on a Silicon Substrate. *Nano Lett.*, **11**, 2028–2031 (2011).
- [20] M.E. Messing, et al., Growth of straight InAs-on-GaAs nanowire heterostructures. *Nano Lett.*, **11**, 3899–3905 (2011).
- [21] E.D. Minot, et al, Single quantum dot nanowire LEDs. *Nano Lett.*, **7**, 367–371 (2007).
- [22] T.P. Pearsall, Threshold energies for impact ionization by electrons and holes in InP. *Appl. Phys. Lett.*, **35**, 168–170 (1979).
- [23] R.E. Algra et al., Twinning superlattices in indium phosphide nanowires. *Nature*, **456**, 369–372 (2008).
- [24] M.D. Kelzenberg et al., Enhanced absorption and carrier collection in Si wire arrays for photovoltaic applications. *Nat. Mater.*, **9**, 239–244 (2010).
- [25] M.P. van Kouwen et al., Single quantum dot nanowire photodetectors. *Appl. Phys. Lett.*, **97**, 113108 (2010).
- [26] E. Beham, A. Zrenner, F. Findeis, M. Bichler and G. Abstreiter, Nonlinear ground-state absorption observed in a single quantum dot. *Appl. Phys. Lett.*, **79**, 2808–2810 (2001).
- [27] A.G. Curto et al., Unidirectional emission of a quantum dot coupled to a nanoantenna. *Science*, **329**, 930–933 (2010).
- [28] J.A.H. Stotz and M.R. Freeman, A stroboscopic scanning solid immersion lens microscope. *Rev. Sci. Instrum.*, **68**, 4468–4477 (1997).
- [29] D.E. Aspnes and A.A. Studna, Dielectric functions and optical parameters of Si, Ge, GaP, GaAs, GaSb, InP, InAs, and InSb from 1.5 to 6.0 eV. *Phys. Rev. B*, **27**, 985–1009 (1983).

CHAPTER 9

Conclusions and outlook

At the beginning of this research thesis in 2010, there was a large gap in the development of quantum dots in nanowires compared to the established system of self-assembled quantum dots. Nanowires were providing broad single-photon emission with a low count-rate and thus, quantum dots grown in nanowires were considered by the larger part of the scientific community as a second class single-photon source. A fashionable geometry and future promises were not sufficient to conceive nanowires as candidates for complex quantum optics experiments.

In this thesis, we studied both single-photon emission properties as well as the photodetection capabilities of semiconductor nanowires, addressing one by one the major key issues for improving the optical quality of the system. As a result, nanowire waveguides containing single quantum dots now demonstrate their maturity to become one of the leading architectures for the realization of reliable single-photon sources to be applied in future quantum communication technology.

9.1 Achieved results and status of research

- The optimized nanowire waveguides with tailored shape and dimensions enabled us to achieve high single-photon fluxes. The single-photon count-rate achieved with an integrated bottom mirror improves by more than 20 times that obtained with thin nanowires, where waveguide conditions are not satisfied. The state-of-the-art nanowire waveguides achieve nearly one million counts on standard silicon single-photon counters, making nanowire waveguides one of the brightest single-photon source in scientific laboratories.

- We have imaged the far field emission profile of the quantum dot emission that is coupled to waveguide modes in a tapered waveguide, demonstrating a perfect Gaussian mode for coupling to the fundamental guided mode. Hence, single photons are coupled with nearly no insertion losses into single mode optical fibers that are necessary to bring quantum communication to long distances.
- We have greatly improved the quantum dot emission linewidth by controlling the crystal structure of the nanowire surrounding the quantum dot. In nanowires with a pure crystal phase we observe optical linewidths of a few μeV , which is 2 orders of magnitude better than the average linewidth prior to this crystal phase optimization. Importantly, we have demonstrated that the best coherence properties are obtained at exciton saturation pumping power. Thus, the commonly suffered compromise between brightness and linewidth in self-assembled quantum dots is resolved.
- A single quantum dot embedded at the p-n interface of a nanowire diode is a promising system for achieving electroluminescence at the single-photon level but also provides efficient photodetection. Single excitons are resonantly generated in the quantum dot and detected electrically along the nanowire utilizing electrical multiplication gain.

Remarkably, the three ingredients of high brightness, Gaussian emission profile and narrow linewidth are achieved simultaneously in a single nanowire waveguide operated at exciton saturation. Furthermore, only a single quantum dot is positioned per nanowire waveguide. All these benefits represent a tremendous advantage over other single-photon sources concerning their scalability. Scaling-up semiconductor single-photon sources is a necessary requirement to bring quantum devices from the academic labs to commercial applications.

9.2 Future research directions

Single quantum dots in nanowires already fulfill many of the requirements for becoming building blocks of quantum communication. Future work must be driven towards demonstrating their advantageous applicability in real technology. Nanowire photodiodes have the potential to be used as photodetectors with very selective and localized absorption area. However, the nanometric dimensions of a nanowire device, such as the one shown in chapter 8, result in a very low overall detection efficiency. In addition, the intrinsic high resistivity of nanowires, which is due to the nanowire shape, hampers their fast operation. As a solution, nanowires can be grown in ordered arrays, separated by a polymer film, sharing the top and the bottom contact. A heavily doped growth substrate can be used for the bottom contact, whereas the deposition of a transparent contact, such as indium tin oxide (ITO), is necessary for the top contact [1]. A photodetector

composed of a nanowire array provides a large surface area for enhancing the photon absorption efficiency and for lowering the resistance in order to reduce the detector time response. The interdistance between nanowires as well as the nanowire diameter must be precisely tuned in order to further optimize light absorption for the selected application wavelength and for trapping light in the nanowire array [2]. The advantage of utilizing nanowires as photodetectors is the versatility in choosing the growth material, thereby achieving heterostructures covering a wider spectral range with respect to standard semiconductor detectors.

Regarding single-photon emission, a natural follow-up experiment to this thesis work is two photon interference from distinct nanowire waveguides. The importance of this measurement is demonstrating the suitability of nanowire waveguides as the nodes of a quantum network. In this thesis, the experimental investigation of the luminescence properties of quantum dots has been pursued via laser excitation. An important step towards practical applications would be to make nanowire quantum light sources compatible with electrical injection. Recent developments in this direction have been performed on GaN nanowires with embedded InGaN quantum dots [3]. The results robustly demonstrate single-photon emission under an injected current of 1 nA in the nanowire. The great advantage of a nanowire-based single-photon light emitting diode is indisputably the ability of placing only one emitter at the p-n interface. This level of addressability is necessary to scale-up the number of single-photon sources embedded on a chip and it is thus far not achievable with self-assembled quantum dots. The functionality of lying nanowire devices is at the moment still hampered by the low detection efficiency due to the disadvantageous light dispersion in the substrate and the uncontrolled light emission direction. We have investigated the possibility of designing solid immersion lenses (SILs) on top of the quantum dots in nanowires in order to achieve very high photon extraction efficiency even for lying nanowires. The concept is described in chapter 3 of this thesis. Our approach for the realization of the lenses starts with depositing individual nanowires on a 100 μm thick substrate of GaP. The high refractive index (3.13 at 950 nm) and transparency of GaP for the InAsP quantum dot wavelength range makes it the ideal material for a solid immersion lens for our system. Fig. 9.1 displays a scanning electron micrograph of a solid immersion lens milled on GaP with a Fresnel type of design. In the Fresnel design, the lens is only a few microns thick, but the increasing curvature at increasing distance from its center replicates the curvature of a hemisphere lens. The position of the quantum dot, defining the lens center, is mapped by collecting photoluminescence with respect to previously deposited reference gold markers. Second, the identified center position the lens is milled in the scanning electron microscope equipped with focussed ion beam. A thinner GaP layer will enable in future implementation for a simpler and more precise alignment of the SIL with respect of the quantum dot. Precise lens alignment can be achieved through in-situ optical lithography performed at cryogenic temperatures [4, 5].

An alternative solution for increasing the detected photon flux by taking advantage of the lying nanowire geometry is coupling the quantum dot emission to on-chip waveg-

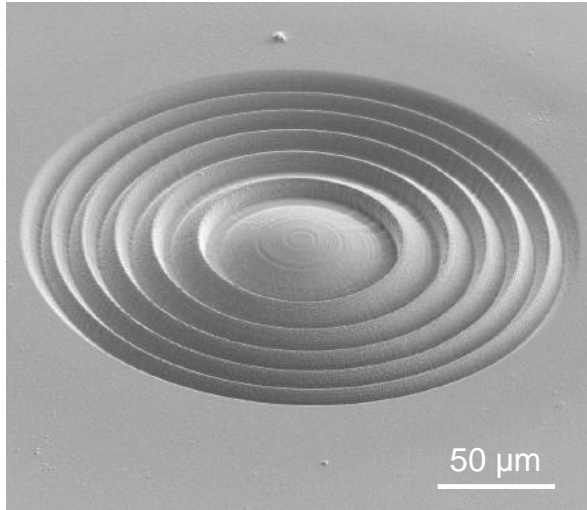


Figure 9.1: Fresnel solid immersion lens. Fresnel solid immersion lens imaged with a scanning electron microscope. The lens is milled with focused ion beam milling using Ga ions on a GaP substrate. The nanowire with embedded single-photon emitter is located at a 100 μm distance underneath the lens surface.

uides. The Gaussian emission mode of nanowire waveguides makes them ideal candidates for coupling to other optical components such as optical fibers or planar waveguides. If high coupling efficiency to the waveguide is achieved, photons are detected with negligible losses by placing one end of the silicon waveguide on top of superconducting single-photon detectors [6]. For this detection geometry, electrical excitation would be preferable because it avoids the technologically challenging issue of rejecting laser light. Coupling single-photon sources to on-chip waveguides drives towards the implementation of multi-photon algorithms and is a way to implement linear optics quantum computation [7, 8] Combining electrically driven single-photon sources with on-chip waveguides, while maintaining the high brightness and excellent optical properties shown in this thesis, would represent an impressive progress in the field of quantum photonics.

9.3 Outlook: a plug and play single-photon generator

Single-photon sources and detectors are at the core of quantum communication and play a central role in the development of novel quantum technology. We propose here an idea to turn the single-photon sources developed in this thesis into a plug and play device. The aim is a single-photon source which guarantees the optical properties discussed throughout this thesis, but also provides ease of use and a robust implementation design

for reliable, long-term operation. In this work, we demonstrated the development of single-photon sources based on nanowires with embedded semiconductor quantum dots. These sources provide high count-rate emission in a Gaussian mode in the far-field with excellent single-photon coherence properties. However, for measuring the optical properties of such devices, a complex setup with bulky lasers and complex cryogenic optical setups was used.

Our idea for simplifying single-photon generation is to directly connect a nanowire single-photon source to a single-mode optical fiber. Provided the Gaussian emission mode, coupling from a nano-emitter to an optical fiber has negligible losses as shown in chapter 6 of this thesis. Once photons are inserted in the fiber they propagate in the fundamental guided and fiber-based technology can be utilized. This innovative approach eliminates the use of mirrors, lenses and spectrometer, resulting in a compact single-photon source ready for applications at relatively low fabrication costs. Moreover, optical fibers are the fundamental building blocks of present and future communication technology. Communication over kilometric distances is enabled with low propagation losses by optical fibers operating in two infrared wavelength windows: $1.31\text{ }\mu\text{m}$ and $1.55\text{ }\mu\text{m}$. Quantum dots are ideal sources for tuning the emission wavelength towards telecommunication windows, due to the versatility in the choice of the semiconductor composition [9, 10].

Device fabrication

The device fabrication procedure is displayed in the schematics of Fig. 9.2. Nanowires waveguides are first grown in ordered arrays on the substrate. Subsequently a layer of positive resist for photolithography is spun on the sample as shown in Fig. 9.2b. The resist covers the entire length of the nanowires, similarly to the process presented in chapter 5 for nanowire transfer and integration of a gold mirror. In a micro-photoluminescence setup, the nanowires will be investigated at low temperature in order to select the best candidate for the plug and play single-photon generator. Criteria for selection are the brightness of the source discussed in chapter 4 of this thesis, purity of single-photon statistics and the linewidth of the emission spectrum. For this last step, a Michelson interferometer can be employed for high resolution spectral measurements as shown in chapter 7 of this thesis.

Once the best candidate are selected, a UV laser will be utilized for photolithography at cryogenic temperature [4]. Resist is exposed around of the selected nanowire with a resolution up to 50 nm of having the nanowire exactly located in the center of the exposed resist [5]. After lift-off of the remaining unexposed resist, the exposed positive resist will protect the nanowire in the subsequent dry etching step, 9.2c. A disk is etched in the substrate, surrounding the nanowire, with dimensions defined during the photolithography step. Precisely, the disk diameter is set to 1.25 mm, that is the diameter of the commercial sleeves hosting single-mode fibers inside fiber cables, as shown in Fig. 9.3a. Hence, the processed nanowire chip fits exactly the dimensions of fiber

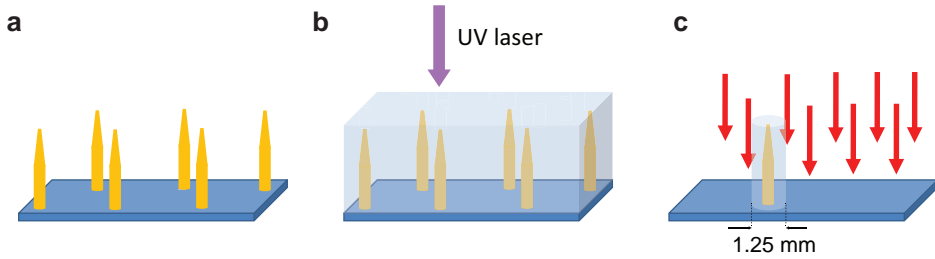


Figure 9.2: Nanowire selection procedure. **a**, Nanowires with embedded quantum dots are grown in ordered arrays. **b**, Positive photo-resist is spun on the sample to enable photolithography with a UV radiation while being able to measure the quantum dot luminescence at cryogenic temperature. The exposed resist protects the selected nanowire in the following dry etching process, **c**, which isolates the selected nanowire and defines around it a disk of precisely the same diameter of a fiber sleeve.

sleeves and self-aligns to the optical fiber for maximizing the collection of single photons. The full fiber-based device implementation is depicted in Fig. 9.3**b**. A fiber splitter is utilized to connect an excitation laser. Along the fiber, a compact fiber-based band-pass filter (1 nm bandwidth) is utilized to select the exciton emission for single-photon generation. We stress that the position control achievable with nanowires is crucial for this implementation. Only one quantum emitter is excited by the pump laser making bulky filtering techniques, such as a spectrometer, unnecessary. By avoiding losses due to propagation through bulky optical components, single-photon rates higher than 10 MHz are anticipated at the fiber output, improving by at least an order of magnitude the best single-photon fluxes currently available in scientific labs. We note that with aim of connecting more sources in a quantum network, the photon count-rate becomes exponentially important for accelerating the measurement speed of photon correlations measurements.

Applications

Applications of quantum light sources are various and this number will tend to increase in the future. Individual photons and linear optical components are the fundamental building blocks of the all-optical universal quantum computer [7, 8]. Indistinguishable single photons are utilized as the input of boson sampling machines [11, 12], where the photon distribution is probed after transmission through a circuit of interconnected waveguides which may represent a calculation problem or a simulated physical system. Key challenges are to produce bright sources of indistinguishable single photons, fast and efficient photodetectors and to connect single-photon emitters in a low-loss network composed by scalable optical elements. In communication science, quantum cryptography is the closest quantum technology to real application. However, the level of security of quantum cryptography systems and their possible scalability depends heavily on the single-

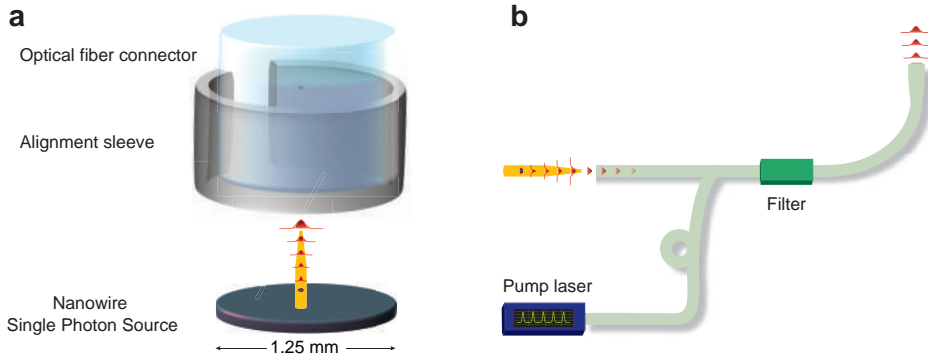


Figure 9.3: Plug and play single-photon source. **a**, A nanowire waveguide containing an emitter of individual photons is perfectly aligned to a single-mode optical fiber. **b**, Schematics of the full fiber-based device implementation. The single-photon generator, self-aligned with the optical fiber is excited by a pulsed laser. After propagation through the filtering stage, high single-photon flux is expected fiber output.

photon generation scheme. State-of-the-art quantum cryptography implementations utilize photons emitted via the downconversion of laser photons in a non-linear crystal. This generation process is probabilistic, with furthermore a very low yield of $\sim 10^{-10}$. A very high laser power is hence required to output pairs of single photons. Moreover, since the generation of single photons is random (follows Poissonian statistics), there is non-negligible probability of generating 2 or 3 pairs of photons, thereby fundamentally deviating from ideal single-photon operation and opening the door to eavesdropper. Quantum cryptography will thus greatly benefit from semiconductor sources which offer on-demand single-photon generation at a higher count-rate with respect to the laser downconversion process. First results utilizing semiconductor quantum dots as sources for quantum cryptography protocols are based on photonic microcavities [13]. However, the optical quality of the single photons decreases with increasing pump rate, giving a detrimental trade-off between information bit-rate and quality of photon statistics. We have demonstrated in chapter 7 that the source we developed in this thesis does not suffer from this problem.

The generation of random numbers is of fundamental importance in fields where unpredictability is crucial, such as cryptography, numerical simulations, gambling but also for answering fundamental questions of quantum physics [14]. True randomness, besides being a quantity of difficult definition, is of complex experimental realization. Quantum light sources can represent the solution to the generation of true random numbers. The concept is as follows: one at a time, individual photons are led to a beam splitter where each photon has 50 % probability of being reflected and 50 % probability of being transmitted. At these two output ports of the beam splitter, single-photon counters with assigned a digit '0' and '1' will count the received photons collected during time. The result is a totally random binary sequence. True randomness, however, is affected by the

noise introduced by its physical implementation and is only generated if very efficient source and detectors are utilized [15]. This will be possible with our implementation of the single-photon generator directly connected via a fiber-baser splitter to extremely efficient superconducting single-photon detectors [16].

9.4 References

- [1] Y. Cui et al., Reversible Switching of InP Nanowire Growth Direction by Catalyst Engineering. *Nano Lett.* **13**, 4113–4117 (2013).
- [2] J. Wallentin et al., InP nanowire array solar cells achieving 13.8% efficiency by exceeding the ray optics limit. *Science* **339** 1057–1060 (2013).
- [3] S. Deshpande, J. Heo, A. Das and P. Bhattacharya, Electrically driven polarized single-photon emission from an InGaN quantum dot in a GaN nanowire. *Nat. Commun.*, **4**, 1675 (2013).
- [4] S. Fälth, V. Zwiller, W. Seifert and M.-E. Pistol, Isolating single selected quantum dots using cryogenic photolithography. **101**, 133–135 (2002).
- [5] A. Dousse et al., Controlled light-matter coupling for a single quantum dot embedded in a pillar microcavity using far-field optical lithography. *Phys. Rev. Lett.* **101**, 267404 (2008).
- [6] W.H.P. Pernice et al., High-speed and high-efficiency travelling wave single-photon detectors embedded in nanophotonic circuits. *Nat. Commun.* **3**, 1325 (2012).
- [7] E. Knill, R. Laflamme and G.J. Milburn, A scheme for efficient quantum computation with linear optics *Nature* **409**, 46–52 (2001).
- [8] J.L. O’Brein, Optical Quantum Computing. *Science* **318**, 1567–1570 (2007).
- [9] M.B. Ward et al., On-demand single-photon source for 1.3 μ m telecom fiber. *Appl. Phys. Lett.* **86**, 201111 (2005).
- [10] M. Benyoucef, M. Yacob, J.P. Reithmaier, J. Kettler and P. Michler, Telecom-wavelength (1.5 μ m) single-photon emission from InP-based quantum dots. *Appl. Phys. Lett.* **103**, 162101 (2013).
- [11] M.A. Broome et al., Photonic Boson Sampling in a Tunable Circuit. *Science* **339**, 794–797 (2013).
- [12] J.B. Spring et al., Boson Sampling on a Photonic Chip. *Science* **339**, 797–801 (2013).
- [13] T. Heindel et al., Quantum key distribution using quantum dot single-photon emitting diodes in the red and near infrared spectral range. *New J. Phys.* **14**, 083001 (2012).
- [14] A. Aspect, J. Dalibard and G. Roger. Experimental Test of Bell’s Inequalities Using Time-Varying Analyzers. *Phys. Rev. Lett.* **49**, 1804–1807 (1982).

- [15] D. Frauchiger, R. Renner, M. Troyer, True randomness from realistic quantum devices. arXiv:1311.4547 (2013).
- [16] F. Marsili et al., Detecting single infrared photons with 93% system efficiency. *Nat. Photon.* **7**, 210–214 (2013).

Summary

In this PhD thesis I experimentally investigated the electrical and optical properties of zero-dimensional semiconductor nanostructures that are known as quantum dots. At the nanoscale, semiconductor materials behave differently than in the micro- and macroscopic world. Amongst the effects given by the nanometric dimensions, quantum dots enable the generation of single light particles: photons.

Single photon emitters and detectors are central building blocks of future communication technologies. As the miniaturization in electronics is driving towards the quantum limit, we envision future telecommunication as based on single photons. Single photons enable the use of quantum properties of light to encode information and share it with unbreakable security provided by quantum cryptography. Based on the principle that a single photon cannot be cloned and that its quantum state cannot be observed without altering it the information that the photon is carrying, a single particle of light represents the ideal mean of transportation for future secure telecommunication.

During my research work, I studied individual quantum dots embedded in one-dimensional nanostructures called nanowires. The optical properties of the quantum dots have been explored through photoluminescence spectroscopy and improved in order to obtain a pure flux of single photons. Simultaneously, the material composition and shape of the nanowire have been designed to achieve efficient collection of these photons. Nanowires are tailored into waveguides providing directional propagation along the nanostructure that out-couples to the macroscopic world with negligible losses. This system we developed can be seen as an analogue of an optical fiber where photons are propagating one at a time. Several optical properties of the emitted single photons have been analyzed and subsequently optimized such as the temporal emission statistics, the shape and dispersion of the energy spectrum and the spatial emission profile. In addition, we demonstrated the possibility of creating an excitation in the quantum dot and translate this excitation into an electrical signal transmitted along the nanowire, thereby detecting the generation of individual excitations in the nanostructure.

Samevatting

In dit proefschrift onderzoek ik experimenteel de elektrische en optische eigenschappen van halfgeleidende nanostructuren die kwantumdots worden genoemd. Deze structuren worden beschouwd als 0-dimensionaal omdat ze in alle richtingen afmetingen op de nanoschaal hebben. Op deze nanoschaal gedragen halfgeleidende materialen zich anders dan in de micro- en macroscopische wereld. Vanwege deze kunnen kwantumdots, als een van de effecten van de gereduceerde grootte, enkele lichtdeeltjes generen: fotonen.

Generatoren en detectoren van enkele fotonen zijn de centrale bouwstenen voor toekomstige communicatie technologieën. Net als de schaalverkleining in de elektronica die richting de kwantum limiet gaat, kan men een toekomstige telecommunicatie voorzien die gebaseerd is op enkele fotonen. Door het gebruik van enkele fotonen is het mogelijk informatie te coderen in de kwantum eigenschappen van het licht. Het is dan mogelijk deze informatie te delen met een niet te kraken beveiliging die wordt geboden door de kwantumcryptografie. Omdat een enkel foton niet kan worden gekloond en zijn kwantum status niet kan worden vastgesteld zonder de informatie te veranderen, vertegenwoordigt een enkel lichtdeeltje de ideale informatiedrager voor de beveiligde telecommunicatie van de toekomst.

Tijdens mijn onderzoek, heb ik enkele kwantumdots in 1-dimensionale nanostructuren, nanodraden genoemd, bestudeerd. De optische eigenschappen van de kwantumdots zijn onderzocht met laserspectroscopie en geoptimaliseerd om een zuivere flux van enkele fotonen te krijgen. Tegelijkertijd zijn de materiaalsamenstelling en vorm van de nanodraad ontworpen om op een efficiënte wijze deze fotonen te collecteren. In analogie van optische fibers zijn nanodraden vormgegeven als golfgeleiders die zorgen voor propagatie langs de nanostructuur en die vervolgens uitkoppelen naar de macroscopische wereld met te verwaarlozen verliezen. Verschillende optische eigenschappen van de uitgezonden enkele fotonen zijn geanalyseerd en geoptimaliseerd, zoals de tijdsafhankelijke statistiek van de emissie, de vorm en de dispersie van het energiespectrum en het ruimtelijke profiel van de emissie. Bovendien demonstreren we de mogelijkheid om een excitatie van de kwantumdot te bewerkstelligen en deze excitatie om te zetten in een elektrisch signaal dat wordt verzonden langs de draad, waardoor we een enkele excitatie in een nanostructuur kunnen detecteren.

Sommario

In questa tesi ho investigato sperimentalmente le proprietà elettriche e ottiche di semiconduttori nanostrutturati che prendono il nome di *quantum dots*, letteralmente tradotto come punto quantico. Queste strutture sono considerate zero-dimensionali perché hanno dimensioni nanometriche lungo ogni direzione. Alla nanoscala, i materiali presentano caratteristiche differenti rispetto a quelle che possono essere osservate su scala micro e macroscopica. Tra i tanti effetti dovuti alle dimensioni nanometriche, le *quantum dots* permettono la generazione di singole particelle di luce: fotoni.

Emettitori e rivelatori di singole particelle di luce, ovvero single fotoni, saranno componenti fondamentali delle future tecnologie di comunicazione. Come per la miniaturizzazione dei componenti elettronici, possiamo immaginare che le telecomunicazioni del futuro siano basate sulla trasmissione di singole particelle. Oltre a rappresentare un metodo efficiente di comunicare, la trasmissione di single fotoni permetterebbe di usare le proprietà quantistiche della luce per codificare informazioni e di utilizzare tecniche di crittografia quantistica per condividere dati in assoluta sicurezza. Una singola particella non può essere clonata e allo stesso tempo l'informazione trasportata dal fotone viene modificata nel momento in cui si tenta di piratarla. Per questi motivi, singoli fotoni sono i messaggeri ideali per il futuro delle telecomunicazioni.

Durante il mio progetto di ricerca, ho studiato singole *quantum dots* inserite in nanostrutture più grandi, uni-dimensionali, chiamate *nanowires*. Le caratteristiche ottiche delle *quantum dots* sono state esplorate per mezzo di spettroscopia di luminescenza e ottimizzate per generare un flusso di singoli fotoni. Allo stesso tempo, la composizione e la forma della nanostruttura ospitante sono state adattate per ottenere un'efficiente collezione di questi fotoni. I *nanowires*, in analogia con i concetti utilizzati per le fibre ottiche, sono stati progettati per guidare i singoli fotoni lungo la nanostruttura e trasmetterli nel mondo macroscopico con perdite trascurabili. Il sistema che abbiamo sviluppato può essere visto come un analogo di una fibra ottica nanoscopica dove particelle di luce vengono propagate una alla volta. Molte caratteristiche dei fotoni sono state prima analizzate e poi migliorate come la statistica temporale di emissione, la dispersione nello spettro energetico e il profilo spaziale di emissione. Inoltre, abbiamo dimostrato la possibilità di creare un'eccitazione nella *quantum dot* e trasformarla in un segnale elettrico trasmesso lungo il *nanowire* in modo da individuare la generazione di singole eccitazioni nella nanostruttura.

Curriculum Vitae

Gabriele Bulgarini

- | | |
|--------------|--|
| 29 Oct, 1985 | Born in Milan, Italy. |
| 1999–2004 | Scientific high school diploma at Liceo Scientifico G.B.Vico, Corsico, Italy. |
| 2004–2007 | BsC in Engineering Physics at Politecnico di Milano, Milan, Italy. |
| 2007–2009 | MsC in Engineering Physics at Politecnico di Milano, Milan, Italy. |
| 2009 | Internship at Friedrich Schiller Universitaet, Jena, Germany. |
| 2010–2014 | PhD research under the supervision of dr. V. Zwiller and prof. dr. ir. L.P. Kouwenhoven at Delft University of Technology, Delft, The Netherlands. |

Publications

- *Overcoming power broadening of the quantum dot emission in a pure wurtzite nanowire*
M.E. Reimer, G. Bulgarini, R.W. Heeres, B.J. Witek, M.A.M. Veerstegh, D. Dalacu, P.J. Poole and V. Zwiller, (2014). *Manuscript submitted*
- *Nanowire waveguides launching single photons in a Gaussian mode for ideal fiber-coupling*
G. Bulgarini, M.E. Reimer, M. Bouwes Bavinck, K.D. Jöns, D. Dalacu, P.J. Poole, E.P.A.M. Bakkers and V. Zwiller, (2013). *Manuscript under review*
- *Ultra-clean emission from InAsP quantum dots in defect-free wurtzite InP nanowires*
D. Dalacu, K. Mnaymneh, J. Lapointe, X. Wu, P.J. Poole, G. Bulgarini, V. Zwiller and M.E. Reimer, *Nano Letters* **12**, 5919-5923 (2012).
- *Optical polarization properties of nanowire quantum dots probed along perpendicular orientations*
G. Bulgarini, M.E. Reimer, E.P.A.M. Bakkers and V. Zwiller, *Applied Physics Letters* **101**, 111112 (2012).
- *Avalanche amplification of a single exciton in semiconductor nanowires*
G. Bulgarini, M.E. Reimer, M. Hocevar, E.P.A.M. Bakkers, L.P. Kouwenhoven and V. Zwiller, *Nature Photonics* **6**, 455-458 (2012).
- *Spontaneous emission control of single quantum dots in bottom-up nanowire waveguides*
G. Bulgarini, M.E. Reimer, T. Zehender, M. Hocevar, E.P.A.M. Bakkers, L.P. Kouwenhoven and V. Zwiller, *Applied Physics Letters* **100**, 121106 (2012).

- *Bright single photon sources in bottom-up tailored nanowires*
M.E. Reimer, G. Bulgarini, N. Akopian, M. Hocevar, M. Bouwes Bavinck, E.P.A.M. Bakkers, L.P. Kouwenhoven and V. Zwiller, *Nature Communications* **3**, 737 (2012)
- *Nanogolfgeleider voor individuele fotonen*
M. Bouwes Bavinck, M.E. Reimer, G. Bulgarini, E.P.A.M. Bakkers, V. Zwiller, *Nederlands Tijdschrift voor Natuurkunde* **78**, 11 (2012).
- *Single semiconductor quantum dots in nanowires: growth, optics, and devices*
M.E. Reimer, N. Akopian, K. Barkelid, G. Bulgarini, R.W. Heeres, M. Hocevar, B.J. Witek, E.P.A.M. Bakkers and V. Zwiller, chapter in *Quantum Dots: Optics, Electron Transport and Future Applications*, edited by A. Tartakovskii, Cambridge University Press, (2012).

A little longer than four years ago I sent an email to Val Zwiller asking for open PhD positions in his group. The same night at 3 'o clock I got an answer saying that a very interesting project on nanowire LEDs was waiting for me. I felt extremely blessed to have a response in the middle of the night but soon I would realize that Val's sleeping hours weren't exactly standard. I thus came to Delft for my interview and I had a very positive impression: Delft was a lovely place, people in QT were very friendly and there was top of the line equipment plus a world class clean room. After a couple of days I indeed accepted the PhD position, unconventionally via Google chat.

After four years in the Netherlands I can say that my experience went even beyond expectations. I am first of all grateful to Leo and Val for giving me the opportunity to work in such an international, colorful and ambitious group. We modified the LED project along the way achieving very good results always accompanied with great fun. My work wouldn't be possible without our collaborations. I would like to thank Erik and his lively group and I am grateful to Dan and Philip for working with us during the last part of my PhD.

A special thank is reserved for Michael who shared with me most of the work in this thesis, first teaching me the secrets of optical alignment and then those of running for joining the *Flying Qubits* team! I guess it's not a secret to anyone that I really enjoyed spending my time in QT: starting on Monday morning with the *Nederlands cursus* at the coffe table, working in the dark lab and concluding the week at the TPKV on Friday afternoon until the *laatste ronde*. It has been a great time.

Gabriele
Delft, May 2014

